ISSN 1913-1844

MODERN APPLIED SCIENCE

Vol. 3, No. 3
March 2009

Canadian Center of Science and Education

Editorial Board

CCSE

Modern Applied Science

www.ccsenet.org/journal.html

Vol. 3, No. 3

March 2009

Contents

Modern Applied Science

www.ccsenet.org/journal.html

Vol. 3, No. 3

March 2009

Contents

Modern Applied Science

www.ccsenet.org/journal.html

Vol. 3, No. 3

March 2009

An Experimental Approach for Engine Mapping

Recep Kozan

Sakarya University, Faculty of Engineering

Esentepe Kampüsü, 54187, Adapazarı-Turkey

Tel: 90-262-311-4351 E-mail: kazan@sakarya.edu.tr

İmdat Taymaz

Sakarya University, Faculty of Engineering

Esentepe Kampüsü, 54187, Adapazarı-Turkey

Tel: 90-262-311-4351 E-mail: taymaz@sakarya.edu.tr

Mersin Gokce (Corresponding author)

Sakarya University, Faculty of Engineering

Esentepe Kampüsü, 54187, Adapazarı-Turkey

Tel: 90-262-311-4351 E-mail: mersingokce@yahoo.com

Abstract

Both collecting data and constructing of a diesel engine's specific fuel consumption model by two-stage modeling approach is investigated in this study. The cam angle is swept from minimum to maximum for different engine speed and torque values and, the specific fuel consumption at these points are measured at an engine test bench in a workshop. The different specific fuel consumption models are created by using the collected data and, the best model among these models is chosen by the help of statistical parameters

Keywords: Engine mapping, Two-stage modelling, Specific fuel consumption

1. Introduction

Engine mapping is the modeling engine behaviors as a function of engine's adjustable parameters. The main objective of engine mapping is optimizing engine parameters due to desired restrictions, which is called model-based calibration. The benefits of the calibration methodologies utilising a model based approach both enable the calibration engineer to visually evaluate the parameter interactions in a multidimensional space and also give the ability to evaluate the drive/emissions compromise with no additional testing (Guerrier M., Cawsey P. 2004).

The objective of this study is describing experimental approach for two-stage engine mapping and constructing the specific fuel consumption model of a diesel engine. The two-stage modelling method is supported in model-based calibration toolbox by MATLAB.

2. Two-Stage Modelling

The way of collecting data for the two-stage modelling is to fix engine speed, and torque within each test and sweep cam angle from minimum to maximum value. This type of data collection has two sources of variation. The first source of variation is within each cam angle sweep, when the engine speed and torque are held constant, and it is called local. The second source of variation is between the cam angle sweeps when the engine speed, and torque change, and this is called global. The specification of the diesel engine used for this study is shown in Table-1

Two-stage modelling estimates the local and global responses separately by fitting local and global models in two stages. A local model is fitted to each cam angle sweep independently, and the results of these local models are used to fit global model across all the global variables. Once the global model has been estimated, it can be used to estimate the local models' parameters for any engine speed, and torque values (Model Browser User's Guide).

The least square method is used to estimate the coefficients of both local and global models. This method chooses the coefficients of the models so that the sum of squares of the errors is minimized (Kazan R, Taymaz I, Gokce M).

3. Experimental Study

The data used in this study is collected at a test bench in a workshop. The engine test bench and the screen of control console are shown in Fig-1 and Fig-2 respectively

The different values for both engine speed and torque are adjusted manually by the help of the control console, and the cam angle is adjusted mechanically by using the marks on the flywheel of the engine as shown in Fig-3.

After each cam angle changes, the fuel pump's injection time must be also adjusted. This adjustment is done also mechanically as shown in Fig-4.

The different combinations of engine speed and torque are tried for each cam angle sweeps, and the specific fuel consumption is measured for each measurement point. The measurement set up is shown in Table-2.

4. Modelling the Engine

After the data is collected, the data is transformed in to excel format to be used in the toolbox. The algorithm used in two-stage modeling approach is shown in Fig-5.

The global inputs are engine speed and torque whereas local input is cam angle, which is swept from maximum to minimum values, and the response is the specific fuel consumption.

There are different types of functions for both local and global model that can be chosen by the engineer. Once the local model type is chosen, the curve is fitted for each cam sweep as shown in Fig-6.

The dark points are the measured specific fuel consumption for the cam angles, and the curve is the fitted curve for quadratic function.

The model definition is given for each local model, which is given below for test no:7;

$$spefuelcon = 897.737 + 2.793 \times C - 51.388 \times C^2 \quad (1)$$

where,

$spefuelcon$: specific fuel consumption

C : cam angle.

The local model definition is evaluated for each cam sweep, which is 90 for this study. This is the first step of two-stage modeling. Afterwards, the global coefficient of the model is evaluated by using the coefficients of each model, which is the second step of two-stage modeling.

At the end of modeling, the equation for specific fuel consumption is evaluated as shown below;

$$spefuelcon = a1 + a2 \times C + a3 \times C^2 \quad (2)$$

where $a1, a2,$ and $a3$ are calculated in terms of engine speed and torque. In other terms, first $a1, a2,$ and $a3$ shall be calculated for any engine speed and torque, then the specific fuel consumption can be evaluated for any cam angle by using Eq. (2).

The more detailed explanation of two-stage engine mapping for CO emission response is presented in Ref (Tabak S, 2007) which is very similar to specific fuel consumption model.

The different model types are tried for specific fuel consumption response and the best model among these models is chosen by using the statistic parameters given by the toolbox, which are root mean squared error (RMSE) and predicted sum of squares (PRESS) RMSE.

RMSE indicates how well the curve is fitted to the measurement points, whereas PRESSS RMSE shows how well the model evaluates the measurement model if it is included during the measurement.

The calculated statistical parameters for different models are shown in Table-3.

The best model is chosen as model "D" in Table-3, because it has the lowest RMSE and PRESS RMSE values.

The 3-D view of the best chosen model is displayed in Fig-7.

5. Results and Discussions

The most benefit of two-stage modelling is the ability to choose different function types for local and global models, which decreases the model's RMSE value, whereas one function type can be chosen during current one-stage modelling.

The outliers are displayed during modelling, and the engineer can remove these outliers during modelling to improve the models (Kozan R., Gokce M. 2009). However this must be done very carefully, because the removed data can be very specific character of the engine.

Two-stage engine mapping is the first step of model-based calibration. Since the model is created, this model can be used in CAGE browser of the toolbox to optimize the cam angles for desired objectives.

References

Guerrier M.,Cawsey P., (2004). "The Development of Model Based Methodologies for Gasoline IC Engine Calibration", SAE Technical Paper Series, 2004-01-1446.

Kazan R, Taymaz I, Gokce M, "The Comparison of Two-Stage and One-Stage Engine Mapping", European Journal of Scientific Research, Vol 20, pp 24-36

Kozan R., Gokce M., "Two-stage Engine Mapping for the Calibration of Carbon Monoxide Emission", Modern Applied Science, Vol 3, No 4, April 2009

Model Browser User's Guide, Model-Based Calibration Toolbox, MATLAB

Tabak S, "Diesel Engine Calibration Approach with Two-Stage Modelling Approach", MSc Thesis, Sakarya University, May 2007.

Table 1. The specification of the diesel engine

Cylinder Number	10
Cylinder Inner Diameter	165 mm
Stroke	175 mm
Compression Ratio	1:18 – 1:19.5
Maximum Power	2200 rpm, 610 KW (830 HP)
Maximum Engine Speed	2400 rpm without load

Table 2. The measurement set up

Cam Angle (^{o})	**Torque (Nm)**	**Speed (rpm)**
-10, -8, -6, -4, -2, 2, 4, 6, 8, 10	200	850, 1000, 1200, 1400, 1600, 1800, 2000, 2200, 2400, 2480
	400	850, 1000, 1200, 1400, 1600, 1800, 2000, 2200, 2400, 2480
	600	850, 1000, 1200, 1400, 1600, 1800, 2000, 2200, 2400, 2480
	800	850, 1000, 1200, 1400, 1600, 1800, 2000, 2200, 2400, 2480
	1000	850, 1000, 1200, 1400, 1600, 1800, 2000, 2200, 2400, 2480
	1200	850, 1000, 1200, 1400, 1600, 1800, 2000, 2200, 2400, 2480
	1400	850, 1000, 1200, 1400, 1600, 1800, 2000, 2200, 2400, 2480
	1600	850, 1000, 1200, 1400, 1600, 1800, 2000, 2200, 2400, 2480
	1800	850, 1000, 1200, 1400, 1600, 1800, 2000, 2200, 2400, 2480
	2000	850, 1000, 1200, 1400, 1600, 1800, 2000, 2200, 2400, 2480

Table 3. The statistics of the investigated models

Model	Local Model	Global Model	Local RMSE	Two-stage RMSE	PRESS RMSE
A	Quadratic	Quadratic	29.99	66.11	72.78
B	Cubic	Quadratic	29.99	49.26	55.28
C	Cubic	Cubic	31.23	42.20	48.37
D	Cubic	Poly_4	31.23	34.65	39.84

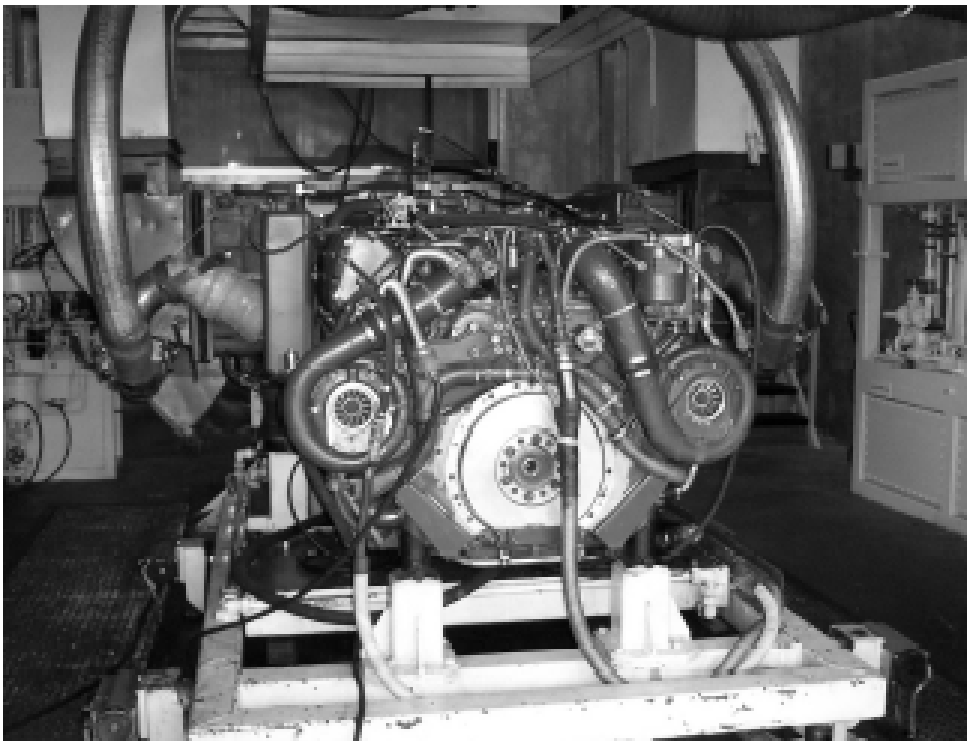

Figure 1.The engine test bench [4]

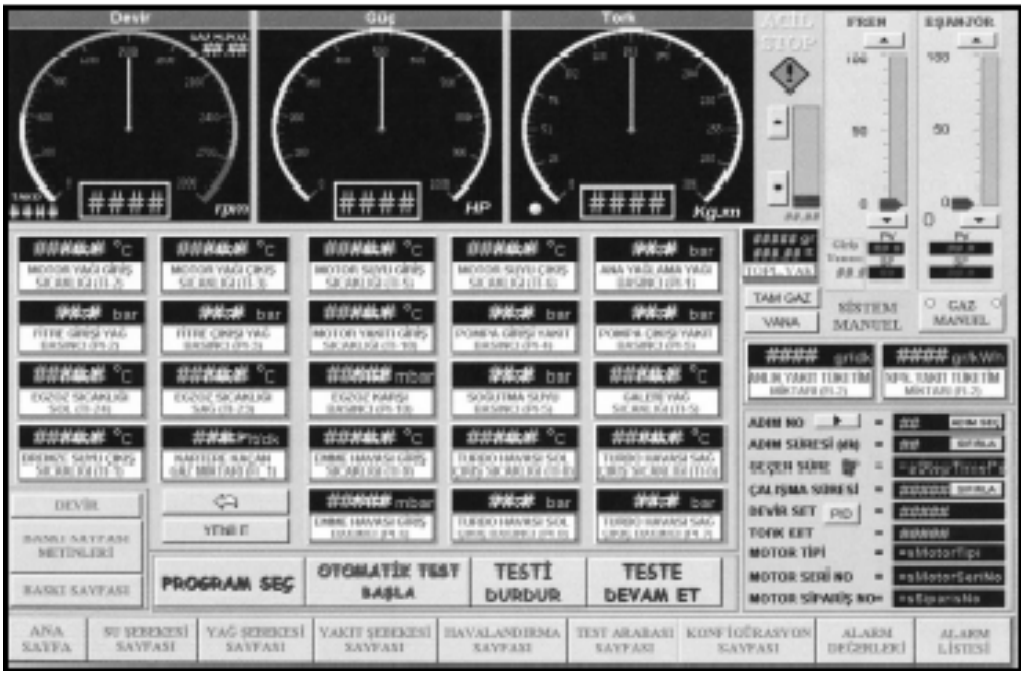

Figure 2. The screen of control console [4]

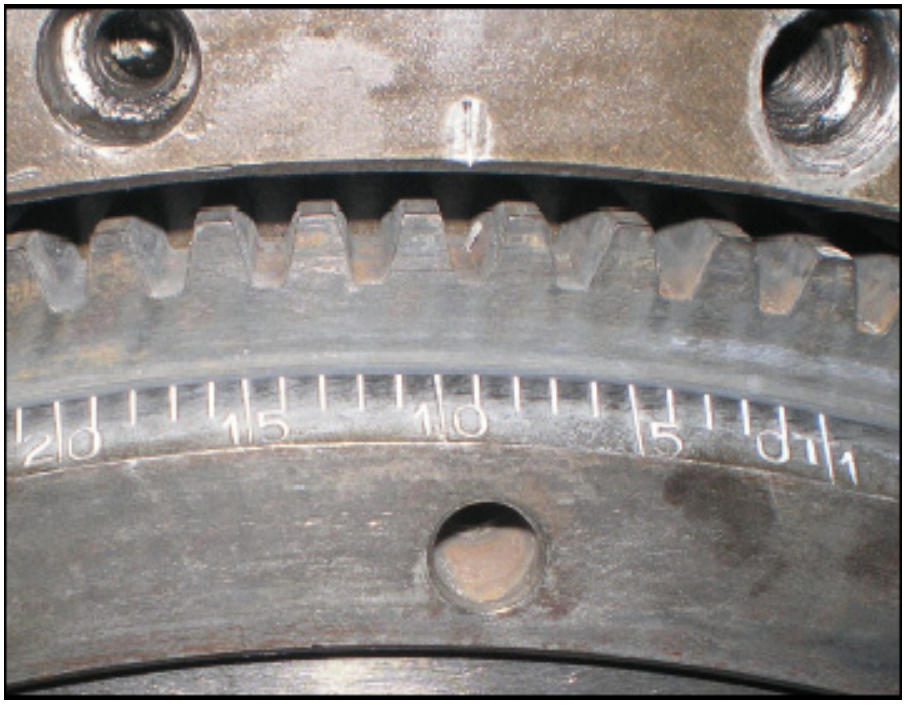

Figure 3.The cam angle degree marks on flywheel [4]

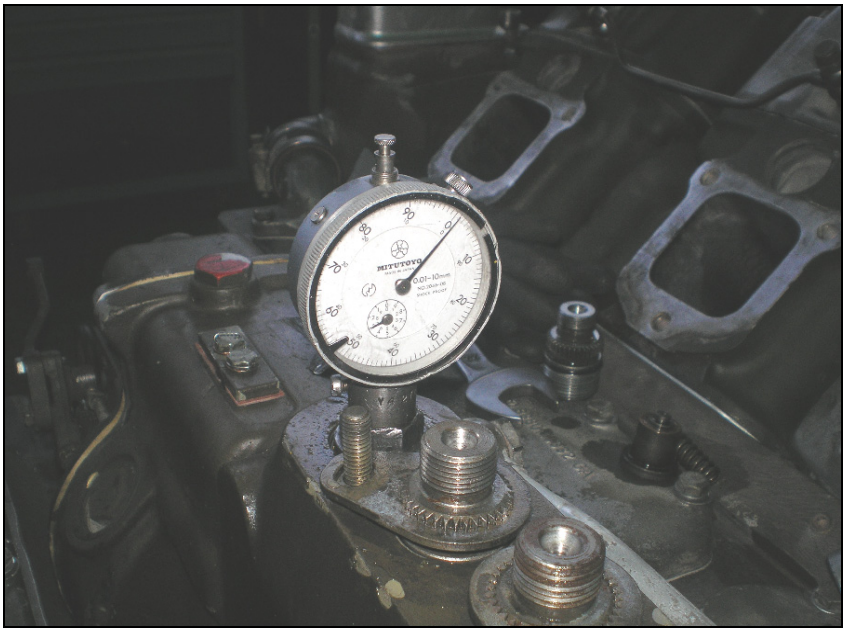

Figure 4. The mechanical adjustment of fuel pump [4]

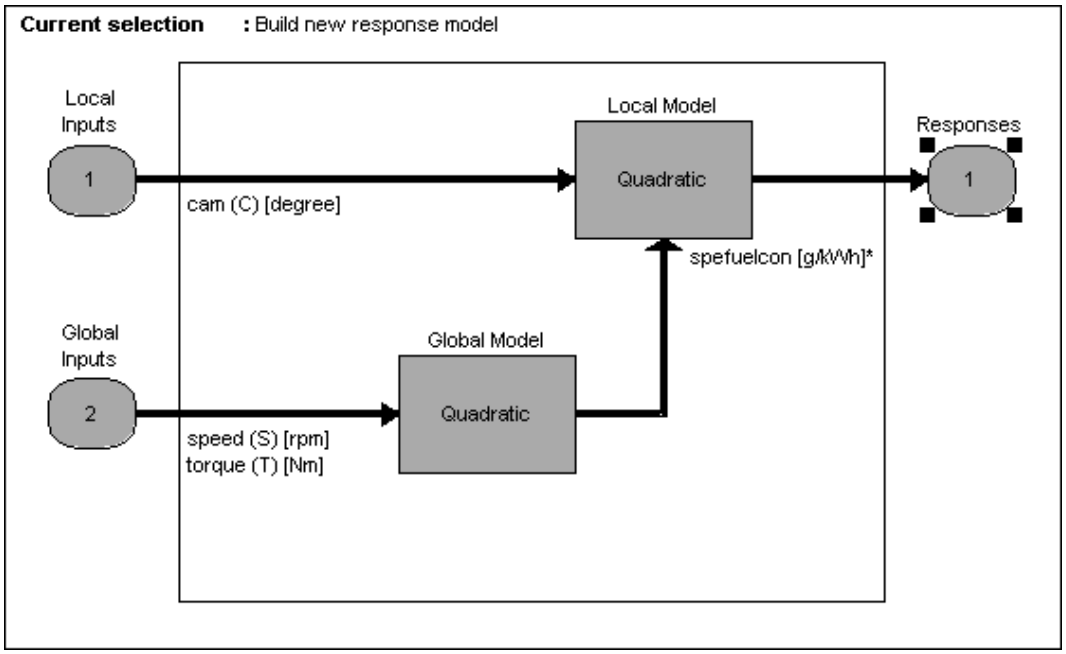

Figure 5. The algorithm for two-stage modelling

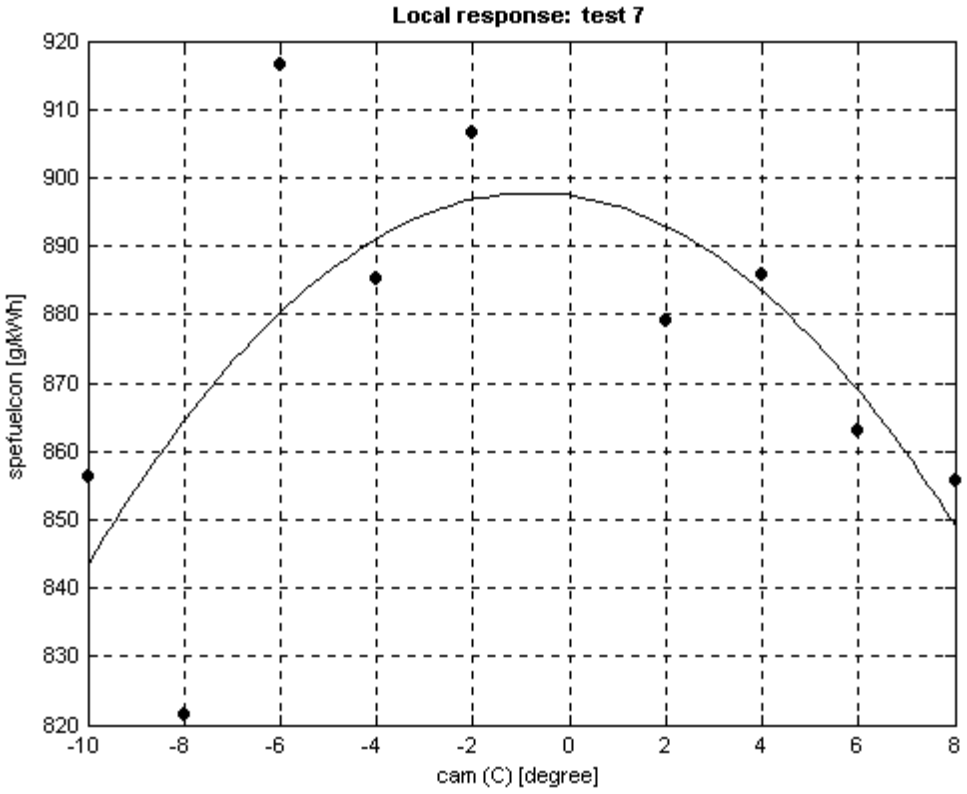

Figure 6. The fitted local quadratic function for test no:7

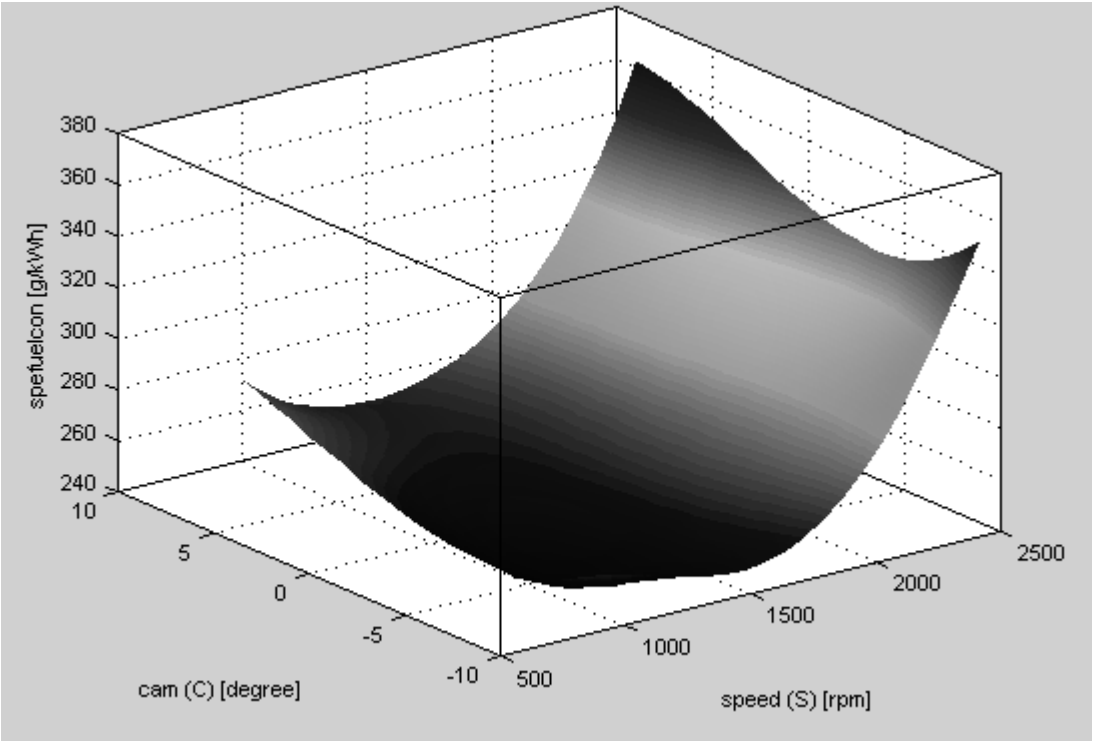

Figure 7. The response surface of the best-chosen model

Modern Applied Science

www.ccsenet.org/journal.html

Vol. 3, No. 3

March 2009

The Wehrl's Entorpy of Schrödinger-cat States

Jingqiu Chen (Corresponding author)

Institute of Optoelectronics Science and Engineering

Huazhong University of Science and Technology

Wuhan 430074, China

College of Physics Science and Technology

Shenzhen University

Guangdong 518060, China

E-mail: chenjq@szu.edu.cn

Qiao Gu

International Institute of Biophysics

Kaiserslautern100004, Germany

Wenda Peng

Institute of Optoelectronics, Shenzhen University

Guangdong 518060, China

Abstract

The Wehrl's entropy of the Schrödinger-cat states has been calculated numerically in this paper. In particular, we show the dependence of the Wehrl's entropy on the two parameters of the Schrödinger-cat states, which act as, respectively, the photon number parameter α and the phase difference ϕ. The Wehrl's entropy has been found to be in the range $1 \le W < 1.7$, and its changes with respect to α, ϕ are not homogenized. Furthermore, we obtain both the dependence of the Wehrl's entropy on the average photon number and the relation between the Wehrl's entropy and the statistical entropy.

Keywords: Wehrl's entropy, Schrödinger-cat states, Statistical entropy

1. Introduction

Entropy is a crucial concept in the thermodynamics, statistical mechanics and information theory. Its sovereign role regarding the behavior of macroscopic systems was recognized about one century ago by Clausius, Kelvin, Maxwell, Boltzmann and many others. Traditionally, entropy is derived from thermodynamically phenomenological consideration based upon the second law of thermodynamics. Entropy relates macroscopic and microscopic aspects of nature and determines the behavior of macroscopic systems.

In quantum statistical mechanics entropy is defined by von Neumann in terms of the density operator as (E.T.Jaynes R.D.Levine and M.Tribus, 1978).

$$S = -\mathrm{Tr}\rho\ln\rho \tag{1.1}$$

where ρ is density operator.

However, the quantum entropy has the problem that it gives the zero value for all pure states, whether or not they are classical or non-classical. Wehrl introduced a new definition of entropy for radiation filed in terms of coherent states by (A Wehrl, 1979)

$$W = -\frac{1}{\pi}\int Q(\beta)\ln Q(\beta)d^2\beta \tag{1.2 a}$$

where

$$Q(\beta) = \langle\beta|\rho|\beta\rangle \tag{1.2 b}$$

are the diagonal elements of the density operator in coherent states $|\beta\rangle$, subject to the constraint

$$\int Q(\beta)d^2\beta = \pi \tag{1.2 c}$$

We recognized that $Q(\beta)$ is exactly the distribution function corresponding to the antinormally ordering of operators, and it is called the Q representation. The Wehrl entropy has bellow characteristics:

(1) The Q representation is always non-negative.

(2) $Q(\beta)$ is a bounded function lying within unit. Thus $Q(\beta)$ serves as a standard distribution function since $0 \le Q(\beta) \le 1$.

(3) As a c-number form, it is calculated much more easily than the quantum entropy**.**

The different pure states may be distinguished in terms of the Wehrl entropy. It takes its minimum value $W = 1$ for coherent states. This may be used as a reference to measure the degree of squeezed states (C.T.Lee, 1988).

Qrlowski (Arkadiusz Orlowski, 1993) discussed the Wehrl's entropy of the two-photon coherent states (squeezed states), photon-number states, ideal laser light, chaotic (thermal) radiation, and displaced photon-number states. They are fond to displace the same shape respect to the average photon number $\langle N\rangle$**.** Then Qrlowski pointed out that the Wehrl's entropy can be considered as a good measure of the strength of the coherent component and there is a possibility of using the Wehrl's entropy as a reasonable classification of quantum states.

The difficulty with the quantum entropy and the Wehrl's entropy lies in the fact that they remain immeasurable at present. Actually, neither eigenvalues of a density operator or its Q representation have yet been found to be measurable by present quantum optical technique, although some possible methods have proposed (L.Knoll and A.Orlowski, 1995). However, the statistical entropy (Qiao, Gu, 2003) can be measured by means of the photon counting data.

A question may be put as follows: whether Wehrl's entropy of Schrödinger-cat states displace the same shape respect to the average photon number $\langle N\rangle$ as (Arkadiusz Orlowski, 1993)?whether statistical entropy of the Schrödinger-cat states can replace the Wehrl's entropy to describe the coherence of such states (Qiao, Gu, 2003)? To answer these questions, there are three main works in the present paper.

Firstly, we calculate the Wehrl's entropy of the Schrödinger-cat states.

Secondly, we discuss the dependence of the Wehrl's entropy of the Schrödinger-cat states on the average photon number.

Thirdly, we discuss the relation of the Wehrl's entropy and the statistical entropy.

2. The Wehrl's Entropy of the Schrödinger-cat states

2.1 Calculation of the Wehrl's Entropy of the Schrödinger-cat states

The Schrödinger-cat states have the explicit definition: it is a quantum superposition of two macroscopically distinguishable states. The Schrödinger cat states can be formulated in different ways [6]. One of them is expressed by

$$|\alpha_c\rangle = \frac{1}{\sqrt{A}}[|\alpha_1\rangle + |\alpha_2\rangle] \tag{2.1 a}$$

where $|\alpha_1\rangle$ and $|\alpha_2\rangle$ are coherent states, which have the same amplitude $|\alpha|$ but different phases, that is

$$\alpha_1 = |\alpha|e^{i\phi_1}, \quad \alpha_2 = |\alpha|e^{i\phi_2} \tag{2.1 b}$$

The normalization constant A is determined by $\langle\alpha_c|\alpha_c\rangle = 1$

For simplicity, we take $\phi_1 = 0$ and $\phi_2 = \phi$, so ϕ acts as a phase difference

We can get that

$$A = 2 + 2\exp(-|\alpha|^2 + |\alpha|^2\cos\phi)\cos(|\alpha|^2\sin\phi) \tag{2.2}$$

Now we calculate the Wehrl's entropy for density operator

$$\rho = |\alpha_c\rangle\langle\alpha_c| \tag{2.3}$$

For this purpose, we first write the distribution function in terms of $\alpha = r\exp(i\theta)$.

From (1.2), a straightforward and strenuous calculation gives

$$W = -\frac{1}{\pi}\int Q(\alpha)\ln Q(\alpha)d^2\alpha \tag{2.4}$$

$Q(\alpha) = \frac{1}{A}(B + C + D);$

where

$B = \exp(-r^2 - \alpha^2 + 2r\alpha\cos\theta)$

$C = 2\exp(E)\cos(r\alpha F)$

$D = \exp(-r^2 - \alpha^2 + 2r\alpha\cos(\theta - \phi))$

$E = -r^2 - \alpha^2 + r\alpha\cos\theta + r\alpha\cos(\theta - \phi)$

$F = \sin(\theta - \phi) - \sin\theta$

From (2.4), we know that the Wehrl' entropy depends on the parameters α and ϕ .In the present case, the Wehrl' entropy cannot be calculate analytically, but it can be evaluated numerically.

2.2 Discussing the results

From Fig.1to Fig.5, we can get many information concerning the Wehrl's entropy of the Schrödinger-cat states.

(1) The values of the Wehrl's entropy of the Schrödinger-cat states have a limit: $1 \le W < 1.7$.

(2) The wehrl's entropy with respect to α and ϕ have different characters.

3. Dependence of the Wehrl's Entropy on the Average Photon Number

The average photon number is given generally by

$$N = \langle a^+ a \rangle = \mathrm{tr}(\rho a^+ a) \tag{3.1}$$

Substituting the (2.3) into (3.1) and calculating the (3.1) we get :

$$N = \frac{1}{A}2|\alpha|^2[1 + \exp(-|\alpha|^2 + |\alpha|^2\cos\phi)\cos\Delta)] \tag{3.2}$$

where

$\Delta = \cos(\phi + |\alpha|^2\sin\phi)$

On the basis of (3.2), we can calculate numerically the Wehrl's entropy as a function of the average photon number, and the result is shown in Fig.6.

From Fig.5, one can see that the shape of wehrl'entropy with respect to *N* is similar to that in Ref. (Arkadiusz Orlowski, 1993).

4. The Statistical Entropy and The Wehrl's Entropy

We know that Wehrl entropy remains immeasurable at present. However, we can discuss the relation between the statistical entropy and Wehrl's entropy.

Some researchers (V.Perinova,J.Krepelka and J.Perina, 1986) have proposed to use the entropy

$$G = -\sum_{n=0}^{\infty} p(n)\ln p(n) \tag{4.1}$$

as an alternative measurement of entropy for the radiation field on account of the measurability of photon number distribution

$$p(n) = \langle n|\rho|n\rangle . \tag{4.2}$$

Calculating $p(n)$ of the cat states defined by (2.1), we get that:

$$p(n) = \frac{1}{A}\frac{\exp(-|\alpha|^2)|\alpha|^{2n}}{n!}(2 + 2\cos n\phi) \tag{4.3}$$

Substituting (4.3) into (4.1), we can get the statistical entropy of the cat states. The numerical result is shown in Fig7.

We can distinctly conclude that wehrl's entropy and the statistical entropy is the one-to-one corresponding relation. So cat states can be can described by statistical entropy as wehrl' entropy do.

5. Brief summary

We get the dependence of Wehrl's entropy of cat states on two parameters α,ϕ. Wehrl's entropy has a limit ($1 \le W < 1.7$) and the density of Wehrl's entropy respect to α,ϕ are not homogenized.

The Wehrl's entropy can classify cat states. Both the average photon number and the statistical entropy are one to one relation to Wehrl's entropy, so Wehrl' entropy can replace to both the average photon number and the statistical entropy to describe the cat states.

Acknowledgements

I am grateful to Dr.Yu yunjin for many interesting discussions.

References

A Wehrl, (1979). *On the relation between classical and quantum –mechanical entropy*. Rep. Math. Phys, 1979, 16: 353-358.

Arkadiusz Orlowski Phys. RevA, (1993). 48:727-730.

C.T.Lee, (1988). *Wehrl's entropy as a measure of squeezing*. Opt. comm., (1988). 66: 52-54.

E.T.Jaynes R.D.Levine and M.Tribus. (1978). *we stand on maximum entropy?*. Canbridge: The MIT Press, 1978. pp.15-118.

L.Knoll and A.Orlowski, (1995). *Distance between density operators: Applications to the Jaynes-Cummings model*. Phy.rev.A, 1995, 51: 1622-1630.

Qiao Gu ,Radiation and Bioinformation. (2003). Beijing: Scince Press, 2003.

V.Perinova, J.Krepelka and J.Perina, (1986). *Entropy of optical field*, Optica Acta, 1986, 33:15-32.

Vlatko Vedral, (2006). *Mordern Foundations of Quantum. Optics*.shanghai:fudan university press, 2006, P24.

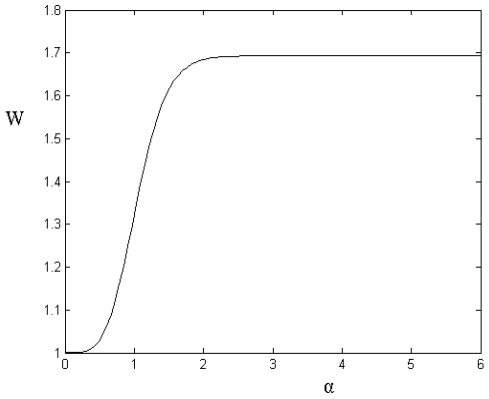

Figure 1. Wehrl's entropy with respect to α, where $\phi = \pi$.

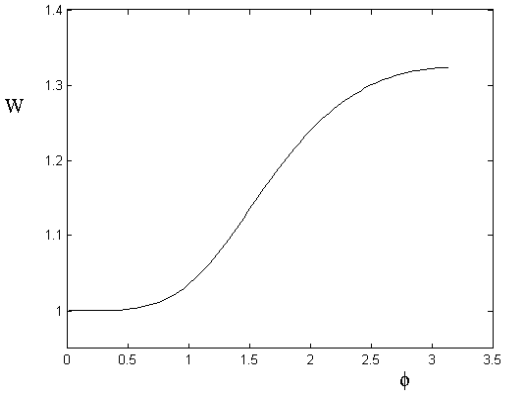

Figure 2. Wehrl's entropy with respect to ϕ, where $\alpha = 1$.

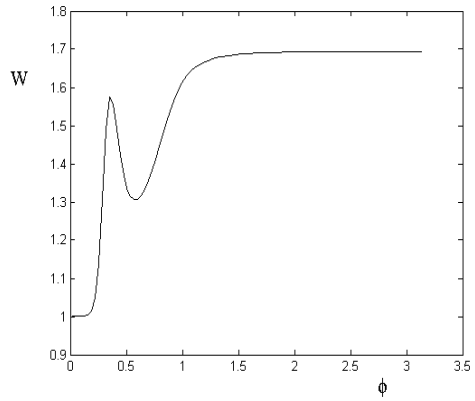

Figure 3. Wehrl's entropy with respect to ϕ ,where $\alpha = 3$.

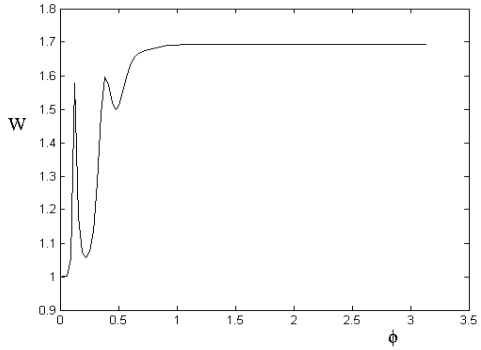

Figure 4. wehrl's entropy respect to ϕ , where $\alpha = 5$.

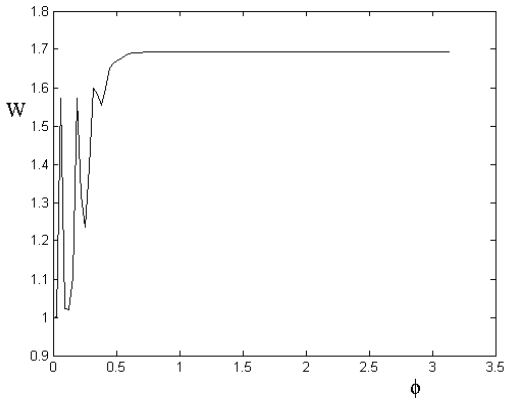

Figure 5. Wehrl's entropy respect to ϕ , where $\alpha = 7$.

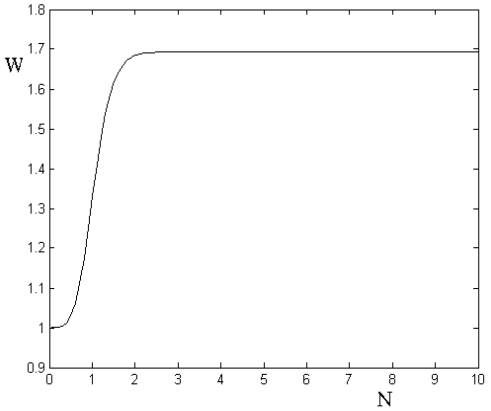

Figure 6. Wehrl's entropy with respect to *N*.

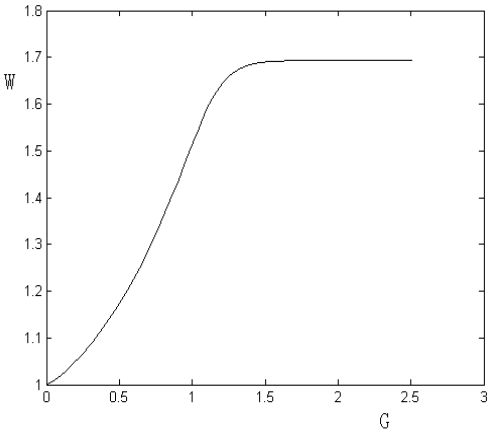

Figure 7. The relation between the Wehrl's entropy and the statistical entropy.

Modern Applied Science

www.ccsenet.org/journal.html

Vol. 3, No. 3

March 2009

Speed Estimation in Forward Scattering Radar by Using Standard Deviation Method

Mutaz Salah, MFA Rasid & RSA Raja Abdullah

Department of Computer and Communication Engineering

Universiti Putra Malaysia (UPM)

43400 Serdang, Selangor, Malaysia

Tel: 60-3-8946-4347

E-mail: rsa@eng.upm.edu.my,fadlee@eng.upm.edu.my mutazoya@hotmail.com

M Cherniakov

School of Electronic, Electrical & ComputerEngineering

The University of Birmingham

Edgbaston, United Kingdom

Abstract

Forward Scattering Radar (FSR) is a special type of Radar. The interest in FSR is rises after its capability in target classification is validated. Unfortunately, the speed of the target still not been solved. Thus, this paper proposed a method to estimate speed FSR system. The theory of FSR systems is briefly described together with practical experiments to evaluate the feasibility of such a system in real-life scenarios. All data are collected from the practical experimentation by using typical ground vehicle as target (e.g. car, lorry). In the proposed system, Standard Deviation for each raw radar signal is calculated. This Standard Deviation information is exploited to estimate the speed of a target. This method shows a good result in estimating the vehicle speed crossing FSR baseline. By analyzing 850 experimentally obtained car signatures, the performance of the system is evaluated and the effectiveness of the system is confirmed.

Keywords: Forward scattering radar, Standard Deviation method and speed estimation

1. Introduction

There are different types of radar systems based on the transmitter-receiver topology as shown in Figure 1. Forward scattering radar (FSR) is a special mode of bistatic radar that can be used for target detection and classification. FSR offer a number of interesting features such as: relatively simple hardware (Gould, D.M., Orton, R.S., Pollard, R.J.E., 2002)(Willis N. J., 1995); an enhanced target radar cross section (compared to traditional radar)(Chernyak, 1998); a long coherent interval of the receiving signal; robustness to stealth technology and possible operation using non-cooperative transmitters. Recent research has shown its capability in target classification (M. Cherniakov, R.S.A.R. Abdullah, P. Janc˘ovic˘, M. Salous and V. Chapursky, 2006)(Abdullah R., Cherniakov M., Jancovic P. 2004)(M Cherniakov, Salous, Kostylev and RSA Abdullah. 2005)(M Cherniakov, V.V Chapurskiy, RSA Raja Abdullah, P.Jancovic, M. Salous. 2004)(RSA Raja Abdullah, M Cherniakov, 2003). Although FSR has an advantage compared to the traditional radar, but it also has number of known drawbacks, such as the absence of range resolution and narrow operational area, etc.

In references (M. Cherniakov, R.S.A.R. Abdullah, P. Janc˘ovic˘, M. Salous and V. Chapursky, 2006) which describe the automatic target detection using FSR, the speed is estimated by analyzing the information from the video camera. Thus, this paper is filling the gap towards the current research in FSR by estimating the speed of a target. The information from the Standard deviation of a raw radar signal is analyzed to predict the speed of a target crossing the FSR baseline. It is shown that using these techniques the speed can be effectively estimated. This paper is dedicated to the experimental study of the feasibility of FSR and its' application for target (ground vehicle) speed estimation. It introduces the radar system itself, fundamental theoretical analysis, and the targets speed in relation to Doppler frequency. By using FSR for detection and classification of ground targets together with the low cost system, it could find various applications in civil, defense, medical and security systems.

2. Forward Scattering Radar basics

Before the speed estimation procedure is described in detail, this section summarizes the basic technical of FSR in terms of signal scattered and power budget. More detail about this subject can be found in (M. Cherniakov, R.S.A.R. Abdullah, P. Janc˘ovic˘, M. Salous and V. Chapursky, 2006) for FSR theoretical background and in (Sizov, V; Cherniakov, M.; Antoniou, M, 2007) for power budget analysis. References(M. Cherniakov, R.S.A.R. Abdullah, P. Janc˘ovic˘, M. Salous and V. Chapursky, 2006)(Abdullah R., Cherniakov M., Jancovic P. 2004)(M Cherniakov, Salous, Kostylev and RSA Abdullah. 2005)(M Cherniakov, V.V Chapurskiy, RSA Raja Abdullah, P.Jancovic, M. Salous. 2004)(RSA Raja Abdullah, M Cherniakov, 2003). (Blackman, A.B., Ryndyk, A.G., and Sidorov, S.B. 2000)(Chapurskiy V.V, Sablin V.N. 2000) have elaborate on the basic FSR system and it is shown again in Figure 2. It is comprises of a transmitter, Tx with f_c central frequency with an appropriate wavelength, λ and a receiver, Rx separated by a distance, b from the transmitter. The target is assumed to be moving along a trajectory that crosses the baseline with speed, V and has zero elevation as the system operates in a ground plane. For a moving target, the received signal experiences Doppler shift, f_{dbr} and can be evaluated as (M. Cherniakov, R.S.A.R. Abdullah, P. Janc˘ovic˘, M. Salous and V. Chapursky, 2006):

$$f_{dbr} = 2V\frac{1}{\lambda}\cos\delta\cos(\beta/2) \tag{1}$$

where β is the bistatic angle.

The maximum Doppler shift occurs for the target trajectory normal (perpendicular) to the baseline. Even in this case, the absolute value of f_{dbr} is essentially less than its maximal rate fdmax = 2V/λ corresponding to a monostatic radar. The information from the scattered Doppler frequency is used in further processing for target classification from the assumption that a unique target possesses a unique Doppler signature in frequency domain (M. Cherniakov, R.S.A.R. Abdullah, P. Janc˘ovic˘, M. Salous and V. Chapursky, 2006). The Doppler shift depends mainly on the target velocity vector components and the carrier frequency. The general equation that describes the received waveform, that is, target signature from the moving sample target with a rectangular shape is described in (RSA Raja Abdullah, M Cherniakov, 2003).

It is expected that the boundary for FSR is around $\beta \sim 170^o$. At the time when the bistatic angle β approaches to 180^o, the target blocks part of the transmitted signal, which leads to a reduction of the received signal power. In this case, the target acts as an aperture antenna with a maximum gain as (RSA Raja Abdullah, M Cherniakov, 2003):

$$G = \frac{4\pi A}{\lambda^2} \tag{2}$$

where the signal wavelength, λ is assumed to be small compared to the target's dimensions, and $\boldsymbol{A}$ is the target shadow silhouette area projection on the transmitter-target line. When $\beta = 180^o$, the level of received signal reaches its maximum and the target can be characterized by a forward scattering cross-section (FSCS), σ_b, which also depends upon the target shadow silhouette area A (RSA Raja Abdullah, M Cherniakov, 2003):

$$\sigma_b = \frac{4\pi A^2}{\lambda^2} \tag{3}$$

The increase in FSCS inherently contributes to the total received signal in the power budget equation (RSA Raja Abdullah, M Cherniakov, 2003).

The reason why the speed information is silence to FSR is illustrated in the Figure 3. Let assume that the transmit time for the two positions of target be $T_o = 0$ sec. The received signal scattered by the target arrive at the receiver at the same time regardless of the target position on the FRS baseline, hence the range resolution which is critical parameter to measure speed does not exist in the received signal.

3. Vehicle data collection and speed estimation

An experiment to collect data using real vehicles was carried out on a public road using the setup shown in Figure 4 (M Cherniakov, V.V Chapurskiy, RSA Raja Abdullah, P.Jancovic, M. Salous. 2004). During this experiment, signals from a random stream of vehicles, as well as a number of test vehicles were collected and recorded. A video recorded the vehicles passing through the beam and allowed the speed with which the vehicles passed through the beam to be calculated. Figure 4 also shows the positioning of the video camera and a typical video scene. Two posts were attached to a tree and a lamppost and have been highlighted in the scene. The two posts were 16m apart. By playing back the recorded video, the speed of a particular vehicle can be evaluated by finding the time taking for the vehicle to travel between the two posts, so we can compare the result of vehicle speed after applying the proposed method with the result from video camera. The Figure 5 shows the example of received signal in time domain from the experiment for two different vehicles crossing the FSR baseline.

Our aim is to find the vehicle speed when the vehicles cross the sensor or the forward scattering radar system. However, speed information, in general, is not available from the radar signal itself (assuming the length of vehicle is unknown). Therefore, it is necessary to develop a practical algorithm for speed estimation. This section describes the algorithm used during the experimentation.

Vehicle speed was measured using the relationship between the time-domain signature and the speed of the vehicle as estimated from the captured video footage. In order to establish this relationship, the speed of vehicle was associated with the value of standard deviation that calculated to each vehicle signature. Figure 6 shows the example of received signal in time domain for different speeds. The graphs show that as vehicle speed increased, the vehicle's time-domain signature is compressed and vice versa. This indicates that a relationship exists between Standard deviation values for the time domain signal and the speed of vehicle. Thus, Figure 7 illustrates the general block diagram of the proposed method which utilizing the value of Standard Deviation as a steps in estimating the speed of vehicle crossing the FSR sensor.

3.1 Standard Deviation

In probability and statistic, the standard deviation, σ (STD)of a probability distribution is a measure of the spread of its values. It is defined as the square root of the variance which is the average of the squared differences between data points and the mean. STD, σ being the square root of that quantity therefore measures the spread of data about the mean (Berger J.O. 1985). In this paper, a default Matlab code is used to find the STD values for the time-domain signals. The matlab code is denoted by S = Std(X), where X is the time-domain signal and it returns the STD by using equation (4):

$$s = \left(\frac{1}{n-1} \sum_{i=1}^{n} (x_i - \bar{x}) \right)^{1/2} \tag{4}$$

Where

$$\bar{x} = \frac{1}{n} \sum_{i=1}^{n} x_i \tag{5}$$

n is the number of elements in the sample, $\bar{x}$ is the mean average and x is the random variables. The steps to find the STD to the time-domain vehicle signature are shown below:

i. Compute the mean for the data set.
ii. Compute the deviation by subtracting the mean from each value.
iii. Square each individual deviation.
iv. Add up the squared deviations.
v. Divide by one less than the sample size.
vi. Take the square root.

3.2 Relationship between the speed of vehicle and the standard deviation

The assumption to associate the standard deviation value to the vehicle speed is described in this section. The basis of assumption is depending on the Doppler effect which can be described as the change in frequency when either the receiver or the energy source are in motion relative to each other. In the considered case, the source of the scatter field is moving relative to the receiver due to the motion of the vehicle; the frequency of the received signal will be shifted due to the Doppler effect. As the vehicle, in our case, is considered to be moving perpendicular to the baseline, the Doppler shift will vary throughout the vehicle's motion. Figure 8 illustrates the overall FSR system layout as seen from above and at the scene during experimentation.

When the vehicle enters the sensor coverage area from one side (position 'a' in Figure 10), the Doppler shift will be large, reducing to zero as the vehicle reaches the baseline (position 'b'). The Doppler shift then increases again as the vehicle moves towards the other side of the coverage area (position 'c'). So, in theory, the Doppler frequency is larger as the vehicle enters and leaves the sensor coverage area, and the Doppler frequency is zero when the vehicle is on the baseline. Figure 9 shows the variation of the Doppler frequency relative to the scattering point of the vehicle

The general equation that describes the received waveform, i.e. the target signature from the moving sample target is explained in detail in (RSA Raja Abdullah, M Cherniakov, 2003) and it is summarised below:

$$V_y \approx \Re \sin\left(\frac{4\pi v \sin(\alpha)}{\lambda} t \right) \tag{6}$$

where

$$\Re = K_A \frac{lhE_o \cos^2(\alpha)}{2\lambda z_b} \frac{\sin\left(\frac{\pi l \cos(\alpha)}{\lambda}\alpha\right)}{\frac{\pi l \cos(\alpha)}{\lambda}\alpha} \tag{7}$$

l and h are the target's length and height respectively, $\Re$ is the amplitude of the Doppler components, v is the velocity of the sample target passing through the sensor, K_A is the receiving antenna transformation coefficient, z_b is the distance between the target crossing point on the baseline to the receiver and E_o is a constant. This equation was derived for a rectangular shaped target. The Doppler frequency can be extracted by the derivation of the phase component of equation (7) and given by (RSA Raja Abdullah, M Cherniakov, 2003):

$$f_d = \frac{2v}{\lambda}\sin\alpha \tag{8}$$

From equation (8) it is obvious that the Doppler shift depends mainly on the target velocity vector components and the carrier frequency. This Doppler shift can be used for moving target selection (M. Cherniakov, R.S.A.R. Abdullah, P. Janc˘ovic˘, M. Salous and V. Chapursky, 2006). From the above explanation we can see that the Doppler shift is related to the speed of vehicle and this also guide us to find the relation between the standard deviation value and the speed of vehicle because whenever the speed is changing, the value of standard deviation is also changing as shown in Figure 10 for different speeds.

4. Automatic speed estimation structure in FSR

The overall automatic system is divided into two phases: the first phase (known as training phase) is to create a database (Speed vs. Standard deviation) which will generate the final relationship of the two parameters. Here, the information from the video camera is needed as a reference. The next phase is where the speed determination is processed, and it is known as the testing phase. In this phase, the unknown speed is compared with the database which was generated from phase one. Figure 11 illustrates the overall structure

In total, 700 samples for different vehicle with different speeds were used in the training phase and are plotted in Figure 12. This plot (database) will indicate the correlation between the speed and Standard deviation value and for this case a linear relation was generated. A line of 'best fit' was determined for this plot and it is used to find the unknown vehicle speed during testing phase. The line of best fit give the relationship between the value of standard deviation and the speed of the vehicles and for this plot is given by:

$$Vehicle\ speed = 20 * \text{Standard Deviation Value} - 1.5 \tag{9}$$

In the testing phase, the Standard deviation for unknown time domain signal input is calculated in the pre-processing stage. The standard deviation value is then substitute into the equation (9) to find the speed. A total of 150 samples were used in testing phase and Figure 13 shows the plot of using equation (9).

To show that the length of vehicle is not related to the standard deviation, a plot of 30 samples of different vehicle length but with same speed 8.1 m/s as illustrated in Figure 14. The graph shows that the standard deviation values stay the same for different value of vehicle length. To analyze the reliability of the proposed method, this section investigates the Root Mean Square (RMS) Error between the speed estimated from the algorithm and from the video camera. The normalized RMS error is calculated for this data using equation (10) (Pawel L., Thomas H. 2005).

$$Error = \frac{\delta}{mean} = \frac{\left\{\frac{1}{n-1}\sum_{i=1}^{n}\left(x_i - \bar{x}\right)^2\right\}^{\frac{1}{2}}}{\bar{x}} \tag{10}$$

where n is the number of data, σ is standard deviation and $\bar{x} = \frac{1}{n}\sum_{i=1}^{n} x_i$.

For the plot in Figure 14 the RMS error is 22%. This error is acceptable in FSR application especially for classification using FSR system.

5. Conclusion

This paper presents vehicle speed estimation in special mode of radar system known as forward scattering radar. Standard deviation characteristics are utilized to achieve the objective. The value of Standard deviation for each signal is unique for different speed. Thus, it carries information about the speed of the vehicle. This is confirmed by data obtained from practical experiments with a system that was developed in-house. The proposed method shows a better

accuracy compared to the previous method first introduced in (Blackman, A.B., Ryndyk, A.G., and Sidorov, S.B. 2000). This paper also shown that, more hidden information can be possibly extracted from the FSR signal with signal processing techniques.

References

Abdullah R., Cherniakov M., Jancovic P.(2004).Automatic Vehicle Classification in Forward Scattering Radar, *First International Workshop on Intelligent Transportation WIT* Hamburg, Germany, *Proceedings* pp. 7-12.

Berger J.O. (1985).”Statistical Decision Theory and Bayesian Analysis.” Springer-Verlag 2nd, ISBN 3540960988

Blackman, A.B., Ryndyk, A.G., and Sidorov, S.B.(2000).Forward Scattering Radar Moving Object Coordinate Measurement”. *Int.Radar Conf*.,Washington, DC, USA, pp. 678–682.

Chapurskiy V.V, Sablin V.N.(2000).SISAR: Shadow Inverse Synthetic Aperture Radiolocation, *International Radar Conference*, *The Record of the IEEE 2000 International*, pp. 322 – 328.

Chernyak.(1998). Fundamentals of multisite radar systems. Gordon and Breach Science Publishers.

Gould, D.M., Orton, R.S., Pollard, R.J.E. (2002). Forward Scatter Radar detection, *RADAR 2002*, 15-17 , pp. 36 – 40.

M Cherniakov, Salous, Kostylev and RSA Abdullah. (2005).Analysis of Forward Scattering Radar for Ground Target Detection. *European Radar Conference*, pp.145 – 148.

M Cherniakov, V.V Chapurskiy, RSA Raja Abdullah, P.Jancovic, M. Salous.(2004).Short- Range Forward Scattering Radar, *International Radar Conference*, The Record of the IEEE International, pp. 322 – 328.

M. Cherniakov, R.S.A.R. Abdullah, P. Janc˘ovic˘, M. Salous and V. Chapursky (2006) Automatic ground target classification using forward scattering radar, IEE Proc.- Radar Sonar Navig., Vol. 153, No. 5,

Pawel L., Thomas H. (2005). “Statistics Methods and Applications”, Statsoft Inc, ISBN 1884233597.

RSA Raja Abdullah, M Cherniakov (2003).Forward Scattering Radar For Vehicles Classification ,*VehCom International Conference, VehCom2003*, UK, pp.73-78.

Sizov, V; Cherniakov, M.; Antoniou, M (2007).”Forward Scattering Radar Power Budget Analysis For Ground Targets. Radar, Sonar & Navigation, IET, **1**, Issue 6, pp437 – 446

Willis N. J. (1995) Bistatic Radar *Technology Service Corporation*.

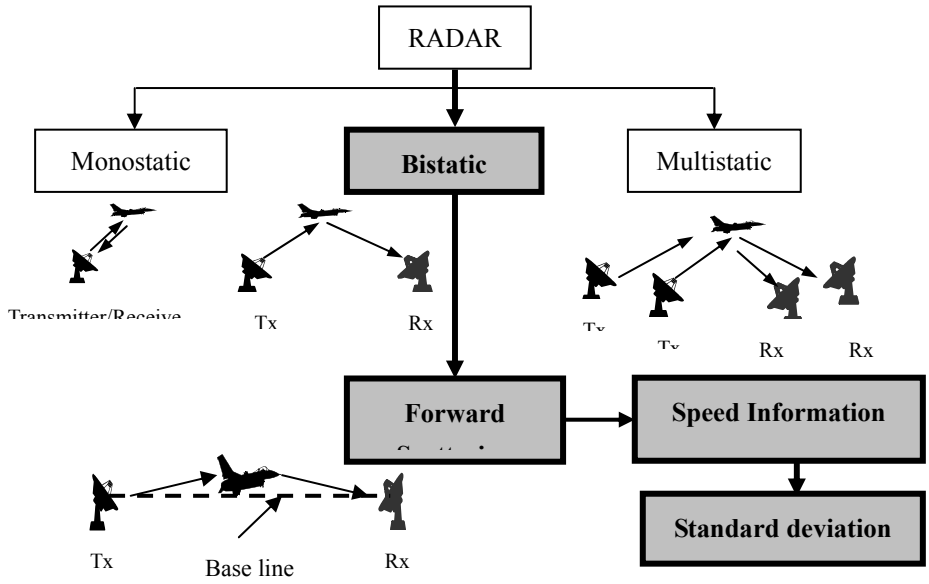

Figure 1. Radar System Classification

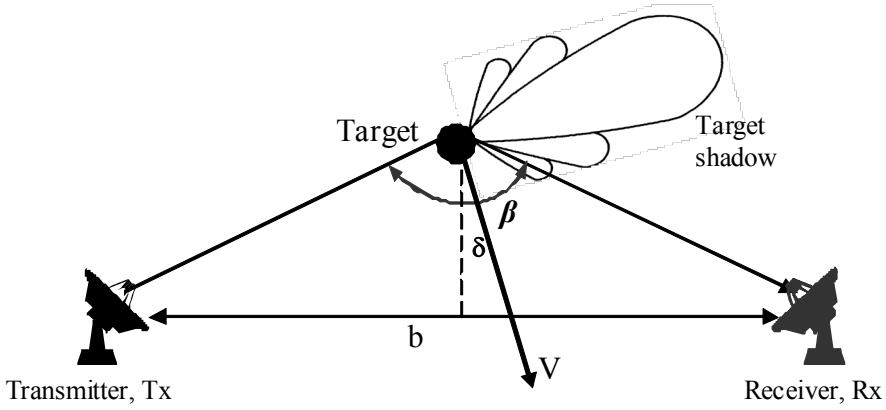

Figure 2. FSR general layout with target trajectory

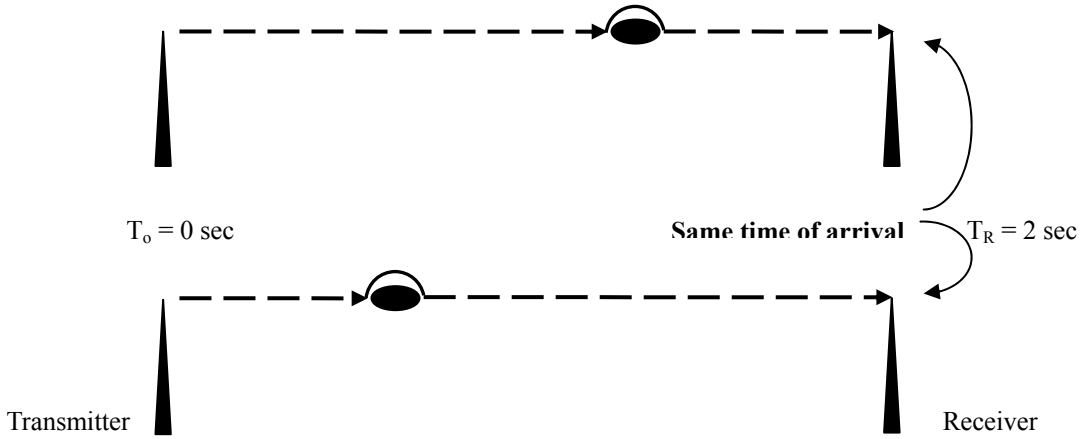

Figure 3. Causes of loss in range resolution

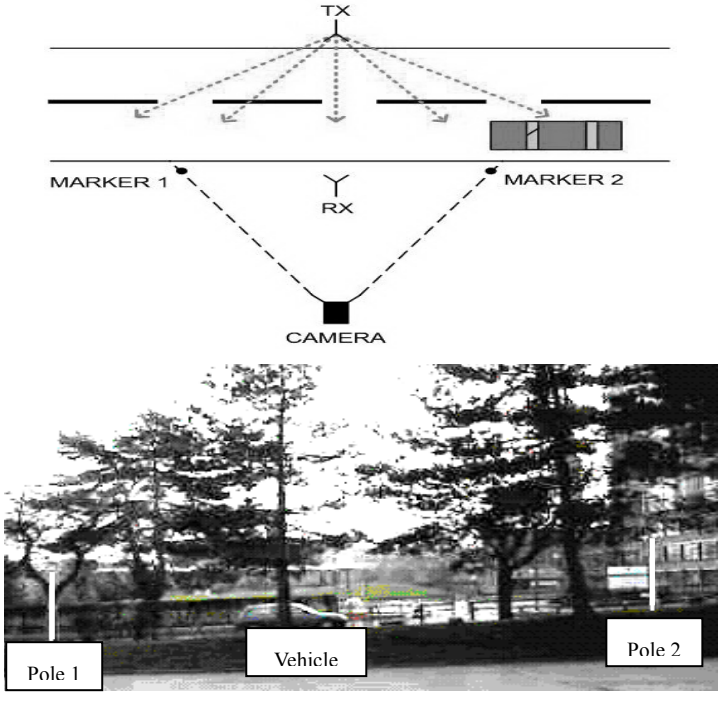

Figure 4. Experimental setup block diagram and typical video from the test day

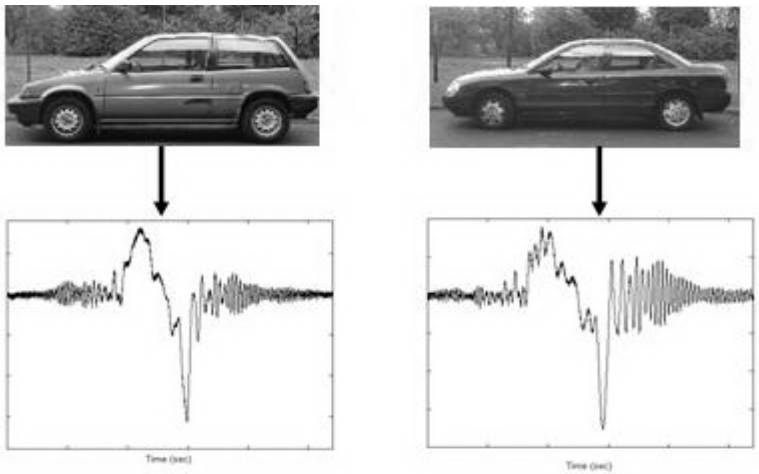

Figure 5. Time domain signals for different vehicle

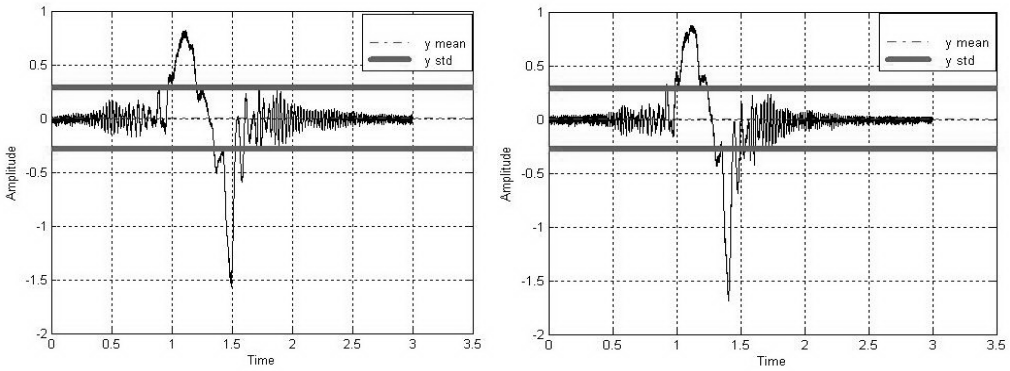

Speed =3.61 m/s, Std = 0.25 Speed = 11.11 m/s, Std = 0.6

Figure 6. Different speed signature and its Standard Deviation

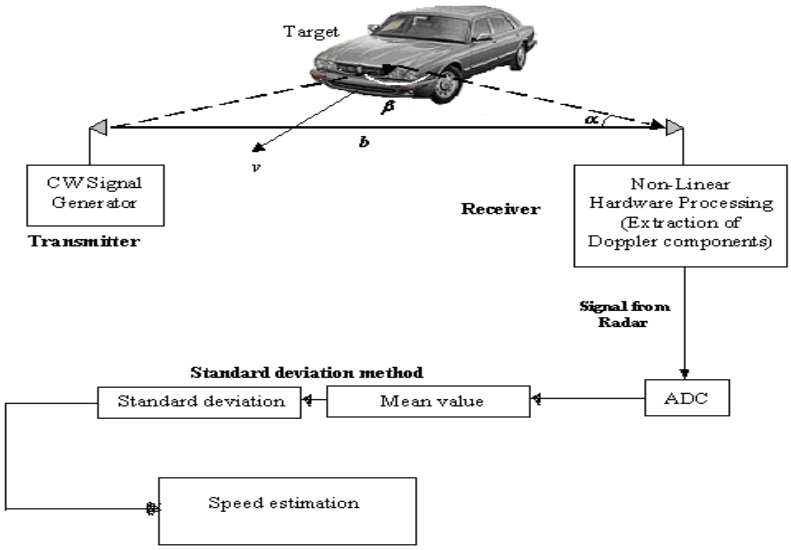

Figure 7. General block diagram for speed estimation in FSR system

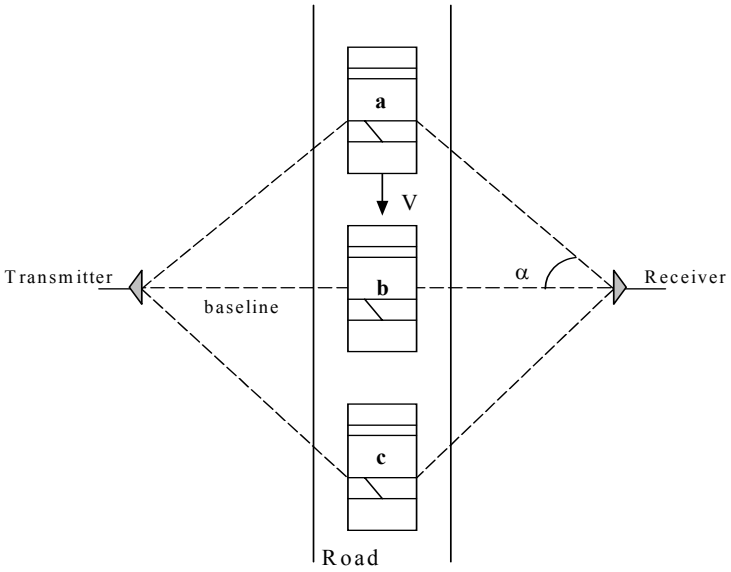

Figure 8. Overall FSR system layout from above (a, b and c are the vehicle positions)

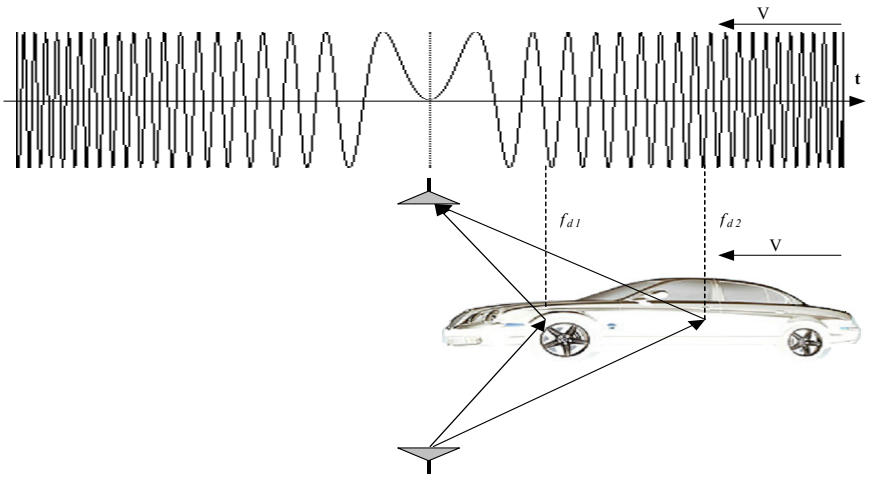

Figure 9. Doppler frequency variation relative to the scattering point on the vehicle

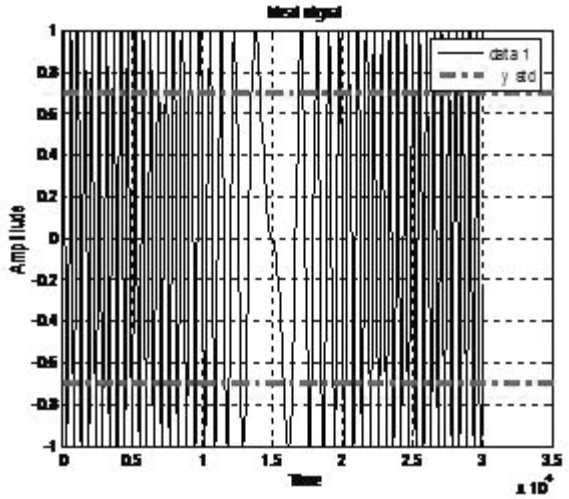

Speed = 7m/s, STD = 0.201

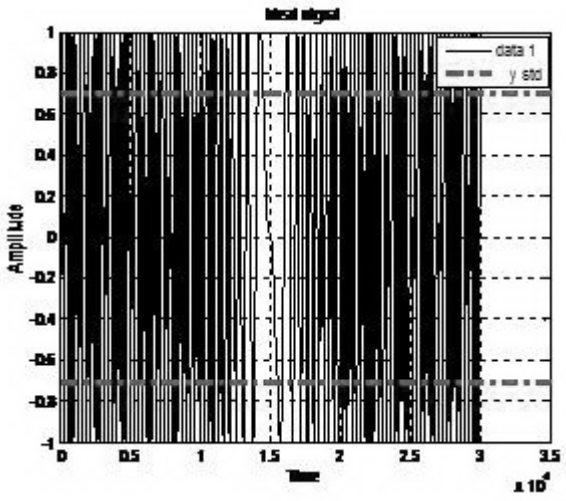

Speed = 12m/s,STD = 0.251

Figure 10. Theoretical Doppler signal for different speed for target with rectangular shape

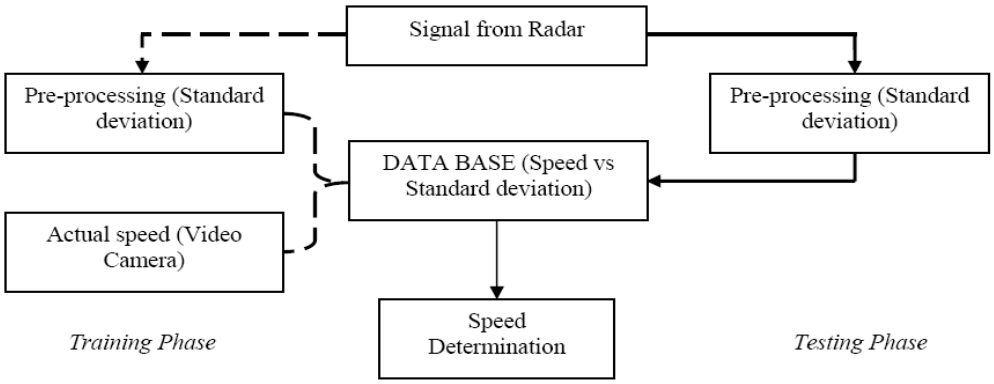

Figure 11. Block diagram for Speed Estimation in FSR

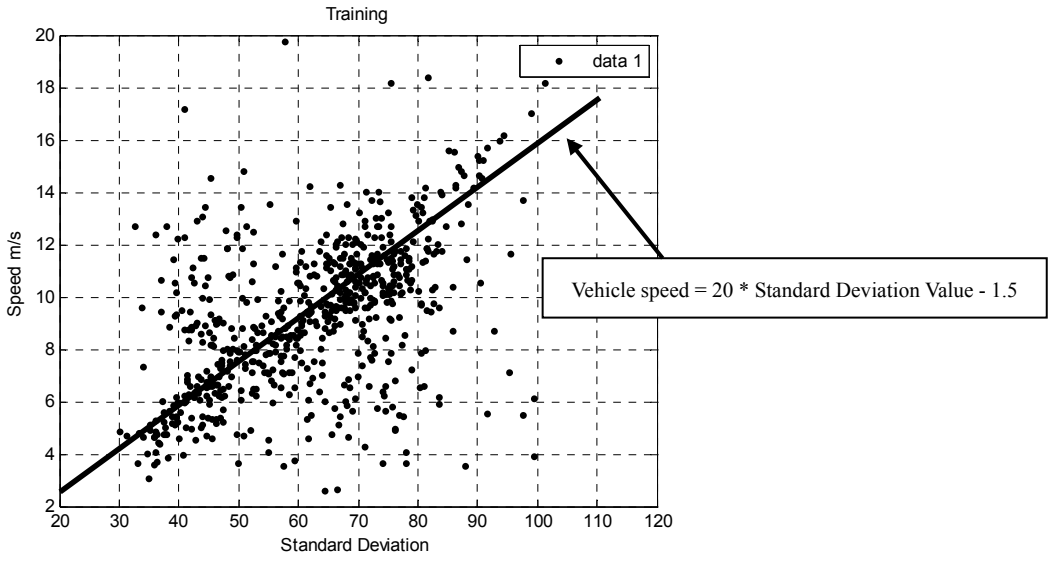

Figure 12. Library of 700 samples for Standard deviation Vs speed of vehicle

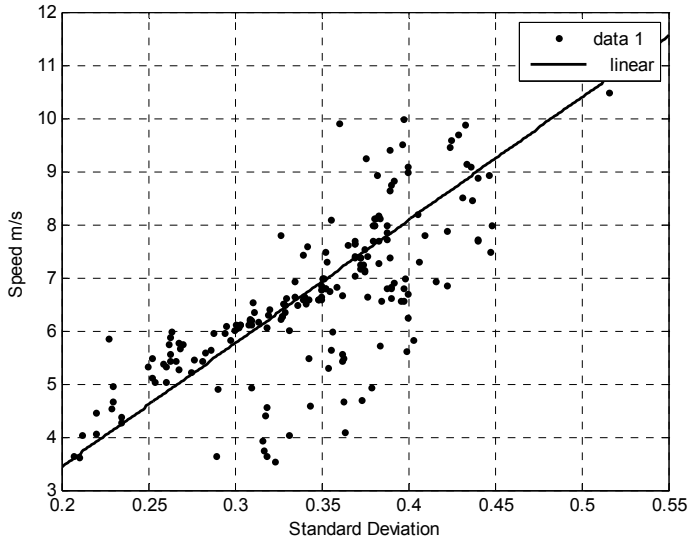

Figure 13. Testing of 150 samples Standard deviation Vs speed of vehicle

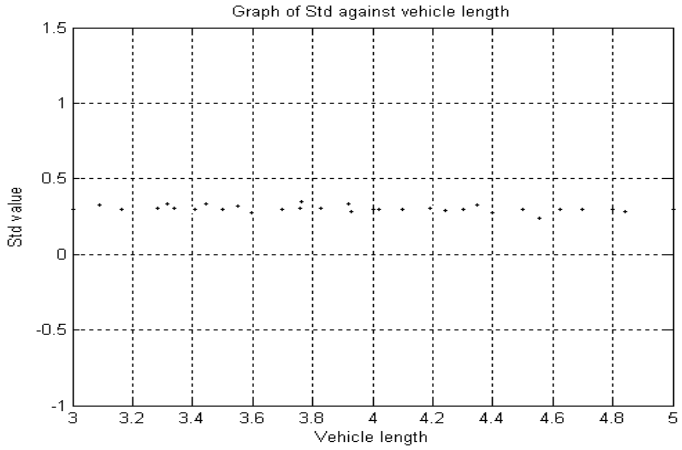

Figure 14. Vehicle length Vs Standard deviation

Modern Applied Science

www.ccsenet.org/journal.html

Vol. 3, No. 3

March 2009

Experimental Research of Optimal Die-forging Technological Schemes Based on Orthogonal Plan

Jianhao Tan (Corresponding author)
Electrical and Information Engineering College
Hunan University
Changsha 410082, China
E-mail: tanjianhao96@sina.com.cn

Jing Zhang
Electrical and Information Engineering College
Hunan University
Changsha 410082, China

Fu Guo
Electrical and Information Engineering College
Hunan University
Changsha 410082, China

The research is financed by National Natural Science Foundation (Approval No. 60634020) and Hunan Province Natural Science Foundation (Approval No. 08JJ3132)

Abstract

Some problems on setting up die-forging technological scheme design criteria by means of traditional methods are analyzed. The idea of mining die-forging technological schemes based on orthogonal plan is pointed out. The height and width of the hub are selected as key factors from many ones which influence the die-forging technological schemes of axisymmetric forging, then, in connection with the two factors, the relative experiments are arranged by using the two-factor-twice-composition orthogonal plan. Flash metal consumption is choosed from a lot of factors as object function whose values are measured in the experiments. When the height and width of the hub are the constant, from several experimental schemes, the technological scheme which makes flash metal consumption be the least is selected as the optimal scheme, so the design criteria of optimal die-forging technological schemes are got. Because of adopting orthogonal plan in arranging the experiments, the design and manufacturing period of forging is reduced, the developing cost of forging is cut down, and the raw and processed material consumption is decreased. In laying down the design criteria of optimal die-forging technological schemes, optimal technology is combined with artificial intelligence. In determining the relations among so many factors in die-forging technological schemes, expert's experiences are used, and experimental results are dealt with by means of association rule mining technology, which makes the decision of die-forging schemes more reasonable and practical.

Keywords: Orthogonal plan, Factor, Optimal die-forging technological scheme, Design criterion, Association rule mining

The die-forging of axisymmetric forging is a complicated deformation process. Therefore, it is difficult to analyze and estimate it. So up to now, there have not yet been common design criteria of die-forging technological schemes. With the development of CAD technology, quantitative die-forging design criteria become increasingly urgent. Many scholars use such ways as theoretical analysis, experimental research or their combination (Xiao Jingrong, Li dequn Translation, 1983) to achieve this goal. As for theoretical methods, because of the complexity of die-forging production, either the analytic method, the main stress one, deformation work one, slip-line one, or discrete finite-cell one can only solve very simple forging problems and has a certain distance from guiding practical design. That is because, first, these

methods make a lot of assumptions which have been quite different from actual production conditions; Second, it is difficult to determine border conditions which are not enough precise. In experimental methods, no matter which of the coordinate grid method,the inspect plasticity one and light plasticity one is used , it could be hard to achieve common design criteria. This has forced people to explore more effective ways to draw die-forging design criteria. In order to improve processes, enhance forging production capability, and enhance the utility of CAD systems, we analyzed some factory's forging die-forging technology of axisymmetric forging. On the basis of first-hand materials, we have decided to mine the design criteria of die-forging technological schemes of axisymmetric forging and to plan these experiments using the orthogonal design method. Thus, more effective data can be received with less experimental number and the corresponding design criteria of technological schemes of die-forging will have greater reliability. The aims of these experiments are to review flash metal consumption produced at every experiment and the quality of shaped forging, and thus determine the design criteria of optimal die-forging technological schemes of axisymmetric forging.

The strategy of orthogonal plan method is to make coefficient matrix become diagonal one after choosing appropriate factors, determining their variational ranges and making certain coding. Thus, the calculation of adverse matrix is simplified and the relativity of regression coefficients is eliminated. It is more important to obtain the desired sample number and factor values.

1. Orthogonal Plan of Experiments

1.1 Basis of Orthogonal Plan

The on-vehicle die-forging process of axisymmetric forging has the following characteristics: axisymmetric forging has a series of feature variables to best reflect its own characteristics(etc. shape complex coefficients, the height-to-width ratio of hub, and so on) most of which are always stable within a certain scope (for example, shape complex coefficients and the height-to-width ratio of hub are always between 1~5), and corresponding to these feature variables, a optimal technological scheme may be found, that is, on-vehicle die-forging has a optimal range. The range divisions to these feature variables with orthogonal plan may fully cover the information of these feature variables using less test points.

1.2 Strategy of Orthogonal Plan

The paper arranges experiments using twice composition orthogonal design. These experiments arranged in composition design have a series of advantages. Firstly, its test points are greatly less than the ones of three-level full-factor experiments, but maintain sufficient residual free degree; Secondly, they are received on the basis of one-time regression and if one-time regression is indistinct, asterisk points and central ones may be supplemented.

In the paper, two basic factors which are the height B and the width of hub are selected according to two-factor-twice-composition. In the case of two factors B and H, the number N of these experiments arranged in composition orthogonal design is 9. After standardized processing, a test point distributed list is received as shown in Table.1.

1.3 Choices of the Factors Affecting Die-forging Technological Schemes

1) Basis of the Choices of Factors

One of the aims to rationally determine die-forging technological schemes is to obtain high-quality forging. And to receive high-quality forging, metal must be filled with mould cavity. The factors affecting meta l moulding are multifaceted. On the shapes and sizes of axisymmetric forging (here mainly referring to the gear type), shape complex coefficients and the height-to-width ratio are two main factors affecting full moulding of metal. The two factors have both independence and the interaction. The paper uses the variety of the height and width of hub to affect the one of the two factors and the height and width of hub greatly affect shape complex coefficients. So the choices of die-forging technological schemes of axisymmetric may be seen as depending mainly on the two factors, the height and width of hub.

Some of the existing criteria determining die-forging technological schemes are mostly confined to a particular factor (i.e. the height-to-width ratio) as a basis in order to select technological schemes. In this paper, the two factors are inspected at the same time in determining the impact of the die-forging technological schemes. These are two mutually independent factors and in determining die-forging technological schemes, the height-to-width of hub is preferentially considered: When the height-to-width of hub is relatively large, even though shape complex coefficients are relatively small, it is advisable that once or twice pre-forging should be introduced. This is the difference between the design criteria and other ones.

2) Choices and Valuing of Factors

(1) Choices of Factors

As described above, the paper uses two steps to select factors: first selecting middle factors as shape complex coefficients of cold forging and the height-to-width ratio of hub and then selecting basic factors as the height and width

of hub.

(2) Valuing of Factors

The valuing of factors and the determination of ranges must reflect the characteristics of forging produced in some factory. Specifically, the shape complex coefficients and the height-to-width ratio are all selected between 1and 5.The fluctuating range of basic factors is determined by means of the following ways: first adding up the production data of some factory in order to receive the fluctuating range of factors in actual production process; then proportionately reducing statistical data in order to gain experimental data according to the principle "when experimental results are applied to reality, geometric similarity, physics one and external environment one must be met. " statistics will be to the experimental data. Experimental data should ensure that the shape complex coefficients and the height-to-width ratio of experimental forging are roughly equal to the ones of actual forging. According to the analysis of the site production data, statistical data of H and B are received as shown in table.2.

After proportionately reducing statistical data of B and H and properly adjusting them, experimental data of B and H are received as shown in table.3.

According to the experimental data of B and H and the discussion about experimental composition, Experimentalplan list is gained as shown in table.4.

2. Determination of Optimal Die-forging Technological Schemes

2.1 Experimental Design and Processing Ways of Experimental Results

1) Experimental Design

Owing to short time, this paper could not complete the tests for nine types of forging. Only five typical types of forging are selected for the tests. Such feature parameters as shape complex coefficients, the height-to-width ratio of hub, and so on are displayed in Table.5.

Seen from Table.5, The shape complex coefficients and the height-to-width ratio of hub of the five types of forging cover a large range. Despite the relatively little number of experiments, the results of the experiment are still lost general.

Three Experiments are made for each type of forging, and the die-forging technological schemes of three experiments are free-upsetting—finish-forging, free-upsetting—pre-forging—finish-forging, and free-upsetting—pre-moulding-pre-forging—finish-forging respectively.

2) Processing Ways of Experimental Results

The aim of the experiments is to determine the magnitude of flash metal consumption produced at each experiment and thus develops the design criteria of optimal die-forging technological schemes.

In actual production, in judging the good or the bad of some technological scheme, except the quality of forging, such factors as flash metal consumption, die life, the complexity of die structure, operating convenience, and so on are also taken into consideration. Namely, The technological schemes which can achieve the best techno-economic benefit are the optimal ones.

On the conditions of the experiments, such factors as flash metal consumption, die life, the complexity of die structure, operating convenience, and so on are hard to be inspected. Therefore, in judging the good or the bad of some technological scheme only the factors, the quality of forging and flash metal consumption are considered. For each technological scheme, the design of its process step has to ensure metal fully moulded. Therefore, in this paper, optimal technological schemes of forging are determined by means of using the magnitude of flash metal consumption as object function and at the same time inspecting forging cost.

The design principles of the optimal technological schemes decided in the sense of less flash metal consumption and lower forging cost are: when the scheme, free-upsetting—finish-forging, is compared with the one, free-upsetting—pre-forging—finish-forging, or the scheme, free-upsetting—pre-forging—finish-forging, with the one, free-upsetting—pre-moulding-pre-forging—finish-forging, the former is preferentially considered. At the time, it is not much meaningful to reduce material consumption and the former is helpful for reducing die-forging process steps, simplifying die structure, increasing productivity, thereby reducing forging costs; Otherwise, the schemes which make flash metal consumption less are considered in order to make object function the least.

2.2 Experimental Results and Analysis of Material Consumption

After summing up and coordinating test data of 15 experiments at 5 test points, the experimental results of material consumption are received as shown in Table.6.

Seen from Table.6,for tested Piece F1, The flash metal consumption of Experiment F12 is the least, its optimal technological scheme is free-upsetting—pre-moulding--pre-forging—finish-forging; for tested Piece F2, The flash

metal consumption of Experiment F22 is the least, its optimal technological scheme is free-upsetting—pre-moulding--pre-forging—finish-forging; for tested Piece F3, F4, and F5, their flash metal consumption of respective three tests is almost the same, but introducing pre-forging is helpful for prolonging die life and decreasing waste rate, their optimal technological scheme is selected as free-upsetting—pre-forging—finish-forging .

Based on the above analysis, the optimal technological schemes of five test points are shown in Table.7.

3. Conclusions

According to Table. 7 and 5, The corresponding relations between the optimal technological schemes of axisymmetric forging, and the shape complex coefficients of forging and the height-to-width ratio of hub B/H can be found, thereby the design criteria of the optimal die-forging technological schemes of axisymmetric forging can be gained as shown in Figure.2.

From Figure.2, the following conclusions can be shown:

(1) The optimal die-forging technological schemes of axisymmetric forging can be determined by means of the shape complex coefficients and the height-to-width ratio of hub;

(2) With the increase in the shape complex coefficients and the height-to-width ratio of hub , introducing pre-forging is helpful for reducing the flash consumption, prolonging die life and decreasing waste rate.

Due to the following reasons, The design criteria have to be consummated and modified before being applied to actual production. These reasons include: there are the greater differences between the experimental environment (including materials, deformation temperature, deformation rate and semifinished materials processing methods) and the actual situations of productions; Because of limited time, the orthogonal design only determines the two sizes, the height and width of hub, and shape complex coefficients are adjusted by modifying the height-to-width ratio of hub. Therefore, there are the large interaction and poor independence between shape complex coefficients and the height-to-width ratio of hub. Clearly, the design criteria of optimal die-forging technological schemes received in the paper is not enough accurate. Further research shows that the independence between the two factors can be modified through adjusting external sizes of hub and thereby, the more acute and actual design criteria of optimal die-forging technological schemes may be set up; Little test points make the design criteria not enough perfect.

References

Buntine W L. (1994). Operations for Learning with Graphical Models. *Journal of Artifical Intelligence Research* , 1994, 2:159-225.

Chu W W, Chen Q. (1992). Neighborhood and Associative Query Answering. *Journal of Intelligence Information Systems*, 1992, 1:355-382.

Rakesh Agrawal, Ramakrishnan Srikant. (1994). *Fast Algorithms for Mining Association Rules in Large Database*. Proceedings of the Twentieth International Conference on Very Large Databases, Santiago, Chile, 1994.

Stone M. (1974). Cross-validatory Choice and Assessment of Statistical and Predications. *Journal of the Royal Statistical Society*, 1974, 36:111-147.

Stone. (1984). *Classification and Regression Trees*. Wadsworth International Group, 1984.

Wang Mingci, Sheng Hengfan. (1999). *Probability Theory and Mathematical Statistics*. Beijing:Higher Education Press, 1999.

Wang R, Storey V, Firth C. (1995). *A Framework for Analysis of Data Quality Research*. IEEE Transactions on Knowledge and Data Engineering, 1995, 7:623-640.

Xiao Jingrong, Li dequn Translation. (1983). *Optimum and Automation Principles for the Technological Processing of Heat Volume Die-forging*. Beijing:National Defence Industry Press, 1983.

Zhang Shuyou, Ji Yangjian, Tan Jianrong, Peng Qunsheng. (2001). Self-adaptive Processing of Non-correlative Size Mark Interfence. *Journal of Zhejiang University*, 2001, 35(6):45-48.

Table 1. Test Point Distributed List

Experimental No.	Factor Valuing	Explanation
1	(1 1)	Full-factor tests of (+1 –1) are composed of four test points: $m = 2^2 = 4$
2	(1 -1)	
3	(-1 1)	
4	(-1 –1)	
5	(γ 0)	The four test points are distributed in asterisk positions of Axes B and H: $2p = 4$
6	(-γ 0)	
7	(0 γ)	
8	(0 –γ)	
9	(0 0)	The central test point is composed of The zero-level of B and H: $m_0 = 1$

Table 2. Statistical data of H and B

Factors	Fluctuating Range	
	Max	*Min*
H	24.00	10.00
B	29.50	10.65

Table 3. Test data of H and B

Factors	Fluctuating Range	
	Max	Min
H	17.00	13.00
B	24.00	18.00

Table 4. Experimentalplan list

Experimental No.	Factors	
	H	*B*
1	17.00	24.00
2	17.00	18.00
3	13.00	24.00
4	13.00	18.00
5	17.00	21.00
6	13.00	21.00
7	15.00	24.00
8	15.00	18.00
9	15.00	21.00

Table 5. Feature Parameters of Experimential Samples

Numbers of Test Pieces	Feature Parameters			
	H	B	S	H/B
F_1	17.00	24.00	3.56	4.25
F_2	17.00	18.00	3.21	3.09
F_3	13.00	18.00	2.89	2.49
F_4	17.00	21.00	2.65	2.14
F_5	15.00	18.00	2.43	1.86

Where $F_i(i=1,..,5)$ is the number of tested forging according to the large-to-small order of shape complex coefficients.

Table 6. Material Consumption List

Experimental No.	Material Consumption		
	Total Weight	Weight of Forging	Weight of Flash
F_{11}	484.0	443.4	40.6
F_{12}	461.4	440.0	21.4
F_{13}	522.2	478.4	43.8
F_{21}	507.7	468.7	39.0
F_{22}	505.0	481.4	23.6
F_{23}	514.6	489.0	37.6
F_{31}	515.0	496.9	38.3
F_{32}	509.1	473.0	36.1
F_{33}	527.9	485.4	42.5
F_{41}	526.4	490.2	36.2
F_{42}	517.1	481.5	35.6
F_{43}	523.6	499.0	28.6
F_{51}	531.8	500.9	30.9
F_{52}	465.1	463.8	21.3
F_{53}	521.8	495.3	26.5

Where $F_{ij} * i = 1,\ldots 5, j = 1,\ldots 3)$ is the experimental number, I is the number of tested pieces, and j is the experimental order of some tested piece. The corresponding technological schemes are:

(1) free-upsetting—finish-forging;

(2) free-upsetting—pre-moulding-pre-forging—finish-forging;

(3) free-upsetting—pre-forging—finish-forging.

Table 7. Optimal Technological Scheme List

Tested Piece No.	Optimal Die-forging Technological Schemes
F_1	free-upsetting—pre-moulding-pre-forging—finish-forging
F_2	free-upsetting—pre-moulding-pre-forging—finish-forging
F_3	free-upsetting—pre-forging—finish-forging
F_4	free-upsetting—pre-forging—finish-forging
F_5	free-upsetting—pre-forging—finish-forging

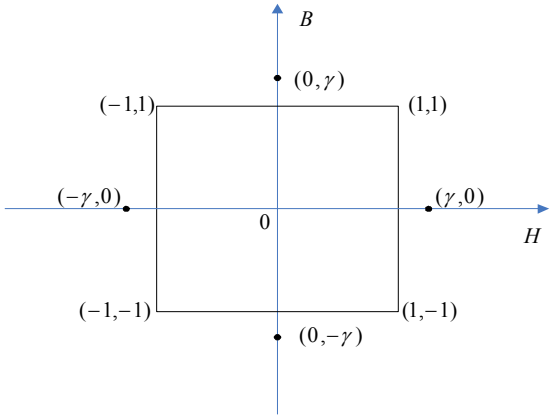

Figure 1. Experimentalconstruct for two-factor-twice-composition orthogonal plan

Where $\gamma = 1$, as shown in Figure 1.

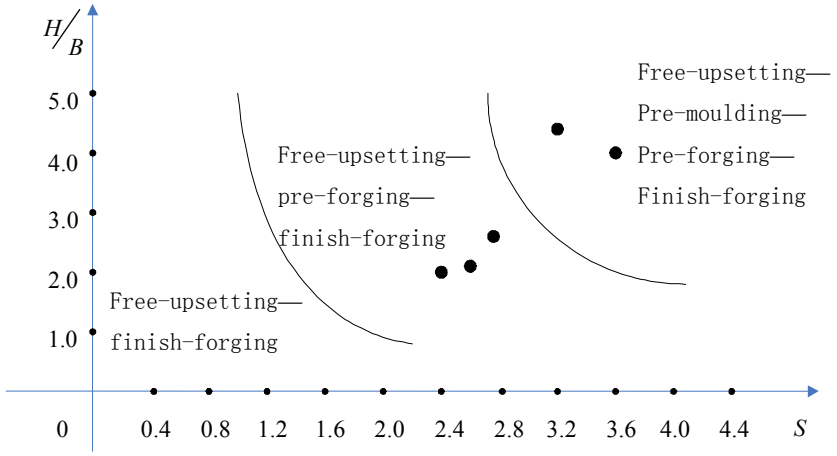

Figure 2. Design Criteria for the Optimal Die-forging Technological Schemes of Axisymmetric Forging

Modern Applied Science

www.ccsenet.org/journal.html

Vol. 3, No. 3

March 2009

Thermal Degradation of Chemically Treated *Shorea Parvifolia* Plywood

Zaihan Jalaludin
Forest Research Institute Malaysia (FRIM)
52109 Kepong, Selangor, Malaysia

Hashim W.Samsi
Forest Research Institute Malaysia (FRIM)
52109 Kepong, Selangor, Malaysia

Razak Wahab
Universiti Malaysia Sabah (UMS)
88999 Kota Kinabalu, Sabah, Malaysia

Aminuddin Mohamad
Universiti Malaysia Sabah (UMS)
88999 Kota Kinabalu, Sabah, Malaysia

Puad Elham
Forest Research Institute Malaysia (FRIM)
52109 Kepong, Selangor, Malaysia

Shaharuddin Hashim
Forest Research Institute Malaysia (FRIM)
52109 Kepong, Selangor, Malaysia

Abstract

Thermal degradation of chemically treated plywood of *Shorea parvifolia* as the facing material in timber stud partition was investigated. The plywoods were treated with Dricon, Monoammonium Phosphate, Diammonium Phosphate and mixture of Borax and Boric Acid at 20% concentration. The cavity of the partition was filled with fibre insulating material. The fire resistance of the partitions was evaluated using 1.5 m by 1.5 m gas-fired furnace following the standard temperature-time curve set by the British Standard, BS 476 : Part 22:1987. The rating measures the integrity-ability to withstand collapse or sustained flaming and the insulation-ability to prevent excessive increase of temperature. In this study the best fire resistance rating time based on integrity failure was the partition using *Shorea parvifolia* plywood treated with Dricon (118 min.) followed by Diammonium Phosphate (116 min.), Monoammonium Phosphate (109 min.) and Borax and Boric Acid (97 min.) respectively. The untreated *Shorea parvifolia* plywood partition shows the weakest fire resistance rating of 95 min.

Keywords: Chemically treated plywood, *Shorea parvifolia*, Timber stud partition, Fire Resistance Test, Integrity Tests

Introduction

Plywood, chipboard, block-board, cement-board and wood-wool slab are widely used as the non-structural components in the building industry (Rashid, 1987; Lebow & Winandy, 1999; Winandy, 2001; Green 2004). These materials are commonly used as wall partition, flooring system and ceilings. Being combustible in nature, they do not comply with the fire safety requirements. Plywood include the most common and popular among wood composite performs more or less identical to solid wood, i.e it carbonizes at the rate of 0.6 mm per minute and has a spread of flame rating of class 3 (Rashid, 1986). Sometimes wood is treated with chemicals to extend its utility into new markets. Fire retardant treated

plywood is sometimes permitted as an alternative to noncombustible materials in structure that require increased fire safety (Winandy, 2001).

Surface treatment of wood with intumescent or other flame retardant finish can also be employed (Levan, 1984; Levan & Winandy, 1990). The incorporation of fire retardants chemicals such as mono-ammonium phosphate, boric acid and borax enhanced the fire retardants properties of chipboard (Rashid, 1982 & 1987). The strengths of the fire retardant treated plywood were found to decrease slightly compare to those of the untreated plywood (Wang, 1999)

In Malaysia the used fire rated building components of non-combustible material in multi-storey residential and commercial building is common since the introduction of the building regulation, the Uniform Building By Laws (UBBL) (Anonymous, 1984). At the moment the most common materials used in the fabrications of light weight partition system in multi-storey and modern high-rise building are steel and gypsum plasterboard. Wood farmed walls lined with wood-based material are not very popular except when used as separating walls in the two to three storey timber chalets. Beings combustible, timber and wood-based panel product are not used widely in the building industry unless they comply with the requirement specified in the UBBL. The clause on the non-combustibility criteria in the UBBL for some building component has limited the use of timber and wood-based panel product.

In this study "the effects of chemicals on treated *Shorea parvifolia* plywood as timber stud partition were investigated in relation to the flame properties". The chemicals chosen have the fire retardants ability (Rashid, 1986 & 182; Green 2004).

Material & Method

Treatment of plywood

Shorea parvifolia plywood of 18mm thickness were treated with chemicals of Monoammonium phosphate (MAP), Diammonium phosphate (DAP), Dricon and Borax:Boric Acid (BBA) respectively at 20% concentration. Treatments were conducted in a commercial vacuum impregnation chamber using full cell process with an initial vacuum of 1 bar for 30 min. followed by 14 bar of pressure for 2 hours and a final vacuum of 1 bar for 10 min. Treated samples were weighed before and after treatments to determine the chemical loading by weight difference. After treatment, the samples were labelled with stickers and stored outdoors under cover for fifthteen days to allow for chemical fixation to proceed. The chemical loading of each of the veneer were calculated based on differential in weight before and after treatments.

Timber stud partition system preparation

A timber stud partition system was constructed within a brick wall bonded together by cement and mortar. The overall size of the *Shorea parvifolia* plywood partition was 900 mm high by 810 mm wide by 106 mm thick built within a masonry brick wall inclusive of a 40 mm wide vertical gap along one edge to provide no lateral restraint to the specimen. Each *Shorea parvifolia* plywood panel was fixed on both sides to a vertical hardwood timber stud. The cavity of the partition was filled with 40mm thick Rockwool known as Fibertex with density of 100 kg m^{-3}. The size of the plywood was 900mm x 270 mm x 18 mm. Three samples of *Shorea parvifolia* plywood panels were fixed vertically to the masonry brickwall. The *Shorea parvifolia* plywoods were predrilled and fixed to the frame with nominal nails at 300 mm centre to centre. Figure 1 shows the detailed drawings of the *Shorea parvifolia* plywood partition system.

Fire Resistance Test

The fire resistance test was conducted in accordance with the procedure specified in BS 476: Part 22:1987. The ambient air temp., as measured by the ambient temperature specified as in standard, in the general vicinity of the test construction shall be within 5°C to 35°C immediately prior to the heating period. The complete partition sample has been installed to the frame of 120 mm thick cement wall within R.S.J. steel frame. The partition was exposed to fire following the temp.-time relationship specified in British Standard in the following manner. The steel frame containing the construction was mounted to form the vertical face of a gas-fired furnace provided with three probe thermocouples and controlled to conform the following temperature-time relationship:

$$T = 345 \log (8t+1) + T_0 \quad \text{----------} \quad (1)$$

Where,

T = furnace temp. at time, t

t = time of test (min.)

T_0 = ambient temperature

Throughout the heating process, the pressure within the furnace and over the upper two-thirds of the specimen was maintained slightly positive in relation to the pressure within the laboratory. The pressure conditions were controlled to be within the range of 8 to 12 Pa at the point located at the top edge of the test specimen. The mean temperature of the unexposed face of the partition was measured using five thermocouples in which one had to be fixed at the centre of

each of the quarters of the wall with thermocouples (type K) in which one had to be fixed approximately at the centre of each of the four quarters of the partition. Throughout the test, observations were made on the general behavior of the specimen on the exposed and unexposed faces. The partition system was judged on their ability to comply integrity and insulation criteria.

Insulation

In the insulation criteria, failure were recorded:

a. When the unexposed face temperature increases by more than 140 ^{0}C above its initial value;

b. When the temperature recorded at any position on the unexposed face, either by a fixed thermocouple or by the roving thermocouple were in excess of 180ºC above the initial mean unexposed face temp.

Integrity

In general, a failure of the test construction to maintain integrity occurred when the tested object collapses or sustained flaming occured for more than 10 seconds on the unexposed face. Under criteria for impermeability, failure is deemed to have occurred when one or either of the following conditions prevail:

a. Where the cotton pad test is performed, flames and/or hot gases cause flaming of the cotton pad.

b. Where the use of cotton pad is not suitable, failure shall be deemed to have occurred when either:

- the 6 mm diameter gap gauge can penetrate a through gap such that the end of the gauge projects into the furnace and the gauge can be moved in the gap for a distance of at least 150 mm ; or
- the 25 mm diameter gap gauge can penetrate a through gap such that the end of the gauge projects into the furnace.

Results & Discussions

Actual Furnace Temperature according to Standard Temp. Time Curve

Table1 shows the overall percentage deviation of each different sample following their time interval specified as in the BS standard. Supposedly, as in the standard, stated that any deviation calculated shall be within the specified percentage tolerance as in the table above. The percentage deviation is within the specified percentage tolerance for all tests. For the first 10 min. the percentage deviation for control, MAP, DAP, BBA and Dricon are -1.7%, 2.0%, 4.8%, 2.27% and11.9% respectively. Although Dricon has the highest percentage it still is within the tolerance. Between 10 to 30 min. the percentage deviation for control, MAP, DAP, BBA and Dricon are -1.5%, 0.5%, 0.7%, -0.07% and 1.5% respectively. It shows that the actual furnace start to burn accordingly. Between 30 to 120 min. the percentage deviation for control, MAP, DAP, BBA and Dricon are 0.03%, - 0.03%, - 0.2%, - 0.04% and - 4.1% respectively.

Unexposed Face Temperature of the Partition System

The temp. rise recorded on the unexposed face of the samples as determined by the surface thermocouples is shown in Table 2. Fire retardants treated plywood performed much better than the untreated samples. The recorded temperature shows MAP treated samples having the lowest mean temperature followed by BBA, Dricon, DAP and untreated samples respectively. In BS standard the failure point is above 180°C while for the mean temperature is above 140°C and all the plywood stills below the failure point.

Observation in failure of integrity during testing

Observations on the general behaviour of the test specimen taken during the test at the failure of integrity are tabulated in Table 3. The best fire resistance rating time was the partition using *Shorea parvifolia* plywood treated with commercial fire retardant chemical namely Dricon (118 min.) followed by DAP (116 min.), MAP (109 min.) and BBA (97 min.) respectively based on their integrity failure.

Conclusions & Recommendations

The best fire resistance rating time based on integrity failure obtained from the studies conducted was the partition using *Shorea parvifolia* plywood treated with commercial fire retardant chemical namely Dricon (118 min.) followed by DAP (116 min.), MAP (109 min.), BBA (98 min.) and control (95 min.) respectively. Based on the observation and in the sense of integrity, all the four partition samples that were made from treated plywood have failed before they can reach the final 120 min.. Dricon has showed the longest period which is only 2 min. away from the standard. On the other hand, untreated plywood showed the shortest period which was failed in the 95 min. In the insulation criteria, the treated *Shorea parvifolia* plywood performed slightly below the optimum or failure temperature and the insulation rating.

Further study needs to be undertaken in improving the tests design, increasing the effectiveness of the chemical treatment and uptakes, and the material used.

References

Anonymous. (1984). Malaysian Uniform Building By Laws 1984.

Green, J. (2004). An overview of the fire retardant chemicals industry, past, present, future. *Journal of Fire and Materials*. Vol. 19, Issue 5, 2004. Pp 197-204.

Lebow, S.T. and Winandy, J. E. (1999). Effect Of Fire Retardant Treatment On Plywood pH And The Relationship Of To Strength Propeties. *Wood Science and Technology.* 33 (1999) 285-298.

Levan, S.,L. and Winandy, J. E. (1990). Effect of fire retardant treatment on wood strength. *A review: Wood and Fiber Sciences*, 22 (1), 113-131

Levan, S.L. (1984). *Chemistry of fire retardancy*. P.p.531-574 in Rowell, R (ed.) The chemistry of solid wood. American Chemical Society Pub. Washington, D.C.614pp

Rashid, A.M. (1986). Fire Retardency And Fungal Decay Of Malaysians Timbers Treated With Phosphorus And Borax Compounds. M.Sc. Thesis, University Of London.

Rashid. A.M. (1982). Early Burning Properties of Malaysian Timber By Inclined Panel Test. *The Malaysian Timbers By Inclined Panel Test*. The Malaysian Forester. 45 (3).

Rashid. A.M. (1987). *Fire Retardant Study On Commercial Chipboard*-part 1 Fire Propagation performance. FRIM occasional paper. Forest Research Institute of Malaysia. Kepong.

Wang, S. Y. and Yu-Chen, R. (1999). Structure Performance of Fire-Retardant Treated Plywood:

Table 1. The percentage deviation of each sample following time interval

Time (min.)	Specified Percentage Tolerance (+ or -)	Percentage Deviation (%)				
		Dricon	BBA	DAP	MAP	Control
0-10	15	11.9	2.27	4.8	2.0	-1.7
10-30	10	1.5	-0.07	0.7	0.5	-1.5
30-120	5	-4.1	-0.04	-0.2	-0.03	0.03

Table 2. Unexposed face temp. of the partition system

Plywood Treatment	Mean temp. (°C)	Maximum temp. (°C)	Remarks
Untreated (Control)	122	154	Temp. at 95 min shows no failure in insulation
DAP	116	166	Temp. at 115 min shows no failure in insulation
MAP	76	92	Temp. at 100 min shows no failure in insulation
BBA	80	99	Temp. at 95 min shows no failure in insulation
Dricon	98	178	Temp. at 110 min shows no failure in insulation

Table 3. Observations noted on the samples that fail the integrity tests

Treatment	Failure in Integrity Tests (min.)	Observations
Untreated (Control)	95	At 86 min plywood panel at the bottom side started to char. The charring area starts to create a gap and at 95 min a flame flashing through the plywood panel for more than ten second.
DAP	116	At 110 min plywood panel at the bottom side started to char. At 118 min a flame flashing through the surface for more than ten second.
MAP	109	At 105 min surface of plywood started to char. It builds a gap within the plywood and at 109 min a flaming flashing through the surface for more than ten second.
BBA	98	At 96 min surface of plywood started to char. The charred area increased. At 98 min a flaming flashing through the surface more than ten second.
Dricon	118	At 110 min surface of plywood started to char. It builds a gap within the plywood and at 118 min a flaming flashing through the surface for more than ten second.

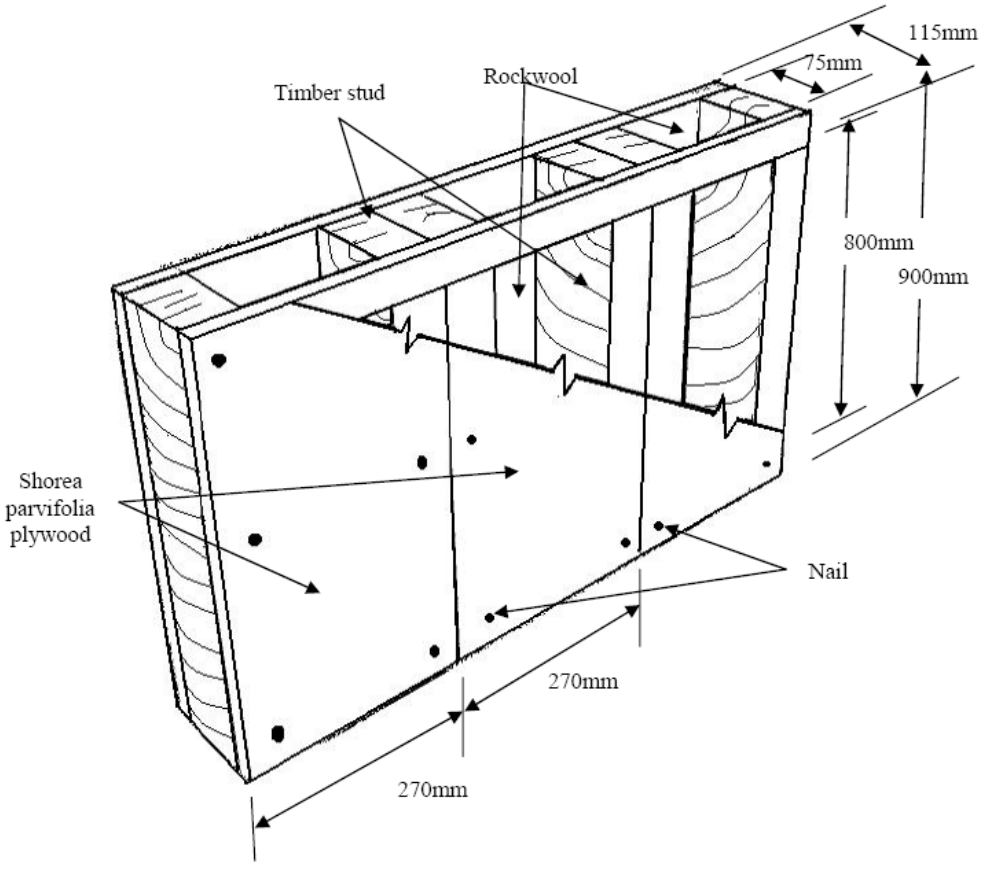

Figure 1. Isometric drawing view of the wall assembly

Modern Applied Science

www.ccsenet.org/journal.html

Vol. 3, No. 3

March 2009

A Simple Analysis Method of Products Lifetime Distribution

Yueming Wang

Fiber Optic Sensing Technology Research Center

Wuhan University of Technology

Wuhan 430070, China

Abstract

The basis of reliability analysis is determining products lifetime distribution type, which is also a tedious job. In accordance with the failure of parametric estimation using probability papers and hypothetical examination, products lifetime distribution type is studied with linear regression analysis and Office Excel.

Keywords: Cumulative distribution function, Reliability, Linear regression analysis, Correlation coefficient, Office Excel

The lifetime distribution type of a product is determined for analyzing reliability of it.Parametric estimation using probability papers and linear hypothesis examination are two commonly methods (*ZHU Min-bo,WANG Shi-ping.Study and Application on Analysis Method Using Probability Papers under Reliability Test[J].COMPUTER AND PERIPHERALS,1997,21(6),66.*), but both of them have deficiencies. The former is intuitive, but difficult for manual drawing, more artificially imposed factor analysis of low level precision.The test data of some products is approximately close to a linear line on the various kinds of probability papers,and it is difficult to determine its most suitable distribution type.The latter is usually supposing some distribution type suitable for the product lifetime and then making correlation examination.If correlation coefficient is greater than the minimum value,the hypothesis about lifetime distribution type is tenable .But this method may miss more reasonable distribution type.

The linear regression analysis method is accurate calculation that is widely used in various fields,and also can be used to determine the distribution types of products lifetime.

1. linear regression correlation coefficient calculation with Excel

Basic thoughts of linear regression analysis is to analyze a non-linear problem by turning it into a linear problem and to make linear correlation coefficient **R** as examination,**R** is defined as (*CHEN Min-xiang.Lifetime Distribution Analysis and Reliability Estimation of Electric Motors[J].ELECTRIC MACHINES AND CONTROL,1998,2(2),89.*):

$$R=\frac{\sum_{i=1}^{n}(t_i-\bar{t})(Z_i-\overline{Z})}{\sqrt{\sum_{i=1}^{n}(t_i-\bar{t})^2\sum_{i=1}^{n}(Z_i-\overline{Z})^2}} \tag{1}$$

In above formula, (t_i, Z_i) is test data,$\bar{t}$, $\overline{Z}$ are the the average values,namely:

$$\bar{t}=\frac{1}{n}\sum_{i=1}^{n}t_i$$

$$\overline{Z}=\frac{1}{n}\sum_{i=1}^{n}Z_i \qquad (i=1,2,3,\ldots n)$$

From formula (1), it is tedious to calculate **R** value, but the Office Excel tool will make it simple.If scattered points sketch is drawn with Excel,it is much more simple, it is simple to get R^2 and **R** value directly.

2. Product lifetime distribution type analysis method

In reliability analysis,product lifetime distribution type usually include an exponential distribution,normal distribution,lognormal distribution and the Weibull distribution.These cumulative distribution functions are all nonlinear and very complex,they can be transformed into linear equations through variable transformation, Scattered points sketch about products test data for (t_i, $F(t_i)$) can be drawn directly with Excel and **R** value can be given directly with Excel.By comparing these **R** values,the distribution type correspondence with the maximum value of **R** is the most

reasonable lifetime distribution function for the product.

3. Linearization of cumulative distribution function and determination of products lifetime distribution type

To estimate the distribution type and characteristic parameters of all products through the experimental results for large samples,histogram with frequency usually used.But in engineering practice,There are usually small samples.It is inaccurate to estimate the result of small samples with estimation method for a large samples.To estimate the probability of small samples,methods of calculating the cumulative distribution probability are usually used,namely,mid-rank being calculated as follows:

$$F(t_i) = \frac{i}{n+1} \tag{2}$$

In above formula, ***n*** is the total number of samples under test, t_i is the sequence number of failure samples, which arranges from short lifetime to long lifetime.

Now motor accelerated lifetime data shown in table 1(*CHEN Min-xiang.Lifetime Distribution Analysis and Reliability Estimation of Electric Motors[J].ELECTRIC MACHINES AND CONTROL,1998,2(2),89*) is studied as an example, $F(t_i)$ in the table 1 can be given immediately with Excel according to formula (2).

3.1 Linearization of an exponential distribution function

Cumulative distribution function of two-parameter exponential distribution is as follows:

$$F(t) = 1 - e^{-\frac{t-\gamma}{\theta}} \qquad (t \geq \gamma) \tag{3}$$

The above formula is arranged in order and changed in natural logarithm,it can become a standard linear equation:

$$Z_e(t) = at + b \tag{4}$$

In above equation,

$$Z_e(t) = \ln \frac{1}{1-F(t)} \tag{5}$$

$$a = \frac{1}{\theta}$$

$$b = -\frac{\gamma}{\theta}$$

$Z_e(t)$ can be given immediately with Excel according to formula (5), shown in table 2.

According to table 2,take ***t*** as x-axis and $Z_e(t)$ as y-axis,scattered points sketch about products test data is drawn with Excel,and then,selecting Linear Type in Adding the Trend Line, clicking on Showing Formula button and Showing Square Of R button in the function of Select,pressing Enter,linear tread chart can be drawn automatically,its linear formula and the value of R^2 can be given immediately,as shown in Figure 1, the linear equations of exponential distribution function is as bellow:

$$y = 8 \times 10^{-7} x - 1.4674 \tag{6}$$

$$R^2 = 0.9506 \tag{7}$$

From equation (6), $a = 8 \times 10^{-7}$, $b = -1.4674$,From equation (4)and(5), the parameters of θ and γ can be given.

From equation (7), the correlation coefficient **R** is given,namely: $R = 0.9750$.

3.2 Linearization of normal distribution functions

The cumulative distribution function of normal distribution is as follows:

$$F(t) = \int_0^t \frac{1}{\sqrt{2\pi}\sigma} e^{-\frac{1}{2}(\frac{t-\mu}{\sigma})^2} dx = \Phi(\frac{t-\mu}{\sigma}) = \Phi(Z_N) \tag{8}$$

In it,

$$Z_N = \frac{1}{\sigma} t - \frac{\mu}{\sigma} \tag{9}$$

Taking the inverse of the standard normal cumulative distribution,selecting NORMSINV(n/(N+1)) in some spreadsheets,transforming $F(t_i)$ (or $\Phi(Z_N)$) into $Z_N(i)$,listed in table 3.

According to the same method as subclauses 3.1, Figure of Linearization and correlation coefficient of normal distribution functions can be drawn with Excel.

3.3 Linearization of lognormal distribution function

The accumulative distribution function of lognormal distribution(*ZHANG Zhi-hua.Statistical Analysis of Accelerated Life Test on Lognormal Distribution Case Under Type I Censoring[J].ACTA MATHEMATICAE APPLICATAE SINICA,2000,23(4),489.*) is as follows:

$$F(t)=\int_0^t \frac{1}{\sqrt{2\pi}\sigma x} e^{-\frac{1}{2}\left(\frac{\ln x-\mu}{\sigma}\right)^2} dx = \Phi\left(\frac{\ln t-\mu}{\sigma}\right) = \Phi(z_{LN}) \tag{10}$$

In it,

$$Z_{LN}(t') = \frac{1}{\sigma}t' - \frac{\mu}{\sigma} \tag{11}$$

$$t' = \ln t \tag{12}$$

According to the same method as subclauses 3.2,select NORMSINV(n/(N+1)),transform $\Phi(z_{LN})$ (or $F(t_i)$) into $Z_{LN}(i)$, $Z_{LN}(i)$ can be given as the method in table 3,and according to the equation(12),change t into t',,listed in table 4 with Excel.

According to the same method as subclauses 3.1, Figure of Linearization and correlation coefficient of lognormal distribution function can be drawn with Excel.

3.4 Linearization of Weibull distribution function

The cumulative distribution function of three-parameter Weibull distribution(*TONG Xiao-jun,MA QUN.General Regression Analysis Method for Estmating The Weibull Three Parameters[J].JOURNAL OF TANGSHAN INSTITUTE OF TECHNOLOGY,1995,17(2),78.*) is as follows:

$$F(t) = 1 - e^{-\left(\frac{t-\gamma}{\eta}\right)^m} \tag{13}$$

In it, γ, η and m are the location parameter, the scale parameter and the shape parameter (or Weibull slope) of Weibull distribution, respectively.

The equation (13)is arranged in order and taken natural logarithm, it is:

$$Z_w(t) = at' + b \tag{14}$$

In it,

$Z_w(t) = \ln\ln\frac{1}{1-F(t)}$

$a = m$

$t' = \ln(t-\gamma)$

$b = -m\ln\eta$

From equation (14), if (t_i, $F(t_i)$) obey Weibull distribution, relationship between $Z_w(t_i)$ and t_i' should be linear,but its linear correlation relates to the location parameter γ. According to the drawing principle of Weibull probability paper, γ value correspondence with maximum R value is the most reasonable location parameter estimation of Weibull distribution.

Due to the complex R value calculation, trial calculation by equation (1) is very simple and accurate with Excel.The method of trial calculation(*FANG Zhi-qiang,GAO Lian-hua.Estimation of Parameters of Three-parameter Weibull Distribution in Life Analysis[J].Journal of Armored Force Engineering Institute,1999,13(1),72.*) in Excel spreadsheets:Suppose a minimum lifetime t_1 was location parameter γ,Then,a start from $\gamma_2 = 0.95\gamma_1$, step down from $\Delta = 0.05\gamma_1$,The respective corresponding correlation coefficient R is calculated,the location parameter correspondence with the maximum R value is γ. In this example, $\gamma = 1.73\times10^6$.

According to equation (14), $Z_w(t_i)$ can be calculated directly with Excel, shown in table 5.

According to the above method in subclauses 3.1,Figure 2 is drawn with Excel.

From figure 1 to figure 4, each of the four distribution functions can be fit a linear relationship sketch,and among them the linear correlation coefficient R value correspondence with Weibull distribution function is the maximum.It indicates that Weibull distribution is the most appropriate function to describe products lifetime in this example.

4. Conclusion

Based on the linear regression analysis,products lifetime distribution function is linearized,fitting-straight line,its equation and its correlation coefficient R value are given quickly and easily by using Excel auxiliary drawing method.Through comparing the R values,the distribution function correspondence with the maximum of R values describes the most reasonably lifetime distribution,which is a simple method to determine the distribution type of product lifetime. According to the fit linear equations, correlative parameters can also accurately calculated.

References

Chen, Minxiang. Lifetime Distribution Analysis and Reliability Estimation of Electric Motors[J]. *ELECTRIC MACHINES AND CONTROL*, 1998, 2(2), 88-95. (in Chinese)

Fang, Zhiqiang, Gao, Lianhua. Estimation of Parameters of Three-parameter Weibull Distribution in Life Analysis[J]. *Journal of Armored Force Engineering Institute*, 1999, 13(1), 72-74. (in Chinese)

Tong, Xiaojun, Ma, Qun. General Regression Analysis Method for Estmating The Weibull Three Parameters[J]. *JOURNAL OF TANGSHAN INSTITUTE OF TECHNOLOGY*, 1995, 17(2),78. (in Chinese)

Zhang, Zhihua.Statistical Analysis of Accelerated Life Test on Lognormal Distribution Case Under Type I Censoring[J]. *ACTA MATHEMATICAE APPLICATAE SINICA*, 2000, 23(4), 489. (in Chinese)

Zhu, Minbo,Wang, Shiping. Study and Application on Analysis Method Using Probability Papers under Reliability Test[J]. *COMPUTER AND PERIPHERALS*, 1997, 21(6), 66-67. (in Chinese)

Table 1. motor accelerated lifetime test data, (t_i is reversal times)

i	***t_i/h***	***F(t_i)***	***i***	***t_i/h***	***F(t_i)***
1	1.82E+06	0.0714	8	2.76E+06	0.5714
2	1.95E+06	0.1429	9	2.92E+06	0.6429
3	2.20E+06	0.2143	10	3.55E+06	0.7143
4	2.18E+06	0.2857	11	3.90E+06	0.7857
5	2.25E+06	0.3571	12	4.20E+06	0.8571
6	2.27E+06	0.4286	13	4.44E+06	0.9286
7	2.43E+06	0.5000			

Table 2. corresponding relation between $Z_e(t)$ and t

i	***t_i/h***	$z_e(t)$	***i***	***t_i/h***	$z_e(t)$
1	1.82E+06	0.0741	8	2.76E+06	0.8473
2	1.95E+06	0.1542	9	2.92E+06	1.0296
3	2.20E+06	0.2412	10	3.55E+06	1.2528
4	2.18E+06	0.3365	11	3.90E+06	1.5404
5	2.25E+06	0.4418	12	4.20E+06	1.9459
6	2.27E+06	0.5596	13	4.44E+06	2.6391
7	2.43E+06	0.6931			

Table 3. corresponding relationship between $Z_N(t)$ and t

i	***t_i/h***	$z_N(t)$	***i***	***t_i/h***	$z_N(t)$
1	1.82E+06	-1.4657	8	2.76E+06	0.1800
2	1.95E+06	-1.0676	9	2.92E+06	0.3600
3	2.20E+06	-0.7917	10	3.55E+06	0.5659
4	2.18E+06	-0.5659	11	3.90E+06	0.7917
5	2.25E+06	-0.3660	12	4.20E+06	1.0676
6	2.27E+06	-0.1800	13	4.44E+06	1.4657
7	2.43E+06	0.0000			

Table 4. corresponding relationship between $Z_{\mathrm{LN}}(t')$ and t'

i	***t_i'/h***	$z_{LN}(t_i')$	***i***	***t_i'/h***	$z_{LN}(t_i')$
1	14.415	-1.4657	8	14.831	0.1800
2	14.481	-1.0676	9	14.888	0.3600
3	14.606	-0.7917	10	15.082	0.5659
4	14.596	-0.5659	11	15.177	0.7917
5	14.626	-0.3660	12	15.249	1.0676
6	14.634	-0.1800	13	15.306	1.4657
7	14.702	0.0000			

Table 5. corresponding relation between $Z_w(t_i)$ and t_i'

i	***t_i'/h***	$Z_w(t_i)$	***i***	***t_i'/h***	$Z_w(t_i)$
1	11.3144	-2.6022	8	13.8373	-0.1657
2	12.2307	-1.8698	9	13.9836	0.0292
3	13.0476	-1.4223	10	14.4083	0.2254
4	13.0013	-1.0892	11	14.5861	0.4321
5	13.1402	-0.8168	12	14.7136	0.6657
6	13.1768	-0.5805	13	14.8084	0.9704
7	13.4386	-0.3665			

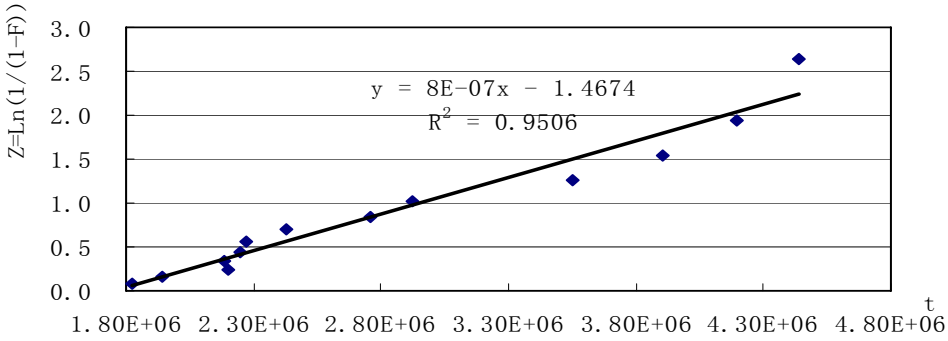

Figure 1. Linear and correlation coefficient of exponential distribution function

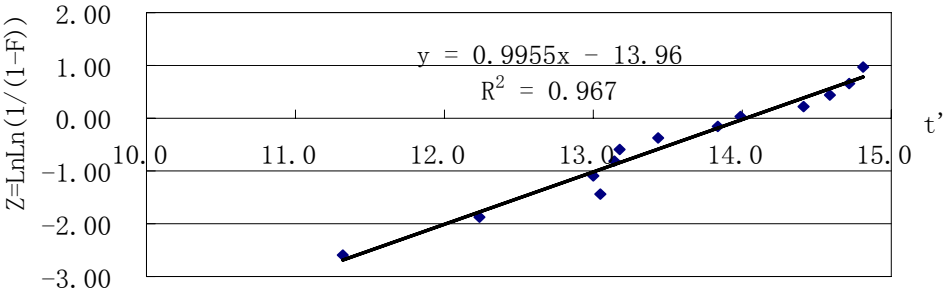

Figure 2. Linearization and correlation coefficient of Weibull distribution function

Modern Applied Science

www.ccsenet.org/journal.html

Vol. 3, No. 3

March 2009

Cold Extrusion of Carbon Electrodes Using Dies of CRHS

Concept and Performance Analysis

Sami Abulnoun Ajeel

University of Technology, Bagdad, Iraq

E-mail: sami-tech@yahoo.com

Ahmed M. Saleem

Technical College, Mosul, Iraq

E-mail: ah_ms1971@yahoo.com

Farhad B. Bahaideen

School of Mechanical Engineering

Universiti Sains Malaysia

14300 Nibong Tebal, Penang, Malaysia

E-mail: farhadbilal62@yahoo.com

M. Abdul Mujeebu (Corresponding author)

School of Mechanical Engineering

Universiti Sains Malaysia

14300 Nibong Tebal, Penang, Malaysia

Tel: 60-1-4305-1476 E-mail: mamujeeb5@yahoo.com

Hussain J. Mhamed Alalkawi

University of Technology, Bagdad, Iraq

E-mail: alalkawi2007@yahoo.com

Abstract

In this article cold extrusion of carbon electrodes using the direct extrusion die that is designed using one of the theoretical concepts, Constancy of the Ratio of the Successive Generalized Homogeneous Strain-increment (CRHS), is presented. On the basis of the above concept we used three types of dies that are categorized as uniform (UCRHS), accelerated (ACRHS), and decelerated (DCRH) according to the deformation rates. All dies were with fixed reduction area of 50%. The mixture used (filler with binder) was extruded in round section carbon electrodes carried out at 60^{o}C to 80^{o}C. Ten samples are produced and tested for properties such as electrical resistivity, hardness, density and porosity. The results show that the extrusion die UCRHS is the more efficient die design for the production of carbon electrodes.

Keywords: Extrusion die, Carbon electrodes, CRHS, Binder ratio, Porosity

1. Introduction

Extrusion is used to produce the large electrodes for electric furnaces, small rods for dry cell batteries, finer grained graphite for molds used by the metallurgical industry, electrolytic anodes, and the bulk material from which certain motor and generator brushes are made. Traditionally, the extrusion processes can be divided into three types: forward extrusion, backward extrusion, and combined forward/backward extrusion. The extrusion processes can also be categorized by the operation temperature into hot, warm, and cold extrusion. Metal extrusion is a near-net-shape manufacturing process that can reduce the machining tasks. This process can be used to produce long and straight extrusion product such as gear spline, bar, wire, and seamless pipe. The die electrode is used to produce the extrusion die cavity [(Kao (2000)].

Regarding the axisymmetric extrusion, the Constancy of the Ratio of the Successive Generalized Homogeneous Strain-increment (CRHS) and the constancy of the Mean Strain Rate (CMSR) had been proposed and used by Vaidyanathan and Blazynski (1973) and Blazynski and Lee (1984) in obtaining the extrusion die profile. Some other

generalised die profiles, such as conic functions by Chen and Ling (1968) and streamline by Yang et al. (1986) were also used in creating uniform extrusion flow and obtaining smaller extrusion load.

As far as the authors are aware, use of CRHS dies for extrusion of carbon electrodes has not been published so far. Against this background, the current study focused on the application of CRHS dies for the cold extrusion of carbon electrodes. Three typical designs namely, 1) Decelerated Constancy of the Ratio of the successive generalized Homogeneous Strain-increment (DCRHS), 2) Accelerated Constancy of the Ratio of the successive generalized Homogeneous Strain-increment (ACRHS) and 3)Uniform Constancy of the Ratio of the successive generalized Homogeneous Strain-increment(UCRHS) have been used and tested for their efficiency. It has been found that UCRHS die design is the best for the application.

2. The CRHS Concept

CRHS is the abbreviation of 'Constancy of the Ratio of the Successive Generalized Homogeneous Strain-increment'. This concept of tool design is based upon the basis of homogeneous strain for the metal forming operation, which represents a function of the physical dimensions of the engineering material to be formed. The die surface profile or tool profile can be produced by using this concept, because the forming pass is divided into, number of sections (n) depending on the expression of CRHS through these sections as follows

$$\frac{\varepsilon_{H_2}-\varepsilon_{H_1}}{\varepsilon_{H_1}-\varepsilon_{H_0}} = \frac{\varepsilon_{H_3}-\varepsilon_{H_2}}{\varepsilon_{H_2}-\varepsilon_{H_1}} = \cdots\cdots\cdots = \frac{\varepsilon_{H_n}-\varepsilon_{H_{n-1}}}{\varepsilon_{H_{n-1}}-\varepsilon_{H_{n-2}}} = Constant = S \qquad (1)$$

Where ε_{Hn} is the value of homogeneous strain at the section 'n' through the forming pass. But S is a constant called 'Rate of Deformation', it does not depend on the time because it is related to the deformation rate and has no relation to the strain rate. The value of S can be taken randomly, if it has a value S<1, it means that the rate of deformation is 'Decelerated', and it has a sign of DCRHS. S=1, the rate of deformation is 'Uniform', and it has a sign of UCRHS. S>1, the rate of deformation is 'Accelerated', and it has a sign of ACRHS, as shown in Figure 1.

The constant S may take different values, but the experience in the metal forming tool design indicates that the range in between (0.8 –1.2) is sufficient for most applications. In this study, the value S = 0.9 is considered as a decelerated rate of deformation, and the value S = 1.2 for the accelerated rate [Kena (2007)].

3. The Extrusion Machine

Extrusion press illustrated in figure 2 consists of a jacketed cylindrical chamber known as the mud chamber which is filled with the mix. A separate molding operation known as preslugging is done by means of the vertical ram (Tamping ram) and the horizontal one known as extrusion ram forces the warm mix from the mud chamber through a reducer into a die of the desired shape. Another design of extrusion machine is the tilting type in which the mud chamber may be raised to vertical position to facilitate loading, and then lowered to a horizontal position in extrusion. Chamber adapter and dies are jacketed and are generally heated with steam or hot oil, or electricity.

A typical extrusion temperature for large electrodes is about 100 ^{o}C and extrusion pressure may range from 2.6 – 55 MPa. (400 – 8000 Psi), depending on the ratio of die area to mud chamber area, temperature and type of mix. Extrusion rate may be about 10 mm/s (24 in/min) at 16.8 MPa (2500 Psi) [Kirk and Othemer (1964&1978), Hibbler (1997)].

4. Extrusion Die

Figure 3 shows the extrusion die designed according to German specification (DIN). The basic parts of the die are as follows:

4.1 Container

It is a cylinder machined in the turning machine from steel (34 CrNiMo6) with inside diameter, 100 mm.

4.2 The Punch

The punch is machined from steel (X210Cr12/6) to have a good toughness against the force applied. It is turned and heated treated to 40 HRC and surface ground to ensure alignment with the container.

4.3 The base

The base of the press has a hole in the middle of it to have a good fitting between the die and the base.

4.4 Dies

1) Accelerated Constancy of the Ratio of the successive generalized Homogeneous Strain-increment (ACRHS), S= 1.2

2) Uniform Constancy of the Ratio of the successive generalized Homogeneous Strain-increment (UCRHS), S = 1 and

3) Decelerated Constancy of the Ratio of the successive generalized Homogeneous Strain-increment (DCRHS), S= 0.9

The material that was used in making the dies is X 155Cr V Mo 12 1/G which has a good hardness besides its ability to be heat treated up to 42 HRC. The reduction in all dies was 75%. Figure 4 shows a photograph of the dies, the container and the punch.

5. Extrusion Process

Extrusion process was done on die by using hydraulic press, type IVA LOLA RIBER with capacity of 40 tons at the University of Technology, Bagdad, Iraq. The die was kept at the base of the press in such a way that the outer surface of the die outlet fit into the inner side of base hole of the press. A light oil lubricant was used to lubricate the inside wall of the die and the container. Cold extrusion process was done at 80^0C by putting a heating element around the die. The slugging force was 2 MPa and the extrusion force was 3 MPa. Extrusion samples of 50 mm diameter and 150 mm long have been produced whose details are given in table 1. A hollow cylinder was putted under the base of the press to let the samples flow outside. Turning was done for some samples for using them in the tests, the forces used were the highest, and sufficient forces for the dies that were used in extrusion process, except the die (DCRHS) with deformation ratio of (S = 0.9) which needed high force (more than 7 MPa). This force indicates that the die was less efficient than the other dies. The products made by dies of type ACRHS and DCRHS show outside cracks and poor service finish, hence the electrodes made by them were rejected. Many experiments have been done by using the die UCRHS with the same filler mixture for different binder ratios (27%, 29%, 31%, 32%, 33%, and 34%) and for different binder temperatures (60^0C, 70^0C, 80^0C, 90^0C, 100^0C, and 120^0C) . Also, experiment was done to measure the time and velocity for electrode extrusion of 150 mm with different binder ratios.

6. Testing of Carbon Electrode Samples

Carbon electrodes tests include the following:

6.1 Electrical Resistively Test

The Electrical resistively of the samples were measured by using high sensitivity digital Avo meter. The temperature coefficient of resistance was calculated by taking measurements under different temperatures using a furnace (type HP) with a maximum temperature 500 ^{o}C. The temperatures were measured using thermo couples (type K) attached to the sample. A graph between current and voltage was plotted, and specific sensitivity Pc and the electric resistance R were calculated as follows,

$$P_c = R\frac{A}{L} \tag{1}$$

where,

L is the length of the samples, A, cross section area of the contact

Temperature coefficient of resistance can be calculated as:

$$R_T = \frac{R_t}{1+\alpha_T(t-T)} \tag{2}$$

where,

R_T, electric resistance at room temperature, R_t, electric resistance at the known temperature,

and α_T, temperature coefficient of resistance which is obtained from,

$$\alpha_T = \frac{R_t - R_T}{R_T(t-T)} \tag{3}$$

6.2 Hardness test

In this test Brenell hardness tester model (Wilson B554T) was used. The applied load was 0.6 kg and the diameter of the ball indenter was 2.5 mm. Then, the LIETZ optical microscope was used to measure the diameter of the indent. The H.B. was calculated using equation [Mohamed Ali (2002)],

$$BHN = \frac{2P}{\pi D^2(1-\sqrt{(1-d^2/D^2)})} \tag{4}$$

where:

P, load in kg, D, diameter of the ball in mm, and d, diameter of the impression in mm.

6.3 Density and Porosity Measurements

In this measurement the typical way (20 – 83) ASTM was used. The upper and the lower surfaces were ground by a samfering paper. First the dry sample is weighed in air then dropped in boiled water, and kept at the same temperature for six hours then the sample and the water are left to cool. The sample is then weighed in water and out of water after the two surfaces are slightly cleaned with a piece of cotton. Then it is baked for twelve hours in a furnace, and is weighted again after baking.

The density of the sample can be calculated by

$$\rho = \frac{D}{V} \tag{5}$$

Where,

D, the weight after backing, V , volume of sample obtained from,

$$V = (W - S)\rho' \tag{6}$$

where, W, weight out of water after cleaning, S, weight in water and ρ' density of water equal to 1 g/cm^3.

The volume of open pores V^I and the volume of prevision portions V^{II} in cm^3 can be calculated as follows

$$V' = (W - D)\rho' \tag{7}$$

$$V'' = (D - S)\rho' \tag{8}$$

Apparent porosity P is calculated from,

$$P = \frac{(W - D)}{V}\rho' * 100\% \tag{9}$$

Water absorption A is obtained from the equation,

$$A = \frac{(W - D)}{D} * 100\% \tag{10}$$

And apparent specific gravity T can be calculated from equation,

$$T = \frac{D}{D - S} \tag{11}$$

7. Results and Discussion

Carbon electrode extrusion is one of forming operations which occurs at a degree less than recrystallization temperature and leads to have strain hardening in the material. Its degree depends on the value of strain which depends on the redundant ratio and causes to improve the mechanical properties. This result is well-suited with that of previous work (Mohamed Ali S., 2002). The dies with UCRHS have a less strain redundancy factor among all the dies and have the shortest length for different extrusion temperatures.

7.1 Density, porosity, and water absorption

The results of density, porosity, and water absorption test are shown in table 2. A comparison with the product of S.G.L. Group Company is shown in figure 5 .The curve shows the result of this research which is compatible with the result of the company.

7.2 Hardness

The result of hardness test is shown in table 3. This result is compatible with that of published work [Farook (1999)]. Figure 6 shows the relationship between the density and the hardness of the samples.

7.3 Effect of Extrusion on Hardness

The sample showed high compression stress as the porosity already present in the material has been minimized by compressing the material before extrusion, which leads to increase in hardness and tensile resistance. This result is well-matched with that of published work [Salam (1996)].

7.4 Electrical Resistivity

The electrical resistively is shown in table 4. The results are is good agreement with other workers [Kirk and Othemer (1964&1978)]. Figure 7 shows the relationship between the density and the resistivity of the samples.

7.5 Effect of Binder Temperature on Extrusion Process

There is a limit for binder temperature through which extrusion process can be done. This limit is found to be 60 ^{o}C to 80^{o}C for the surface of the mixture near the internal surface of the container and the die, and 90 ^{o}C to100^{o}C for the outer surface of the container and the die. It has been experienced that the temperature of the mixture near the container surface should be more than that of the remaining part of the mixture by 20^{o}C to simplify the forming process, and get a good fluidity of the mixture in and out the die.

7.6 Effect of Binder Ratio on Extrusion Process

The extrusion velocity increases by increase of binder ratio by non linear relationship which can be expressed by the function $T = AB^{-\alpha}$. For the coke and binder used, the minimum binder ratio is found to be 31% for extrusion process. For a ratio 27% – 30%, the extrusion process is too hard and the miture has no plasticity to form carbon electrode. Fig. 8 shows the variation of time versis binder ratio. It is clear that the binder ratio decrease with increase the time and sharply variation at the time (145 - 10) sec.

7.7 Effect of Friction on Extrusion Process

The extrusion product at the first time had a crack at the surface because of the surface resistance of the die and the container. This problem was solved by the following actions

1) The surface grinding of both die and container.

2) The careful use of lubricant.

3) Increase in extrusion force.

Surface grinding for both small scale die and container is very important because of high friction. The use of lubricant for 2 cm^3/kg of the mixture was very necessary.

8. Conclusion

The cold extrusion process of carbon electrode forming by using CRHS die designing concept is being presented. Three typical die designs such as accelerated (ACRHS), uniform (UCRHS) and decelerated (DCRHS) were used for the process and the samples in each case were tested for their quality. From the result analysis, the following conclusions are drawn

1) The best temperature of the mixing (the filler and the binder) is 100 ^{o}C – 120^{o}C.

2) The best temperature of the extrusion is 100 ^{o}C for outside wall of the container and 80 ^{o}C – 90^{o}C for inside wall of the container.

3) The best die is UCRHS.

4) The force needed for preslugging the mixture is 2 MPa.

5) The force needed for extruding the electrode is 3 MPa.

6) The electrode can be produced successfully by direct cold extrusion.

References

Blazynski, T.Z and Lee, R.S. (1984). *Pass design and redundant strain in forward tube extrusion*, J. Mech. Work. Technol. **9**, p.313.

Chen, C.T. and Ling, F.F.L. (1968). *Upper bound solution to axisymmetric extrusion problems*, Int. J. Mech. Sci. 10 (11) 863–879.

Farook, M. A. (1999). The effect of engineering die shape on the direct extrusion mechanics and properties of Al, alloy 1060, PhD thesis, University of Technology , Iraq, Baghdad.

Hibbler, R.C. (1997). *Mechanics of materials*, 3rd edition, pp. 112 – 114.

Kao, Y.-C. (2003). Development of a remote quick CAE system on sculptured metal extrusion die surface, *Journal of Materials Processing Technology*, 140(1-3), 116-122.

Kena, M.H.S. (2007). Analysis and Application of Subdivision Surfaces, M.Sc Thesis, Department of Production and Metallurgy Engineering, University of Technology, Bagdad, Iraq.

Kirk R.F. and Othemer D.F. (1964). *Encyclopedia of chemical technology*, Wily and Sons.

Kirk R.F. and Othemer D.F. (1978). Encyclopedia of chemical technology,Tohnwilegend sons, Inc.

Mohamed Ali S. (2002). The effect of engineering shape of extrusion die on the fatique strength of Al-alloy, MSc thesis university of technology Iraq, Baghdad.

Salam, H. A. A. (1996). Manufacturing of the graphite electrodes and studies of some physical properties, M.Sc. Thesis, University of Technology, Baghdad, Iraq.

Vaidyanathan, P. V. and Blazynski, T. Z. (1973). A theoretical method of efficient extrusion die design, J. Inst. Met. 101, p.7

Yang, D.Y., Han, C.H. and Lee, B.C. (1986). The use of generalized extrusion boundaries for the analysis of axisymmetric extrusion through curved dies, Int. J. Mech. Sci. 27 (10), 653–663.

Table 1. Samples taken for electrodes

Symbol	Filler Type	Binder Ratio%	Type of Die
E1	Needle	31	UCRHS
E2	Needle	31	UCRHS
E3	Needle	31	UCRHS
E4	Needle	31	UCRHS
E5	Needle	31	UCRHS
E6	Needle	31	UCRHS
E7	Needle	31	UCRHS
E8	Needle	31	UCRHS
E9	Needle	31	UCRHS
E10	Needle	31	UCRHS

Table 2. Density, porosity, and water absorption for needle petroleum coke and binder samples

Sample no.	Density g/cm^3	Water absorption%	Porosity %
E1	1.63	11.52	25.38
E2	1.65	11.5	24.5
E3	1.69	10.8	22
E4	1.71	10.2	21.8
E5	1.70	10.3	21.9

Table 3. Hardness and density for needle petroleum coke and binder samples

Sample no.	Hardness	Density
E6	318	1.62
E7	319	1.66
E8	320	1.69
E9	322	1.70
E10	325	1.72

Table 4. Electrical resistively for needle petroleum coke and binder samples

Sample no.	Resistively Ohm - cm	Density g/cm^3
E6	0.291	1.62
E7	0.290	1.66
E8	0.275	1.69
E9	0.285	1.7
E10	0.270	1.72

Figure Legends

1. Figure 1. The compounds die (CRHS) surface profile along the die inlet-exit.
2. Figure 2. Extrusion machine for carbon electrode manufacture.
3. Figure 3. Schematic assembly drawing for extrusion die.
4. Figure 4. The dies, the container and the punch.
5. Figure 5. A comparison between the research result and SGL group company product.
6. Figure 6. Relationship between the density and hardness.
7. Figure 7. Relationship between density and the resistively
8. Figure 8. Variation of binder ratio with extrusion time for electrodes 50 mm diameter at constant pressure and temperature.

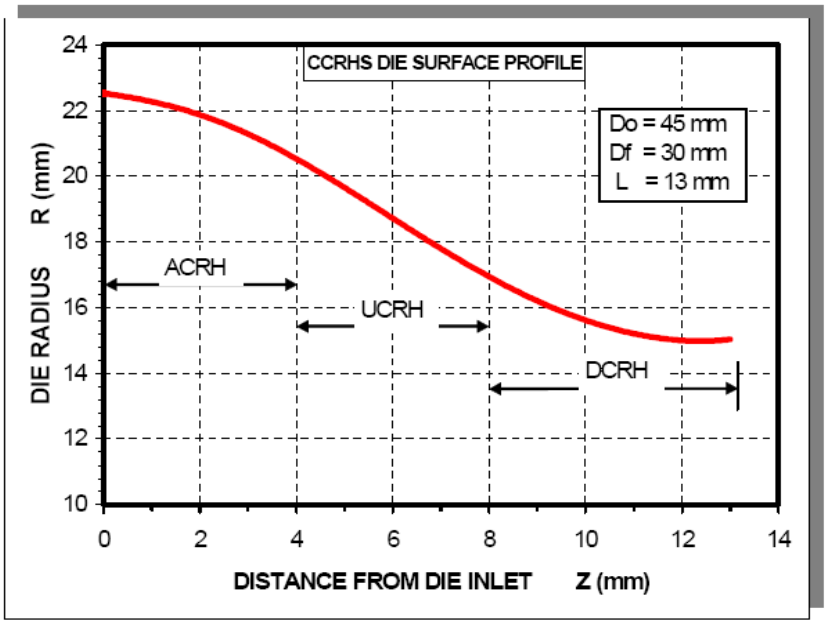

Figure 1.

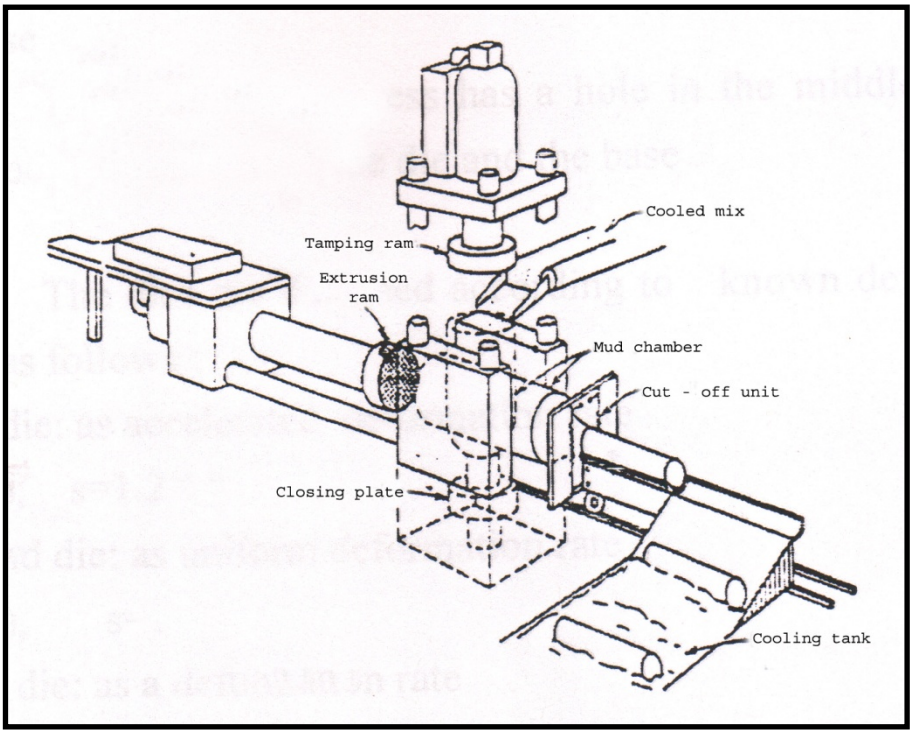

Figure 2.

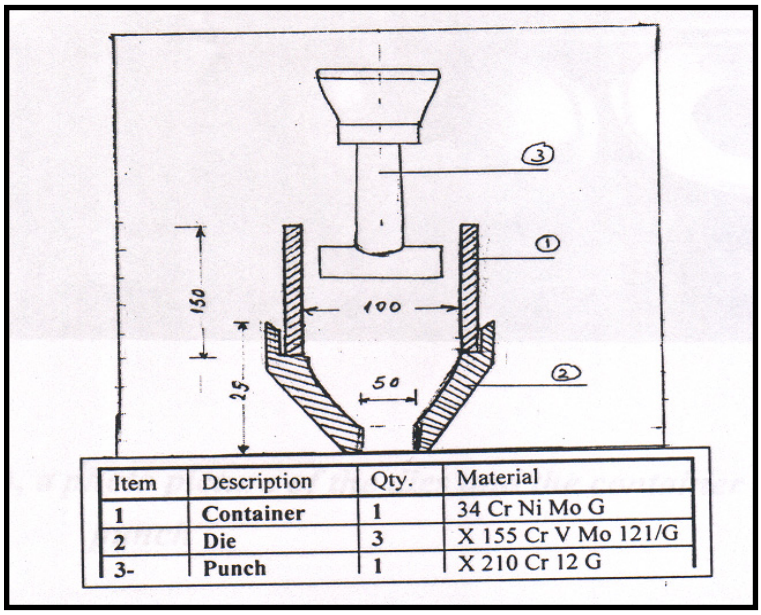

Item	Description	Qty.	Material
1	Container	1	34 Cr Ni Mo G
2	Die	3	X 155 Cr V Mo 121/G
3-	Punch	1	X 210 Cr 12 G

Figure 3.

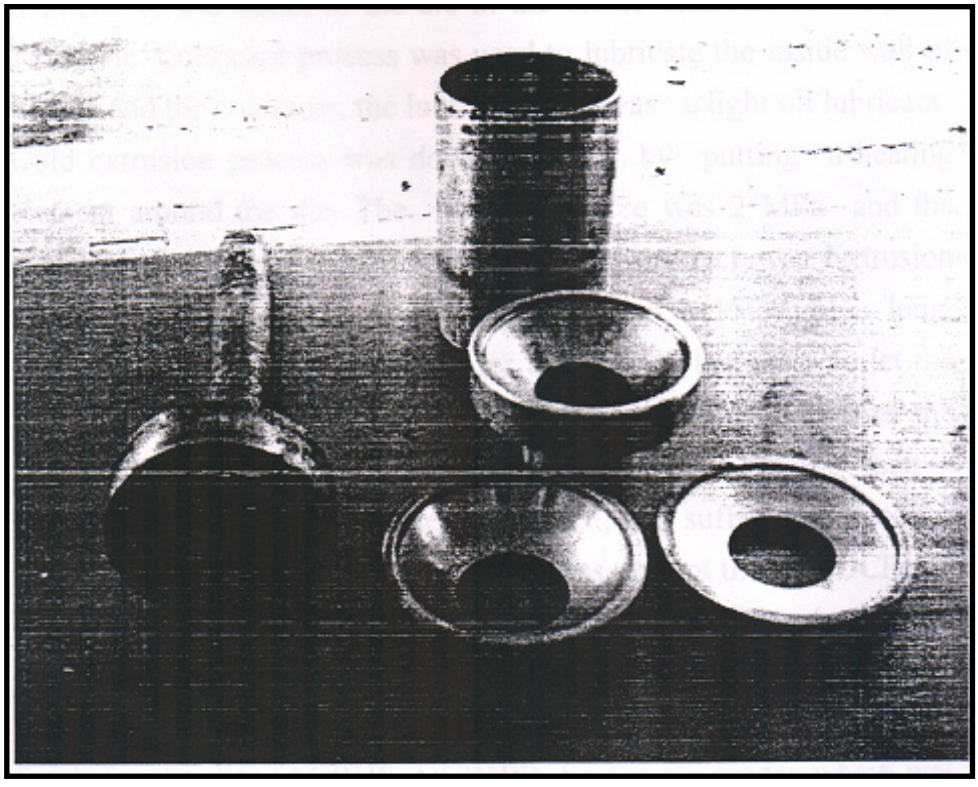

Figure 4.

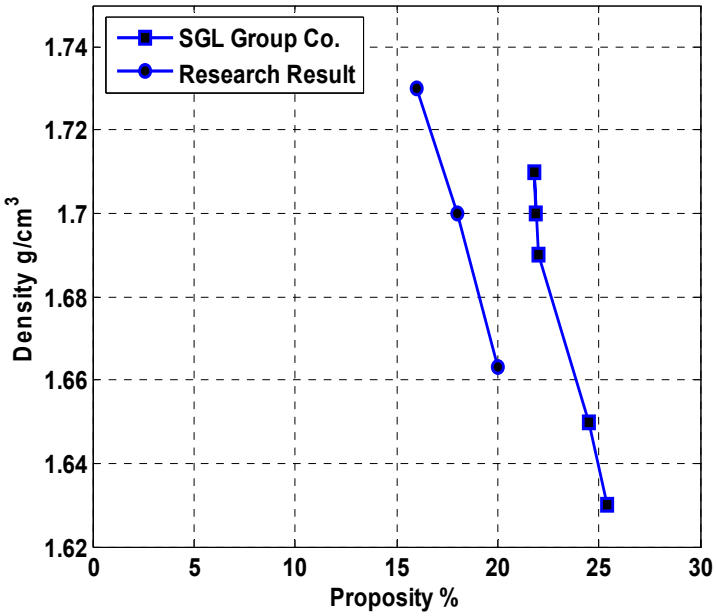

Figure 5.

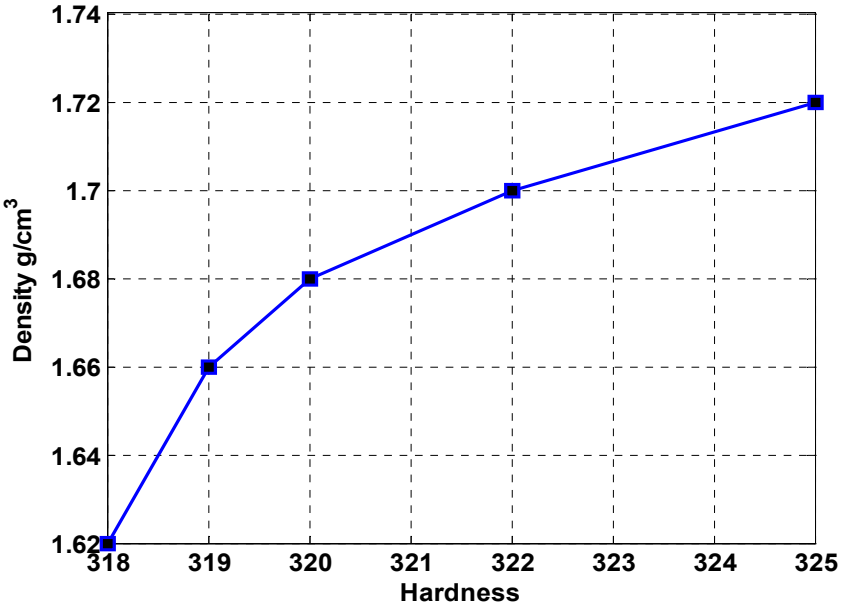

Figure 6.

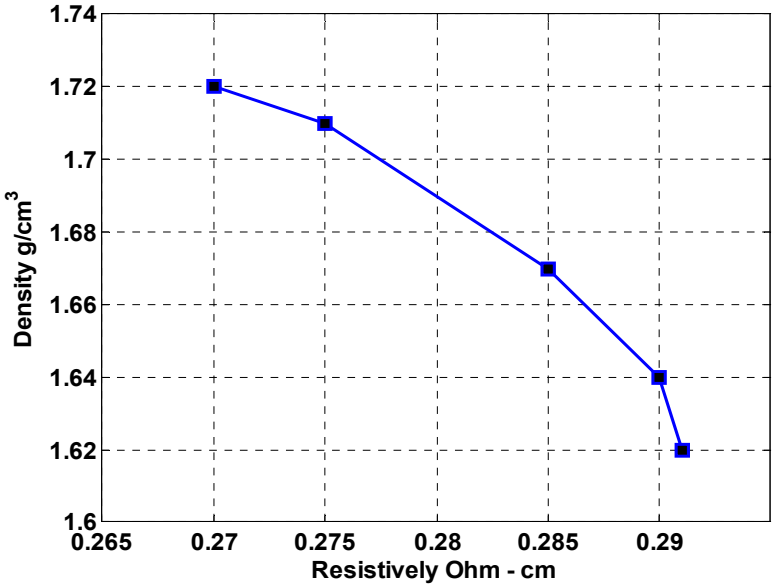

Figure 7.

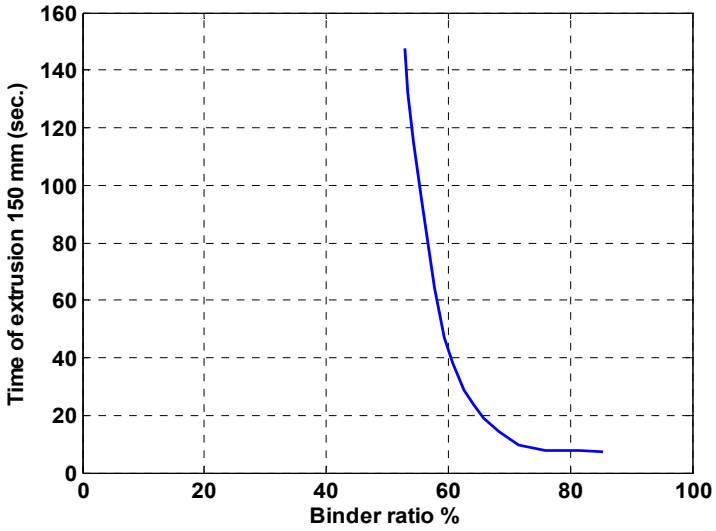

Figure 8.

Modern Applied Science

www.ccsenet.org/journal.html

Vol. 3, No. 3

March 2009

Study on the Sensitive Property of Poly (AMPS-co-DMAEMA) Hydrogel under Electric Stimulation

Liewen Liao

School of Materials Science and Engineering

Northwestern Polytechnical University

Xi'an 710072, China

Institute of Green Chemical Engineering

ZhongKai University of Agriculture and Engineering

Guangzhou 510225, China

Zhengtang Liu

School of Materials Science and Engineering

Northwestern Polytechnical University

Xi'an 710072, China

Hangbo Yue & Yingde Cui

Institute of Green Chemical Engineering

ZhongKai University of Agriculture and Engineering

Guangzhou 510225, China

Tel: 86-20-8901-3955 E-mail: liaolw@163.com

The research is financed by the National Natural Science Foundation of China (No. 20176007 & No. 20376087). (Sponsoring information)

Abstract

Taking 2-acrylamido-2-methylpropane sulfonic acid (AMPS) and 2-dimethylamino ethyl methacrylate (DMAEMA) as monomers, taking N,N'-methylenebis acrylamide as the cross linker, and taking the ammonium persulfate and sodium bisulfite as the redox initiators, we adopted the aqueous polymerization to prepare the Ploy(AMPS-co-DMAEMA) hydrogel and studied the shrinking and bending behaviors of hydrogel under exterior DC electric field stimulation. The result indicated that the DMAEMA monomer content and the pressure could significantly influence the electric sensitivity of hydrogel. With the increase of the DMAEMA content and the non-contract electric field, the Poly(AMPS-co-DMAEMA) hydrogel first bended toward the cathode and then bended toward the anode.

Keywords: Hydrogel, Electric stimulation response, 2-acrylamido-2-methylpropane sulfonic acid (AMPS), 2-dimethylamino ethyl methacrylate (DMAEMA)

According to the response of hydrogel to the exterior stimulation, the hydrogel can be divided into traditional hydrogel and intelligent hydrogel, and the intelligent hydrogel can perceive exterior tiny physically chemical stimulations such as temperature, electric field, magnetic field, light, pH, ion strength and pressure, and show significant expansions or responses in the response process. We can utilize this characteristic to apply the intelligent hydrogel into the medicine controlled release, chemical convertor, memory component switch, artificial muscle and many domains (He, 1997, P.118-127, Moschou, 2004, P.499-502, Hamlem, 1965, P.1149-1150).

The DMAEMA molecule contains alkaline tertiary amine which can be turned into protons and presents characteristic of positive ion in the acidic medium (Huang, 2003, P.177-182). The sulfoacid group in the AMPS molecule has high charge density, and it is easy to be dissociated as sulfoacid ion and presents the characteristic of negative ion. In this article, we took the N,N'-methylenebis acrylamide as the cross linker, took the ammonium persulfate and sodium bisulfite as the redox initiators, and adopted the free radical polymerization process to prepare the Poly(AMPS-co-DMAEMA) hydrogel, and studied the sensitivity under the stimulation of the electric field.

1. Experiment

1.1 Main reagents and apparatus

The main reagents in the experiment included AMPS (industrial class, made by Guangzhou Shuangjian Trading Co., Ltd), DMAEMA (industrial class, made by Guangzhou Shuangjian Trading Co., Ltd), N,N'-methylenebis acrylamide (MBAAm) (analytical pure, made by Tianjin Kermel Chemical Reagent Co., Ltd), ammonium persulfate (analytical pure, made by Tianjin Kermel Chemical Reagent Co., Ltd), sodium bisulfite (analytical pure, made by Tianjin Kermel Chemical Reagent Co., Ltd) and other reagents which were general analytic pure and didn't be treated before using.

The apparatus in the experiment included Spectrum 2000 Fourier Transform Infrared Spectrometer (Pekin-Elmer, USA), JY600 Electrophoresis Apparatus Trophoresis Power Supply (made by Beijing Junyi Dongfang Electrophoresis Equipment Co., Ltd), 902C Platinum Electrode and Electric Heat Constant Temperature Water Bath.

1.2 Preparation of hydrogel

Weighed certain quantitative monomeric AMPS, DMAEMA and cross linker MBAAm according to Table 1, added proper quantitative distilled water to make it dissolved, and added quantitative ammonium persulfate and sodium bisulfite, mixed up and encaseed miscible liquids into the plastic pipe (which diameter was 6mm and the length was 20cm) and pressurized it, and put it in the constant temperature water bath of 50℃ and produced the hydrogel. Marinate the hydrogel into the deionized water for three days, and changed water twice one day to eliminate the monomers which didn't react. Finally, put the hydrogels into the vacuum drying oven to dry until constant weight, and the drying hydrogel could be used in the infrared spectrum test.

1.3 Infrared spectrum token of hydrogel

Made the infrared spectrum test to the hydrogel sample by the Spectrum 2000 Fourier Transform Infrared Spectrometer (Pekin-Elmer, USA), and the scanning range was 500~4000cm^{-1}, and the resolution was 4cm^{-1}.

1.4 Electric stimulation shrinking behavior of hydrogel

First, made the hydrogel expand in the distilled water, and chopped the expanded hydrogel into column forms (the bottom diameter was 8mm, and the altitude was 10mm), and put them into the measurement equipment, and put a pair of platinum electric characteristic into the hydrogel along the horizontal directions from two sides. Connected the power supple, and took out the dehydrated gelatin, absorbed the surface water and measured them again. Computed the mass maintenance rate (R_m) according to the formula (1).

$$R_m(\%) = m_t / m_f \times 100 \quad (1)$$

Where, m_t was the mass of the gelatin through electrification of t time (g), and m_f was the mass of the hydrogel before electrification (g).

1.5 Electric stimulation bending performance of hydrogel

First, expanded the hydrogel in the NaCl liquor with 0.8% of mass concentration, and chopped the expanded hydrogel into the gelatin bars (20mm×2mm×1mm), and put them into the culture dish with a few NaCl solution and lucid bottom. Vertically put two parallel electric characteristic which interval was 20mm in the culture dish, and made the gelatin bars vertical to the direction of the two electric characteristic and in the middle position of two electric characteristic, and fixed one end of the gelatin bars, and put the angle measurement equipment on the bottom of the culture dish. Threw pressure to the gelatin, and measured the curve degree of the gelatin through reading the angle deviation of the gelatin on the angle measurement equipment. When the gelatin bar achieved the maximum curve angle under the electric simulation, cut off the power supply and read the number, and regulated that when the gelatin bended toward the cathode, the curve angle was positive, and when the gelatin bended toward the anode, the curve angle was negative.

2. Results and discussions

2.1 Infrared spectrum analysis of Poly(AMPS-co-DMAEMA) hydrogel

Figure 1 was the infrared spectrum of the Poly(AMPS-co-DMAEMA) hydrogel, and the flexing libration absorption apex of the amido group in the AMPS molecule occured at 1665 cm^{-1}, and the flexing libration absorption apex of the ester group in the DMAEMA molecule occured at 1730 cm^{-1}. But characteristic absorption apex (at about 1640 cm^{-1}) of the unsaturated double-linkage didn't exist, which indicated that two sorts of monomers have produced the polymerization reaction.

2.2 Electric simulation deswelling behavior of hydrogel

2.2.1 Hydrogel deswelling kinetics under constant pressure

The change of the mass maintenance rate of expanded Poly (AMPS-co-DMAEMA) hydrogel under the 15V contact pressure stimulation with the time was seen in Figure 2.

From Figure 2, under the situation that the pressure kept at 15V, with the delay of electrification time, the Rm value of the hydrogel would decrease gradually. With the increase of the DMAEMA content in the copolymer, the Rm value of the hydrogel also decreased in turn.

The reason might be that acidic sulfonic group and alkali tertiary amine existed in the Poly(AMPS-co-DMAEMA) hydrogel network. A90D10 hydrogel contained more AMPS main chain, and when the content of the side chain sulfonic group was more, the hydrophilicity and the conductivity were better. DMAEMA molecule in the A50D50 hydrogel contained hydrophobic ester group, and the hydrophobic side groups on the macromolecule chain would assemble and form hydrophobic micelles, and the macromolecule chain would present austere conformation (Zhang, 2002, P.25-29), so the expansion change degree of the hydrogel with much DMAEMA would decrease.

2.2.2 Influence of pressure on the hydrogel shrinking behavior

The hydrogel shrinking influence result under different DC pressure stimulation was seen in Figure 3. From Figure 3, when the electrification time kept 30min, with the increase of pressure, the Rm value would gradually decrease. And with the increase of the DMAEMA content in the copolymer, the shrinking degree of the gelatin volume would be delayed.

For general polyelectrolyte hydrogel, under the function of electric field, the transfer speed of the movable counterion was related with the electric field tension except for the character of the ion (ion radius and charges) (Ma, 2002). With the increase of the pressure, the transfer speed of the charged ion increased. With the transfer of the ions with different electric characteristic in the gelatin network, because of the function of electrostatic attraction, part of charges on the poly ion group in the gelatin network would be shielded, the decrease of the charged poly ion quantity would reduce the "distracting" function of the gelatin to the water, and the moisture would be exuded into the gelatin network. For the Poly(AMPS-co-DMAEMA) gelatin with different matching ratios, with the increase of the voltage, the Rm value would gradually decrease.

2.3 Electric simulation bending behavior of hydrogel

The influencing result of the pressure to the bending behavior of gelatin is seen in Figure 4, and the exterior pressure would act on the hydrogels with different components through the NaCl solution with 0.8% of mass concentration.

From Figure 4, under the stimulation of non-contact DC pressure, A90D10 hydrogel bended toward cathode, and A50D50 hydrogel bended toward anode, and A70D30 hydrogel first bended toward cathode and then bended toward anode and with the increase of pressure, the curve angle of the gelatin would increase with it.

The reason might be that the electric characteristic of the poly ion group in the sample gelatin network were different. For A90D10 hydrogel, the poly ion group in the gelatin network presented the characteristic of negative ion. For A50D50 hydrogel, the poly ion group presented certain characteristic of positive ion. With the increase of pressure, the poly ion group in the A70D30 hydrogel network changed from the characteristic of negative ion to the characteristic of positive ion, so it first bended toward the cathode and then bended toward the anode, and the function of the osmotic pressure might influence the electrode change of the poly ion group, and the electric stimulation response mechanism should be further studied by scholars. Through adjusting the pressure, the bending direction of Poly(AMPS-co-DMAEMA) hydrogel could be controlled, which indicated that this sort of hydrogel material possessed potential application foreground in many domains such as bionic material and chemical valve.

3. Conclusions

In this article, we prepared the Poly(AMPS-co-DMAEMA) hydrogel through the aqueous solution polymerization method, and measured the sensitivity under the simulation of the electric field. The results included (1) under the direct contact pressure stimulation, the mass maintenance rates of A900D10, A70D30 and A50D50 decreased in turn under same condition, and with the increase of the pressure, the shrinking phenomena of hydrogel were more and more obvious, (2) under the non-contact electric field stimulation, A90D10 hydrogel bended toward cathode, A50D50 hydrogel bended toward anode, and A70D30 first bended toward cathode and then bended toward anode with the increase of pressure.

References

Hamlem R P, Kent C E & Shafer S N. (1965). Electrolytically Activated Contractile Polymers. *Nature.* No.206. P.1149-1150.

Heqing & Shengjing. (1997). Response Hydrogel and Its Application in Medicine Controlled Release. *Journal of Functional Polymers.* No.10(1). P.118-127.

Huangyi, Fan, Xiaodong & Huhui et at. (2003). Synthesis and Characterization of Novel Hydrogels of Poly(DMAEMA-co-β-Cyclodextrin Acrylate). *Acta Polymerica Sinica.* No.2. P.177-182.

Ma, Xinglan & Xue, Shuiqiang. (2002). *Physical Chemistry.* Xuzhou: China University of Mining and Technology

Press.

Moschou E A, Peteu S F, Bachas L G, et al. (2004). Artificial muscle material with fast electro actuation under neutral pH conditions. *Chemistry of Materials.* No.16(12). P.499-502.

Zhang, Jianhe & Yang, Yajiang. (2002). Stimuli-Response of Hydrophilic-Hydrophobic Semi-IPN Hydrogels under DC Electric Field. *Acta Polymerica Sinica.* No.1. P.25-29.

Table 1. Feed composition of Poly(AMPS-co-DMAEMA) hydrogel[a]

Hydrogel[b]	AMPS (mol %)	DMAEMA (mol %)	Crosslink agent (mol %)	Initiator (mol %)	Total concentration of monomer (mol/L)
A90D10	90	10			
A70D30	70	30	1	1	1
A50D50	50	50			

Note: [a]: The amount of crosslink agent or initiator is mole percent (mol %) of total monomer content.

[b]: The A90D10, A70D30 and A50D50 hydrogels respectively denote n(AMPS):n(DMAEMA)=9:1, 7:3, 5:5.

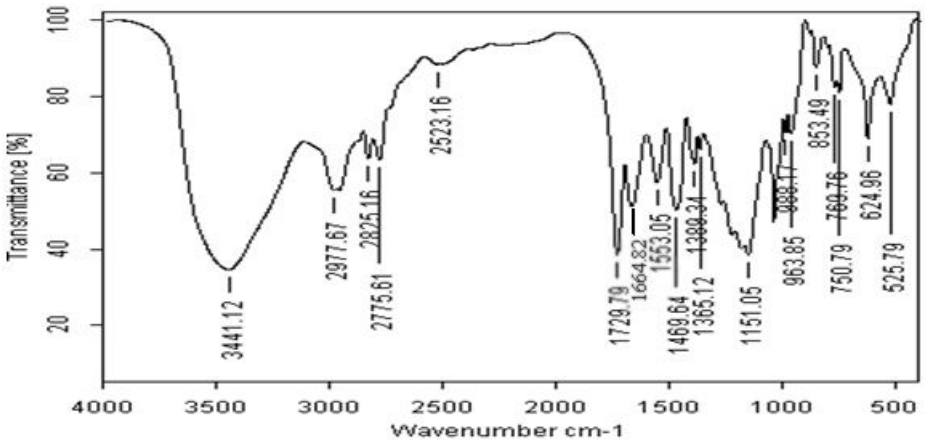

Figure 1. FTIR Spectrum of Poly(AMPS-co-DMAEMA) Hydrogel

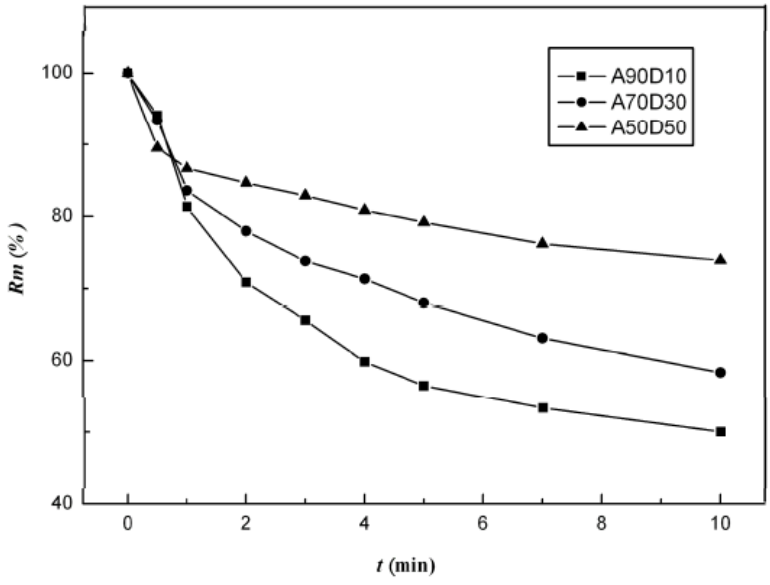

Figure 2. Shrinking Behavior of Poly(AMPS-co-DMAEMA) Hydrogel under 15V Electrical Stimulation

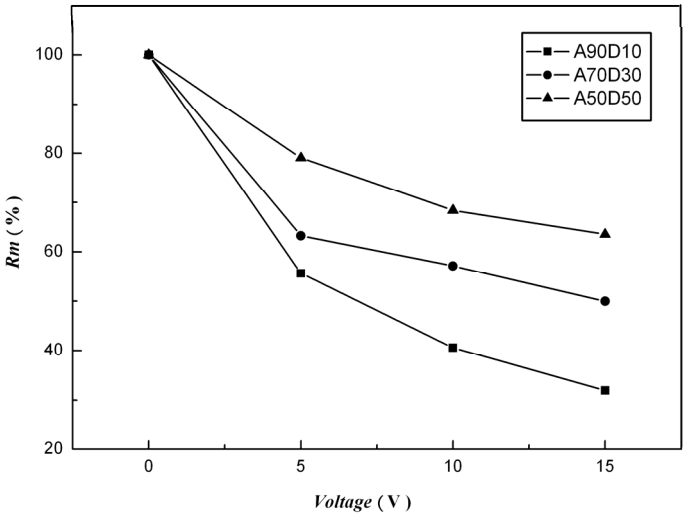

Figure 3. Shrinking Behavior of Poly(AMPS-co-DMAEMA) Hydrogel under Electrical Stimulation for 30min

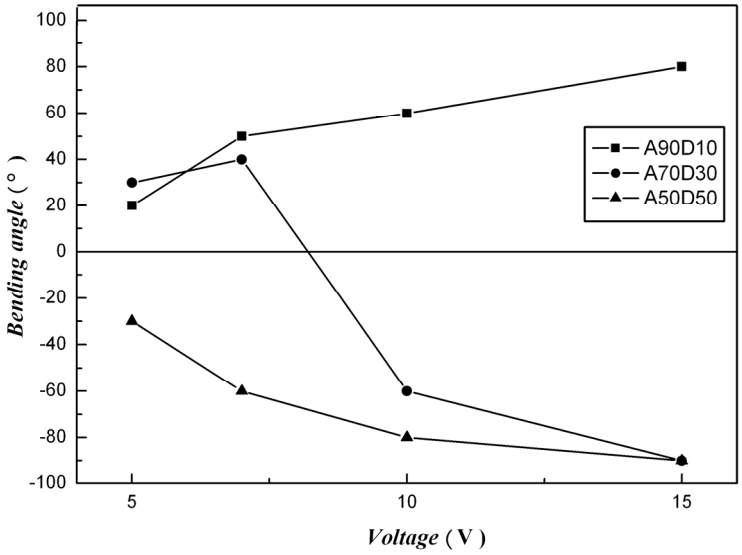

Figure 4. The Effects of the Applied Voltage on the Bending Angle of Poly(AMPS-co-DMAEMA) Hydrogel in 0.8wt% NaCl aqueous solution

Modern Applied Science

www.ccsenet.org/journal.html

Vol. 3, No. 3

March 2009

Partially Null Curves of Constant Breadth in Semi-Riemannian Space

Süha Yılmaz

Buca Educational Faculty, Dokuz Eylül University

35160, Buca-Izmir, Turkey

E-mail: suha.yilmaz@yahoo.com

Melih Turgut (Corresponding author)

Buca Educational Faculty, Dokuz Eylül University

35160, Buca-Izmir, Turkey

E-mail: melih.turgut@gmail.com

Abstract

In this work, some characterizations of partially null curves of constant breadth in Semi-Riemannian space are presented.

Keywords: Semi-Riemannian Space, Partially Null Curves, Curves of Constant Breadth

1. Introduction

Curves of constant breadth were introduced by L. Euler, 1780. Ö. Köse (1984) wrote some geometric properties of plane curves of constant breadth. And, in another work Ö. Köse (1986) extended these properties to the Euclidean 3-Space E^3. Moreover, M. Fujivara (1914) obtained a problem to determine whether there exist space curve of constant breadth or not, and he defined '*breadth*' for space curves and obtained these curves on a surface of constant breadth. A. Magden and Ö. Köse (1997) studied this kind curves in four dimensional Euclidean space E^4.

E. Cartan opened door of notion of null curves (for more details see C.Boyer, 1968). And, thereafter null curves were deeply studied by W.B. Bonnor (1969) in Minkowski space-time. In the same space, special null; *Partially and Pseudo Null curves* are defined by J. Walrave (1995). Additionally, M. Petrovic et. al. (2005) defined Frenet equations of pseudo null and partially null curves in E_2^4.

In this paper, we extend the notion of curves of constant breadth to null curves in Semi-Riemannian space. Some characterizations are obtained by means of Frenet equations defined by M. Petrovic et. al.(2005). We used the method of Ö. Köse (1984).

2. Preliminary Notes

To meet the requirements in the next sections, here, the basic elements of the theory of curves in the space E_2^4 are briefly presented. A more complete elementary treatment can be found in B. O'Neill (1983).

Semi-Riemannian space E_2^4 is an Euclidean space E^4 provided with the standard flat metric given by

$g = -dx_1^2 - dx_2^2 + dx_3^2 + dx_4^2$,

where (x_1, x_2, x_3, x_4) is a rectangular coordinate system in E_2^4.

Since g is an indefinite metric, recall that a vector $\vec{v} \in E_2^4$ can have one of the three causal characters; it can be space-like if $g(\vec{v},\vec{v})\rangle 0$ or $\vec{v} = 0$, time-like if $g(\vec{v},\vec{v})\langle 0$ and null (light-like) if $g(\vec{v},\vec{v}) = 0$ and $\vec{v} \neq 0$. Similarly, an arbitrary curve $\vec{\alpha} = \vec{\alpha}(s)$ in E_2^4 can be locally be space-like, time-like or null (light-like), if all of its velocity vectors $\vec{\alpha}'(s)$ are respectively space-like, time-like or null. Also, recall the norm of a vector $\vec{v}$ is given by $\|\vec{v}\| = \sqrt{|g(\vec{v},\vec{v})|}$. Therefore, $\vec{v}$ is a unit vector if $g(\vec{v},\vec{v}) = \pm 1$. Next, vectors $\vec{v},\vec{w}$ in E_2^4 are said to be orthogonal if $g(v,w) = 0$. The velocity of the curve $\vec{\alpha}$ is given by $\|\vec{\alpha}'\|$. Thus, a space-like or a time-like curve $\vec{\alpha}$ is said to be parametrized by arclength function s, if $g(\vec{\alpha}',\vec{\alpha}') = \pm 1$. Let $\vec{a},\vec{b}$ be two space-like vectors in E_2^4, then, there is unique real

number $0 \le \delta \le \pi$, called angle between $\vec{a}$ and $\vec{b}$, such that $g(\vec{a},\vec{b}) = \|\vec{a}\|\|\vec{b}\|\cos\delta$.

Denote by $\{\vec{T}(s), \vec{N}(s), \vec{B}_1(s), \vec{B}_2(s)\}$ the moving Frenet frame along the curve $\vec{\alpha}$ in the space E_2^4. Then $\vec{T}, \vec{N}, B_1, B_2$ are, respectively, the tangent, the principal normal, the first binormal and the second binormal vector fields. Recall that a space-like curve with time-like principal normal $\vec{N}$ and null first and second binormal is called a partially null curve in E_2^4 M. Petrovic et. al. (2005). Let $\vec{\alpha}$ be a partially null curve in the space E_2^4, parametrized by arclength function s. Then for the curve $\vec{\alpha}$ the following Frenet equations are given by M. Petrovic et. al. (2005):

$$\begin{bmatrix} \vec{T}' \\ \vec{N}' \\ \vec{B}_1' \\ \vec{B}_2' \end{bmatrix} = \begin{bmatrix} 0 & \kappa & 0 & 0 \\ \kappa & 0 & \tau & 0 \\ 0 & 0 & \sigma & 0 \\ 0 & \tau & 0 & -\sigma \end{bmatrix} \begin{bmatrix} \vec{T} \\ \vec{N} \\ \vec{B}_1 \\ \vec{B}_2 \end{bmatrix}$$

where $\vec{T}, \vec{N}, B_1$ and $\vec{B}_2$ are mutually orthogonal vectors satisfying equation

$$g(\vec{T},\vec{T}) = 1, g(\vec{N},\vec{N}) = -1, g(\vec{B}_1,\vec{B}_1) = g(\vec{B}_2,\vec{B}_2) = 0, g(\vec{B}_1,\vec{B}_2) = 1,$$

And here, $\kappa(s), \tau(s)$ and $\sigma(s)$ are first, second and third curvature of the curve $\vec{\alpha}$, respectively.

M. Petrovic et. al. (2005) gave a characterization about partially null curves with the following statement.

Theorem 2.1 A partially null unit speed curve $\vec{\varphi} = \vec{\varphi}(s)$ in E_2^4, with curvatures $\kappa \neq 0, \tau \neq 0$ for each $s \in I \subset R$ has $\sigma = 0$ for each s.

3. Partially Null Curves of Constant Breadth in E_2^4

Let $\vec{\varphi} = \vec{\varphi}(s)$ be a simple closed partially null curve in the space E_2^4. These curves will be denoted by C. The normal plane at every point P on the curve meets the curve at a single point Q other than P. We call the point Q the opposite point of P. We consider a partially null curve in the class Γ as in M. Fujivara (1914) having parallel tangents $\vec{T}$ and $\vec{T}^*$ in opposite directions at the opposite points $\vec{\varphi}$ and $\vec{\varphi}^*$ of the curve. A simple closed curve of constant breadth having parallel tangents in opposite directions at opposite points can be represented with respect to Frenet frame by the equation

$$\vec{\varphi}^* = \vec{\varphi} + m_1\vec{T} + m_2\vec{N} + m_3\vec{B}_1 + m_4\vec{B}_2, \tag{1}$$

where $m_i(s), 1 \le i \le 4$ arbitrary functions of s and $\vec{\varphi}$ and $\vec{\varphi}^*$ are opposite points. Vector $\vec{d} = \vec{\varphi}^* - \vec{\varphi}$ is called 'the distance vector' of C. Differentiating both sides of (1) and considering Frenet equations, we have

$$\frac{d\vec{\varphi}^*}{ds} = \vec{T}^*\frac{ds^*}{ds} = (\frac{dm_1}{ds} + m_2\kappa + 1)\vec{T} + (\frac{dm_2}{ds} + m_1\kappa + m_4\tau)\vec{N} + (\frac{dm_3}{ds} + m_2\tau)\vec{B}_1 + (\frac{dm_4}{ds})\vec{B}_2. \tag{2}$$

Since $\vec{T}^* = -\vec{T}$. Rewriting (2), we obtain following system of equations,

$$\begin{pmatrix} \frac{dm_1}{ds} + m_2\kappa + 1 + \frac{ds^*}{ds} = 0 \\ \frac{dm_2}{ds} + m_1\kappa + m_4\tau = 0 \\ \frac{dm_3}{ds} + m_2\tau = 0 \\ \frac{dm_4}{ds} = 0 \end{pmatrix}. \tag{3}$$

If we call ϕ as the angle between the tangent of the curve C at point $\vec{\varphi}$ with a given fixed direction and consider $\frac{d\phi}{ds} = \kappa$, we have (3) as follow:

$$\left(\begin{array}{l} \dfrac{dm_1}{d\phi} = -m_2 - f(\phi) \\ \dfrac{dm_2}{d\phi} = -m_1 - m_4\rho\tau \\ \dfrac{dm_3}{d\phi} = -m_2\rho\tau \\ \dfrac{dm_4}{d\phi} = 0 \end{array}\right), \tag{4}$$

where $f(\phi) = \rho + \rho^*$, $\rho = \dfrac{1}{\kappa}$ and $\rho^* = \dfrac{1}{\kappa^*}$ denote the radius of curvatures at $\vec{\varphi}$ and $\vec{\varphi}^*$, respectively. It is not difficult to see that $m_4 = c_4 = \text{constant}$. Then, using system (4), we easily have the following differential equations with respect to m_1 and m_2 as

$$\left(\begin{array}{l} \dfrac{d^2 m_1}{d\phi^2} - m_1 + \dfrac{df}{d\phi} - c_4\rho\tau = 0 \\ \dfrac{d^2 m_2}{d\phi^2} + m_2 + c_4 \dfrac{d}{d\phi}(\rho\tau) - f(\phi) = 0 \end{array}\right). \tag{5}$$

These equations are characterizations for the curve $\vec{\varphi}^*$. If the distance between opposite points of C and C^* is constant, then, due to null frame vectors, we can write that

$$\left\|\vec{\varphi}^* - \vec{\varphi}\right\| = m_1^2 - m_2^2 + 2m_3 m_4 = l^2 = \text{constant}. \tag{6}$$

Hence, by the differentiation we have

$$m_1 \frac{dm_1}{d\phi} - m_2 \frac{dm_2}{d\phi} + m_3 \frac{dm_4}{d\phi} + m_4 \frac{dm_3}{d\phi} = 0. \tag{7}$$

Considering system (4), we get

$$m_1\left(\frac{dm_1}{d\phi} + m_2\right) = 0. \tag{8}$$

Since, we arrive $m_1 = 0$ or $\dfrac{dm_1}{d\phi} = -m_2$. Therefore, we shall study in the following cases.

Case 1: $m_1 = 0$. Moreover, let us suppose that $c_4 \neq 0$. In this case $(5)_1$ deduce other components, respectively,

$$m_2 = -f(\phi) = -c_4 \int_0^{\phi} \rho\tau \, d\phi \tag{9}$$

and

$$m_3 = -\int_0^{\phi} (\rho + \rho^*)\rho\tau \, d\phi. \tag{10}$$

Additionally, it is safe to report that the following relation hold:

$$\rho^* = -\rho - c_4 \int_0^{\phi} \rho\tau \, d\phi. \tag{11}$$

And if $c_4 = 0$, we have $f(\phi) = c = \text{constant}$. By this way, we know

$$\left(\begin{array}{l} m_2 = -c \\ m_3 = c\displaystyle\int_0^{\phi} \rho\tau \, d\phi \\ \rho^* + \rho + c = 0 \end{array}\right). \tag{12}$$

Case 2: $\frac{dm_1}{d\phi} = -m_2$. In this case, from $(4)_1$ we know $f(\phi) = m_2 = 0$. And first let us suppose that $c_4 \neq 0$. Thus the equation $(5)_1$ has the form

$$\frac{d^2 m_1}{d\phi^2} - m_1 = c_4 \rho\tau. \tag{13}$$

By the method of variation of parameters, the solution of (13) yields that

$$m_1 = e^{\phi}\left[A + \frac{c_4}{2}\int_0^{\phi} \rho\tau\, e^{-\phi} d\phi \right] + e^{-\phi}\left[B - \frac{c_4}{2}\int_0^{\phi} \rho\tau\, e^{\phi} d\phi \right], \tag{14}$$

where A, B are real numbers. Denoting $\frac{dm_1}{d\phi} = \xi(\phi)$, we have other component

$$m_3 = \int_0^{\phi} \rho\tau\, \xi\, d\phi. \tag{15}$$

Last, we know that

$$\rho^* + \rho = 0. \tag{16}$$

And if $c_4 = 0$, we write that

$$\frac{d^2 m_1}{d\phi^2} - m_1 = 0. \tag{17}$$

Using hyperbolic functions, we write the solution of (17) as

$$m_1 = l_1 \cosh\phi + l_2 \sinh\phi. \tag{18}$$

Considering (4), we have other components,

$$m_2 = -l_1 \sinh\phi - l_2 \cosh\phi \tag{19}$$

and

$$m_3 = \int_0^{\phi} (l_1 \cosh\phi + l_2 \sinh\phi)\rho\tau\, d\phi. \tag{20}$$

Case 3: $m_1 = c_1 = \text{constant} \neq 0$ and $m_2 = 0$. Using $(5)_{1,}$ we arrive

$$\rho\tau = \text{constant}. \tag{21}$$

Corollary 3.1 In case 3, c_4 cannot be zero.

References

A. Magden and Ö. Köse, On The Curves of Constant Breadth, *Tr. J. of Mathematics*, 1 (1997), 277-284.

B. O'Neill, *Semi-Riemannian Geometry*, Academic Press, New York, 1983.

C.Boyer, *A History of Mathematics*, New York: Wiley, 1968.

J. Walrave, Curves and surfaces in Minkowski space. Dissertation, K. U. Leuven, Fac. of Science, Leuven (1995)

L. Euler, De Curvis Trangularibis, *Acta Acad. Petropol* (1780), 3-30.

M. Fujivara, On Space Curves of Constant Breadth, *Tohoku Math. J.* 5 (1914), 179-184.

M. Petrovic-Torgasev, K.Ilarslan and E. Nesovic, On partially null and pseudo null curves in the semi-euclidean space R_2^4. *J.of Geometry*. 84 (2005) 106-116.

Ö. Köse, Some Properties of Ovals and Curves of Constant Width in a Plane, *Doga Sci. J. Serial B* (8) 2 (1984), 119-126.

Ö. Köse, On Space Curves of Constant Breadth, *Doga Turk Math. J.* (10) 1 (1986), 11-14.

W. B. Bonnor, Null curves in a Minkowski space-time, *Tensor*. 20 (1969) 229-242.

Modern Applied Science

www.ccsenet.org/journal.html

Vol. 3, No. 3

March 2009

Application of In-situ Synthesized TiC Reinforced Ni Based Composite Coatings by Laser Cladding on Piercing Plug

Yongqiang Guo

School of Mechanical & Electronic Engineering

Tianjin Polytechnic University

Tianjin 300160, China

E-mail: gyq0818@163.com

Abstract

In this article, the advantages of laser cladding were briefly introduced, and a method for improving the life of piercing plug was provided by the laser cladding experiment. In situ formation of TiC particles reinforced Ni-base composite coating was prepared on the surface of piercing plug material H13 steel by CO_2 laser. The microstructure of the clad layer was characterized by SEM, EDX and XRD. The microhardness and wear resistance of the laser clad layer was examined. The results show that laser clad layer can be achieved under technical processing parameters and that the good metallurgical bonding is formed between the coating and substrate. The coating is uniform, continuous and free of pores and cracks. The microstructure of the clad layer contains the TiC reinforced phase. The microhardness of the clad layer is 800-950HV0.2, about 2.5-3 times larger than that of the substrate. The clad layer is reinforced by particles and grain-refining, resulting in greatly increase in life comparing with piercing plug material H13 steel.

Keywords: Laser cladding, Piercing plug, Clad layer, Wear resistance

1. Introduction

In the process of rolling seamless steel pipe, the consumption of piercing plug is the biggest one of the mold (Cao, 1998, p.51-55). The piercing plug contacts directly with high-temperature steel in the production of seamless steel pipe, and bears a great friction in the process of piercing. At the same time, the piercing plug exists mechanical shock and other effects, so that it occurs much failure such as nasal cavity collapse, deformation, steel plating and cracking in the earlier. Therefore piercing plug manufacturing has become a key tool for high-quality steel pipe. The development of high-quality piercing plug is required in the production of seamless steel pipe (Zhang, 2000, p.187-190).

Laser cladding technology has developed rapidly in recent years. Some research shows that laser cladding metal matrix composite ceramic coating materials can significantly improve the wear-resistance (Qu, 2008, p.1546-1551 & Xu, 2006, p.486-492 & Ocelik, 2005, p.303-315). The ceramic coating particles can be getted by “plus” method, and also can be getted by "in-situ synthesis" in the process of laser cladding. In recent years, the use of "in-situ synthesis" of metal-ceramic composite coating technology has been concerned extensively at home and abroad (Li, 2006, p.8-12 & Yang, 2006, p.519-525 & Yang, 2002, p.26-30).

In this paper, selecting NiCrBSi(Ni60)+Ti+C as the clad material, In situ formation of TiC particles reinforced Ni-base composite coating was prepared on the surface of piercing plug by the way of laser cladding. Analysis the microstructure of the laser clad layer. Test the hardness and wear properties of the laser clad layer. It aims to improve the life of piercing plug.

2. Experimental procedures

H13 steel of dimensions 20mm×20mm×50mm was used as the substrate, its chemical composition(quality scores,%) are 0.32-0.42C, 4.75-5.5Cr, 1.1-1.75Mo, 0.8-1.2V, 0.8-1.2Si, 0.2-0.5Mn and Fe cushion. Powder mixture of NiCrBSi(Ni60)+Ti+C in volume ratio of 20:4:1, was used as the clad material, which was replaced on H13 steel with a thickness of 1mm.

A continuous TJ-HL-T5000 CO2 laser processing system was used for laser cladding. An overlap of 50% between successive tracks was selected and argon gas was used as shielding gas during laser cladding process. The process parameters of laser cladding were: laser power of 1.5-2kW, scanning velocity of 3–10mm/s and laser beam diameter of 3 mm.

The morphology of the irradiated sample was characterized by scanning electron microscopy (SEM) with QUANTA200-scanning electron microscope, which could determine the thickness of the modified layer. These studies

were complemented with EDX. The crystalline structure was analysed by X-ray diffractometry (XRD) with D8 diffractometer. In order to get some knowledge of the mechanical properties of the treated surface, its hardness was performed by nanoindentation with HXD-1000T electron microscopy hardness, whereas the weight loss of laser clad pin-specimens was measured using a high accuracy analytic balance (10^{-5}g). Surface roughness of worn surface was tested by JB-4C Precision instrument roughness.

3. Results and discussion

3.1 Microstructure of laser clad coatings

Figure 1shows a X-ray diffraction spectrums of the clad coatings. According to the indexed results of the X-ray diffraction spectrums, the main phase constituents in the coatings include: γ-Ni, Cr_7C_3 and TiC.

Figure 2 shows the SEM micrograph of the cross-section of the coatings under different magnification. Figure 2. (a) is SEM micrographs showing the morphology under low magnification, Figure 2. (b) is SEM micrographs showing the morphology under high magnification of A zone in the Figure 2. (a). According to microstructure difference, the laser clad coatings is constitute of dendrite and lumpish particles. The lumpish particles are 1-3μm.

In order to further the reaction product of the confirmation, the EDX spectrum analysis of dendrite and lumpish particles was shown in Figure 3. According to dendrite of the spectrum analysis, it is composite of (wt%) 56.84Cr, 1.37Ti, 20.38Fe, 12.97Ni, 7.33C, 1.10Si, its elements for the formation of Cr and C compounds. Therefore, certain dendrite for Cr_7C_3. According to lumpish particles of the spectrum analysis, it is composite of (wt%) 55.69Ti, 13.41Cr, 16.58C, 2.37Si, 6.30Fe, 5.65Ni, its elements for the formation of Ti and C compounds. Therefore, it was identified that the lumpish particles was TiC.

3.2 Hardness of coatings and Wear resistance

The microhardness distribution curve across the depth of the laser clad layer is plotted in Figure 4. The hardness of laser cladding in 800-950HV0.2 than the substrate increase by 2.5 to 3 times. The binding of clad layer and the substrate with the hardness is in the area around 600HV0.2.

Multi-channel laser cladding lap of the sample was cutted into 25mm×7mm×7mm, and do the wear test with GCr15. Friction process parameters: normal load N=100N, sliding speed V=400r/min, Wear time T=3600s. Figure 5 show the wear weight loss of clad layer and H13 steel. Under the same wear condition, the wear weight loss of clad layer was 0.0132mg and the wear weight loss of H13 steel was 0.1365mg. The wear weight loss of clad layer was 10 percent as that of H13 steel.

The surface roughness parameters of worn surface of laser clad layer and H13 steel in Table 1. From the Table 1, the average roughness Ra of worn surface, the contour maximum height R_Y, the ten height R_Z, the average distance S of outline of an single-spacing and the average distance S_m of profile of laser clad layer are obviously smaller than that of H13 steel. It shows that the wear track of laser clad layer is Small and shallow and the wear track of H13 steel is deep and wide.

In view of the wear test analysis, it seems that laser clad in situ TiC reinforced Ni composite coatings excellent wear resistance. It was mainly due to a lot of TiC particles was in the clad layer. When the worn of clad layer was in the process of wear, TiC particles revealed in the worn surface. On the one hand, the TiC particles which revealed in the worn surface played a supporting role. On the other hand, the TiC particles play a protection role on the substrate. Thus greatly reduce the worn of substrate. In view of the of the microstructure analysis, the microstructure of laser clad layer was very small. The clad layer not only contained the Cr, Fe, Si, but also contained a lot of Ti. Thus produce grain-refining and particles strengthen and make the clad layer has high strength and toughness. It result in greatly increase in wear resistance comparing with H13 steel. In other words, It result in greatly increase in life comparing with piercing plug material H13 steel.

4. Conclusions

Crack and porous free composite coatings consisting of Ni alloy reinforced with in situ formation of TiC particles were successfully obtained by laser cladding under optimal parameters on H13 steel substrates from powder mixtures of Ni alloy, Ti and C. The microstructure of the coating is mainly composed of γ-Ni, Cr_7C_3 and TiC particles. The microhardness of the coatings is between 800 and 950HV0.2, about 2.5-3 times larger than that of the substrate. The laser clad layer is reinforced by particles and grain-refining, resulting in greatly increase in life comparing with piercing plug material H13 steel.

References

Cao, Pengjun & Wu, Haidong. (1998). Studies about prolonging service life of piercing plug. *Steel Pipe*, 27(1), 51-55.

Li, Jing, Zhong, Minlin & Liu, Wenjin. (2006). Microstructures and properties of laser clad in situ particle reinforced Ni-Base composite coating on 55Mn steel. *Heat Treatment of Metals*, 31(11), 8-12.

Ocelik, V, Matthews, D & DeHosson J Th M. (2005). Sliding wear resistance of metal matrix composite layers prepared by high power laser. *Surface and Coatings Technology*, 197(2-3), 303-315.

Qu, Shiyao, Wang, Xinhong & Zhang, Min. (2008). Microstructure and wear properties of Fe-TiC surface composite coating by laser cladding. *Journal of Materials Science*, 43(5), 1546-1551

Wu, Xiaolei & Chen, Guangnan. (1998). Microstructural characteristics and wear properties of in situ Formed TiC Ceramic Reinforced metal-matrix composites coatings by laser cladding. *Transactions of Metal Heat Treatment*, 19(4):1-7.

Xu, Jiang & Liu, Wenjin. (2006). Wear characteristic of in situ synthetic TiB_2 particulate-reinforced Al matrix composite formed by laser cladding. *Wear*, 260(4-5), 486-492.

Yang, Sen, Liu, Wenjin & Zhong, Minlin. (2006). In-situ TiC reinforced composite coating produced by powder feeding laser cladding. *Materials Science and Technology*, 22(4), 519-525.

Yang, Sen, Zhong, Minlin & Liu, Wenjin. (2002). Research on in-situ formation of TiC particles reinforced nickel base alloy coating produced by laser cladding. *Journal of Aeronautical Materials*, 22(1), 26-30.

Zhang, Xiaoping & Hu, Jianhua. (2000). The Application of A New Surface Alloying Technique to Piercing Plug. *Journal of TaiYuan Heavy Machinery Institute*, 21(3), 187-190.

Table 1. Surface roughness parameters of worn surface

Material	*Ra*	R_Y	R_Z	*S*	S_m
H13 steel	4.293	22.939	22.922	0.0051	0.0556
Laser clad layer	0.655	4.917	4.877	0.0025	0.0217

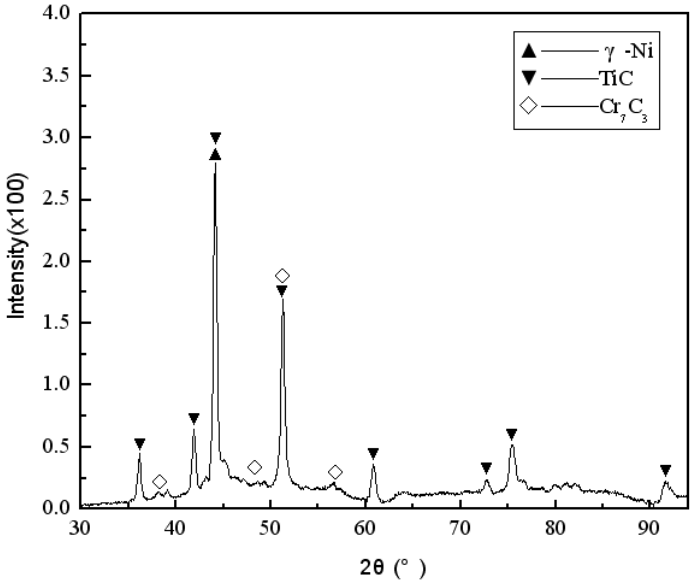

Figure 1. X-ray diffraction spectrum of laser clad layer

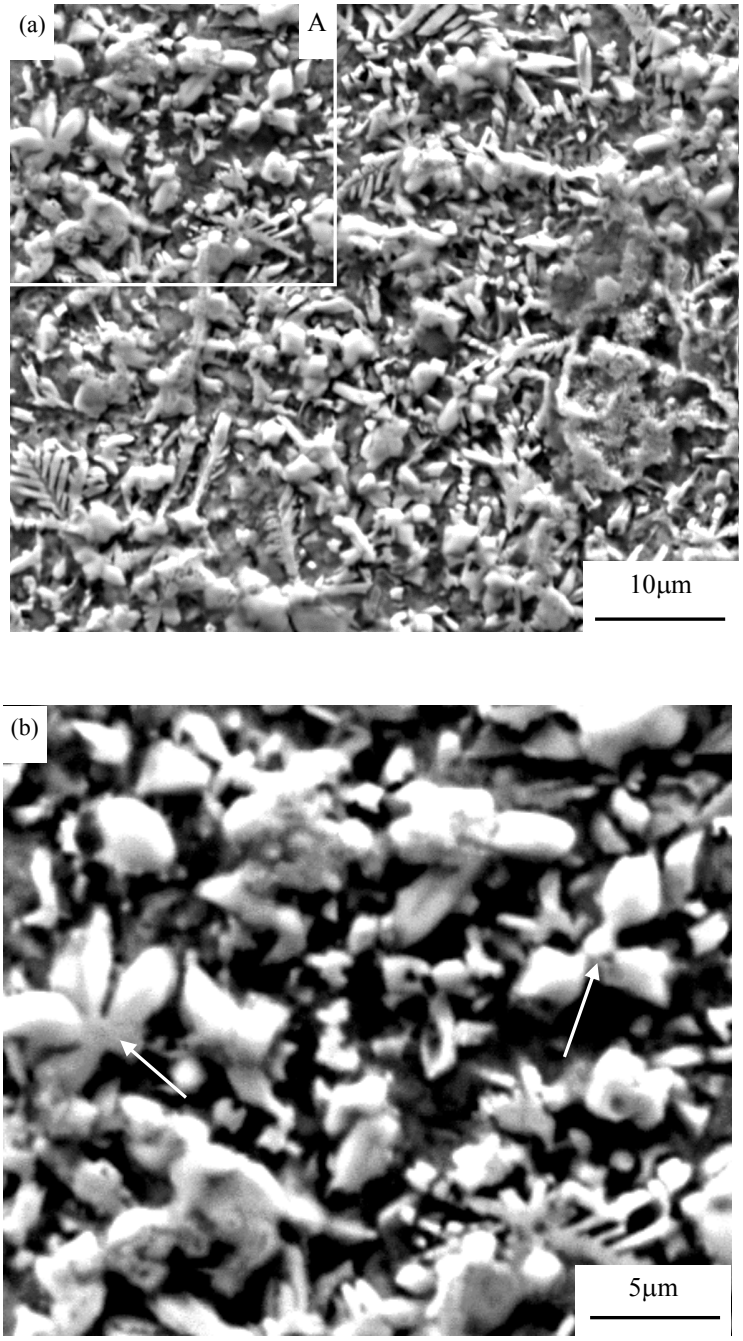

Figure 2. SEM photographs showing microstructure of clad layer
(a) under low magnification; (b)A zone under high magnification

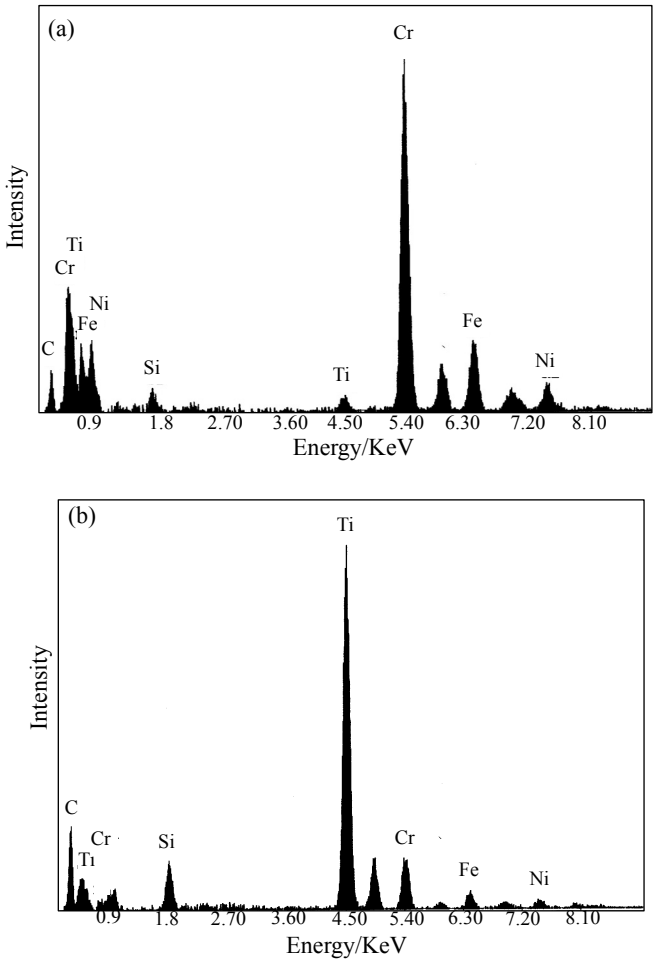

Figure 3. (a)Dendrite and (b)lumpish particles EDX spectrum

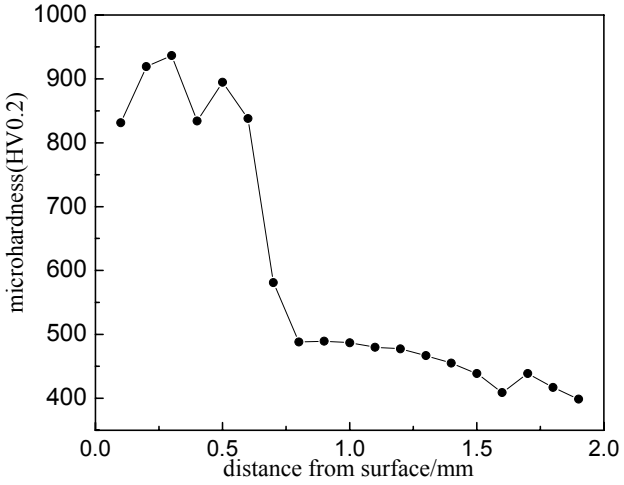

Figure 4. Microhardness distribution curve across the depth of the laser clad layer

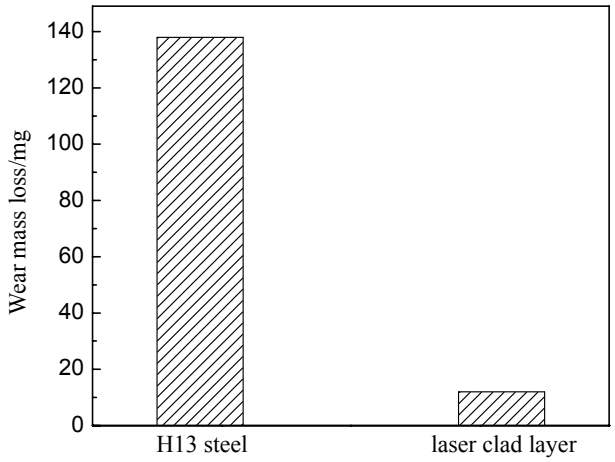

Figure 5. The wear weight loss of clad layer and H13 steel

Modern Applied Science

www.ccsenet.org/journal.html

Vol. 3, No. 3

March 2009

Performance Analysis of a Robust Positional Control with an Induction Actuator by Using a Simplified Indirect Field Oriented Control Algorithm

Chams-Eddine Feraga

Department of electrical Engineering

Guelma University

PO box 401, Guelma 24000, Algeria

E-mail: chferaga @yahoo.fr

Ali Yousfi

Department of electromechanical Engineering

Annaba University

PO box 12, Annaba 23000, Algeria

E-mail: yousfiali51@yahoo.fr

Abdallah Bouldjedri

Department of electrical Engineering

Annaba University

PO box 12, Annaba 23000, Algeria

E-mail: b_abj67@yahoo.fr

Abstract

The aim of this paper is to study the performance of a simplified indirect field oriented control algorithm suited for small power induction actuators. The main particularities of the control strategy under study are the use of a disturbance observer in the speed and position control loops, and the absence of any current measurement. The good performance of the proposed control strategy, particularly as concerns the flux control sensitivity to parameter uncertainties, is shown by theoretical results and digital simulations.

Keywords: Field oriented control, Induction actuator, Performance analysis, Disturbance observer

1. Introduction

High performance motion control with induction actuators requires to control separately the flux and the current producing the torque. As the flux measurement in an induction actuator has numerous drawbacks, the flux in the actuator is usually indirectly controlled by controlling an intermediate variable, which is, in a d-q generalized reference frame, the stator d axis current provided that the reference frame position is selected in such a way that the rotor flux is along the d axis (Bose, 2002; Bin, 2006). However current i_{sd} related to the flux by a function which depends on the electrical parameters. Moreover the computing of the reference frame position depends also on the electrical parameters. Therefore the flux control is sensitive to errors on the parameters (Peresada and al; 2003; Robyns and al; 1993).

In some field oriented control schemes commonly used the d and q axes currents are controlled by PI regulators (Singh and al; 2005). For small power motors, current regulators may be avoided and only estimated values of the currents may be used in the control algorithm (Gorez and al; 1991; Larabi and al; 1998).

In this paper we study the performance of a simplified indirect field oriented control algorithm suited for small power induction actuators improved by the introduction of a disturbance observer in the speed and position control loops.

A main characteristic of the control algorithm under study is that it does not involve any current measurement. The effect of using estimated value of the currents instead of measured ones is therefore investigated. Particularly, the interest of this solution as concerns the sensitivity of the flux control to parameter uncertainties is made clearly

apparent.

The good performance of the proposed control algorithm is emphasized by a theoretical analysis, digital simulations; on 0.25Kw induction actuator.

2. Actuator modeling

In a generalized two axes reference frame, the electrical equations of a two pole induction machine are:

$$\frac{d\psi_{sd}}{dt} = \omega\psi_{sq} - R_s i_{sd} + U_d$$

$$\frac{d\psi_{sq}}{dt} = -\omega\psi_{sd} - R_s i_{sq} + U_q \quad (1)$$

$$\frac{d\psi_{rd}}{dt} = \omega_{sr}\psi_{rq} - R_r i_{rd}$$

$$\frac{d\psi_{rq}}{dt} = -\omega_{sr}\psi_{rd} - R_r i_{rq}$$

The electromagnetic torque is given by:

$$T_{em} = \frac{M}{L_r}\left(i_{sq}\psi_{rd} - i_{sd}\psi_{rq}\right) \quad (2)$$

The fluxes are related to the currents by the following equations:

$$\psi_{sd} = L_s i_{sd} + M i_{rd} \qquad \psi_{rd} = L_r i_{rd} + M i_{sd} \quad (3)$$
$$\psi_{sq} = L_s i_{sq} + M i_{rq} \qquad \psi_{rq} = L_r i_{rq} + M i_{sq}$$

In these equations, ψ_{sd} ψ_{sq} ψ_{rd} ψ_{rq} are the fluxes along the stator and rotor d and q axes; M is the mutual inductance between the stator and the rotor d, q windings; L_s and L_r are the inductances of the stator and the rotor d, q equivalent windings. $L_s=M+l_{s0}$ and $L_r=M+l_{r0}$ where l_{s0} and l_{r0} are the leakage inductances of the stator and the rotor windings. R_s and R_r are the resistances of the stator and the rotor d, q windings; ω is the angular speed of the d, q reference frame with respect to the actuator stator and θ its position; ω_{sr} is the sleep frequency: $\omega_{sr}= \omega- \omega_m$,where ω_m is the rotor angular speed.

The position of the reference frame may be selected in order to obtain $\psi_{rq}=0$ (Leonhard, 2001; Blaschke, 1972; Vas, 1990). From equation (1), (2) and (3) with $\psi_{rq}=0$, we obtain the induction motor block diagram shown in full line in Figure1. In this diagram T_R is the load torque (considered as a perturbating torque), J is the inertia of the actuator rotor and of the mechanical load, K is the viscous torque coefficient, σ is the dispersion coefficient [$\sigma=1-M^2/(L_sL_r)$].

$\tau_s= L_s/ R_s$ and $\tau_r= L_r/ R_r$ are the stator and rotor electrical time constant and s is the Laplace operator.

3. Control strategy

It is assumed that the flux can be controlled in open loop and kept constant and equal to its reference value $(\psi_{rd})_{ref}$ after a transient associated to its build up, by considering for the d axis control voltage

$$U_d = \frac{R_s}{M}(\psi_{rd})_{ref} - \omega\sigma L_s i_{sq} \quad (4)$$

With $$\omega = \omega_m + \frac{M R_r}{L_r}\frac{i_{sq}}{(\psi_{rd})_{ref}} \quad (5)$$

In equation (4) the term $-\omega\sigma L_s i_{sq}$ corresponds to a state feedback (shown in broken line in Figure1) which ensures the decoupling of the d axis from the q axis.

As no current measurement is performed the value of current i_{sq} which is involved in this computation must be estimated. This estimation is performed by considering the SISO system to which the block diagram of the actuator reduces when the rotor flux ψ_{rd} is constant (this block diagram is shown in Figure 2 inside the frame in dotted line) and by neglecting the electrical time constant $\sigma L_s/(R_s+(L_s/L_r)R_r)$ in this block diagram:

$$i_{sq} = \frac{U_q - \frac{L_s}{M}(\psi_{rd})_{ref}\,\omega_m}{R_s + \frac{L_s}{L_r}R_r} \quad (6)$$

The actuator rotor position is controlled through the q axis voltage U_q by using a regulator comprising a subordinate speed loop with a disturbance observer. As the block diagram of the actuator reduces to the linear SISO system shown in Figure2 (inside the frame in dotted line), when the rotor flux is constant, the synthesis of this controller is straightforward (Gorez and al; 1991). The model H of the disturbance observer is deduced from the SISO equivalent system after compensating the emf $(\psi_{rd})_{ref}\ \omega_m L_s / M$ and by neglecting the viscous torque coefficient and the electrical time constant:

$$H = \frac{M\,(\psi_{rd})_{ref}}{(R_s L_r + R_r L_s) J s} \tag{7}$$

As an integral action exists in the disturbance observer, the position and speed controllers may be simply proportional regulators. More details about the disturbance observer used are given in (Robyns and al; 1992).

4. Flux control sensitivity to parameter uncertainties

As the flux is controlled in open loop in the proposed control scheme, errors in the electrical parameters imply errors on the flux. These errors can be computed in steady state.

From (1) and (3), one gets the following steady state equations:

$$U_d = R_s i_{sd} - \omega\sigma L_s i_{sq} - \omega\frac{M}{L_r}\psi_{rq} \tag{8a}$$

$$U_q = \omega\sigma L_s i_{sd} + R_s i_{sq} + \omega\frac{M}{L_r}\psi_{rd} \tag{8b}$$

$$i_{sd} = \frac{1}{M}\psi_{rd} - \omega_{sr}\frac{L_r}{MR_r}\psi_{rq} \tag{8c}$$

$$i_{sq} = \omega_{sr}\frac{L_r}{MR_r}\psi_{rd} + \frac{1}{M}\psi_{rq} \tag{8d}$$

By introducing (8c) and (8d) in (8a) and (8b), one gets the following relations between U_d and U_q and ψ_{rd} and ψ_{rq}:

$$U_d = A\,\psi_{rd} - B\,\psi_{rq} \tag{9a}$$

$$U_q = B\,\psi_{rd} + A\,\psi_{rq} \tag{9b}$$

With $A = \frac{1}{M}(R_s - \omega\,\omega_{sr}\frac{\sigma L_s L_r}{R_r})$

$$B = \frac{1}{M}(\omega_{sr}\frac{L_r R_s}{R_r} + \omega L_s)$$

According to the control strategy adopted, voltage U_d and U_q can be related to the reference value of the rotor flux, $(\psi_{rd})_{ref}$ by

$$U_d = A^*\psi_{ref} \tag{10a}$$

$$U_q = B^*\psi_{ref} \tag{10b}$$

The * indicating that estimated values of the parameters have been used in the computation of A and B.

From (10a) and (10b), one gets the following expressions for the errors due to parameter uncertainties on the flux along the d axis (which should be equal to reference flux ψ_{ref}), and on the flux along the q axis ψ_{rq} (which should be equal to zero):

$$\frac{\psi_{rd}}{\psi_{ref}} = \frac{A\,A^* + B\,B^*}{A^2 + B^2} \tag{11a}$$

$$\frac{\psi_{rq}}{\psi_{ref}} = \frac{A\,B^* - A^*B}{A^2 + B^2} \tag{11b}$$

From (11a) and (11b), it is possible to obtain the error on the flux amplitude ψ_r and on the flux orientation ρ:

$$\frac{\psi_r}{\psi_{ref}} = \frac{\sqrt{(\psi_{rd}^2 + \psi_{rq}^2)}}{\psi_{ref}} = \sqrt{\frac{A^{*2} + B^{*2}}{A^2 + B^2}} \tag{12a}$$

$$\rho = arctg\frac{\psi_{rq}}{\psi_{rd}} = arctg\left(\frac{A\,B^* - A^*B}{A^2 + B^2}\right) \tag{12b}$$

By introducing (8c), (8d), (11a) and (11b) in (2), one gets the following expression for the electromagnetic torque:

$$T_{em} = \frac{\omega_{sr}}{R_r}\frac{\left(A^{*2} + B^{*2}\right)}{\left(A^2 + B^2\right)}\psi_{ref}^2 \tag{13}$$

5. Simulated Results and Discussions

The parameters of the used machine model are given in Table 1. Figure 3 shows the speed, torque, fluxes, voltages and currents responses of the system to a step in the speed reference from *0* to *1500RPM* and to a step of torque equal to the rated torque at *t=1s* until *t=1.5s*. The very low sensitivity of the system to the step of torque, due to the disturbance observer, is clearly apparent.

In figure 4 an error of *50%* on the rotor and stator resistances is introduced. This induces an error on the flux when the actuator is loaded at *t=1.5*s, but owing to the robustness of the controller, this error remains small.

Figure 5 shows the position response of the system to a step in the position reference from *0* to *100Rad*. In spite of the fact that the sensitivity of the flux control to parameter uncertainties is more important at low speed; the position response is very satisfactory.

6. Conclusion

It has been shown in this paper that it is possible to design a simplified indirect field oriented control system which has, in spite of the simplifications, good performance owing to the design of a speed or position controller based on techniques of robust control evolved for linear systems, and on an appropriate choice of the decoupling method which allows to obtain a very reduced flux control sensitivity to parameter uncertainties.

References

Bin, w. (2006). *High power converters and ac drives*. New Jersey: John Wiley & Sons.

Blaschke, F. (1972). The principle of field orientation as applied to the new transvektor closed-loop control system for rotating field machines. *Siemens Review*, 34, 217-220.

Bose, B. K. (2002). *Modern Power Electronics and AC Drives,* New Jersey: Prentice-Hall.

Gorez, R., Galardini, D., & Zhu, K.Y. (1991). Internal model control and disturbance observer. *Proc. of the 30th IEEE-CDC, Brighton*, 229-235.

Larabi, A., Grenier, D., & Labrique, F.A. (1998). Simplified vector control scheme for an induction motor revisited, *5th International Workshop on Advanced Motion Control.* APOS'98, *Coimbra, 29 Jun- 1Jul,* 24 – 29.

Leonhard, W. (2001). *Control of Electrical Drives.* (3rd ed.). Berlin: Spinger Verlag.

Peresada, S., Tilli, A., & Tonielli, A. (2003). Theoretical and Experimental Comparison of Indirect Field-Oriented Controllers for Induction Motors. *IEEE, Trans. on Power Electronics*, 18, 151-163.

Robyns, B., Galardini, D., Gorez, R., Labrique, F., & Buyse, H. (1992). Asservissements de vitesse d'un actionneur asynchrone par modèle de l'actionneur et de sa commande vectorielle. *Actes des Journées d'Etudes de la SEE sur les Asservissements Electromécaniques Rapides-Modélisation et Régulations Avancées, Metz, 21-22 octobre*, 45-51.

Robyns, B., Buyse, H. (1993). Comparison of the sensitivity of the flux control to parameter uncertainties in two induction actuator indirect field oriented control schemes. *Proc. Of EPE'93, Brighton, 13-16 september*, 402-407.

Singh, G.K., Singh, D.K.P., Nam, K., & Lim, S.K. (2005). A simple indirect field-oriented control scheme for multiconverter-fed induction motor**.** *IEEE, Trans. on Industrial Electronics*, 52, 1653-1659.

Vas, P. (1990). *Vector Control of AC Machines.* Oxford: Clarendon Press.

Table1. Induction machine data

Components	Rating values
Voltage	*V =110V*
Power	*P =0.25Kw*
Speed	N_m *=1500r/min*
Moment of inertia	$J = 0.012kg.m^2$
Coefficient of viscous friction	*K = 0.0011Nms*
Stator resistance	R_s *=1.923 Ω*
Rotor resistance	R_r *=1.739 Ω*
Stator inductance	L_s*=0.1157 H*
Rotor inductance	L_r*=0.1154 H*
Mutual inductance	*M=0.1126 H*

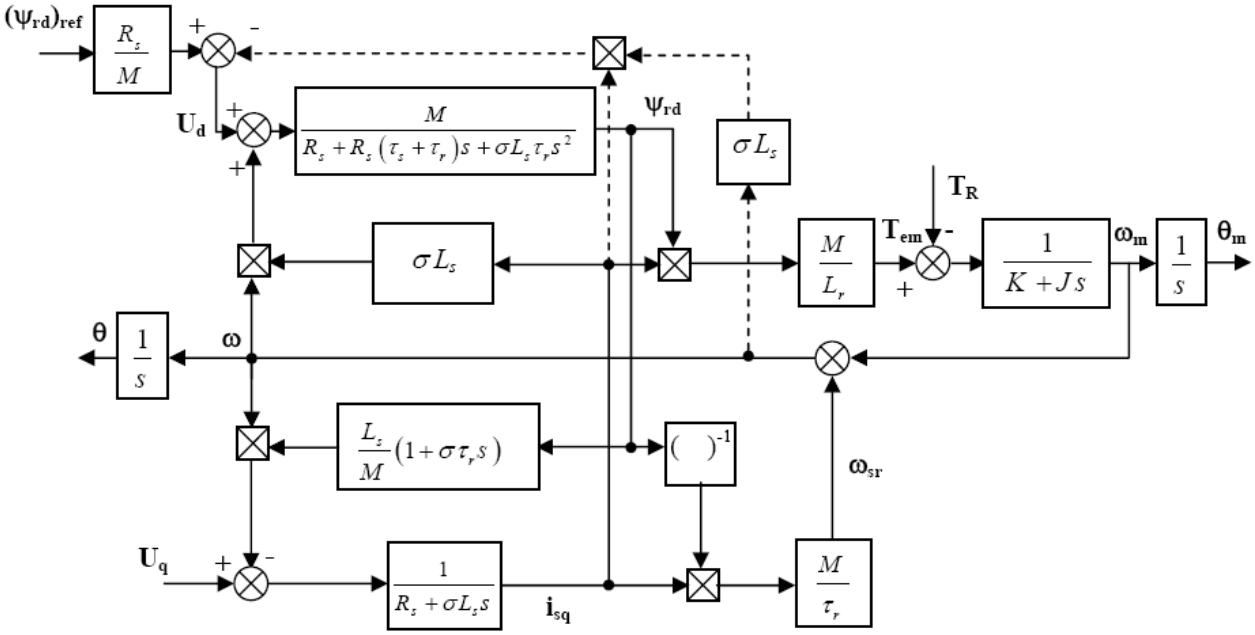

Figure 1. Induction actuator block diagram

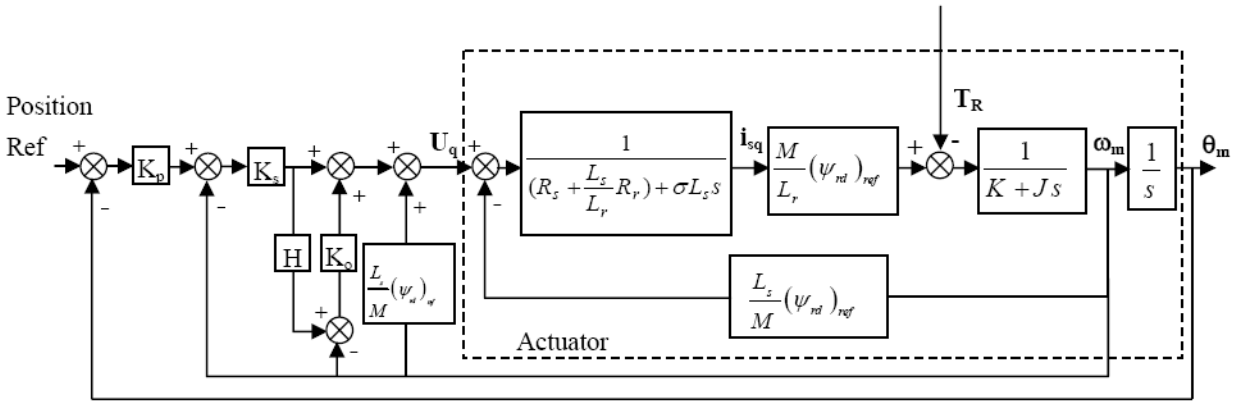

Figure 2. Block diagram of the position control

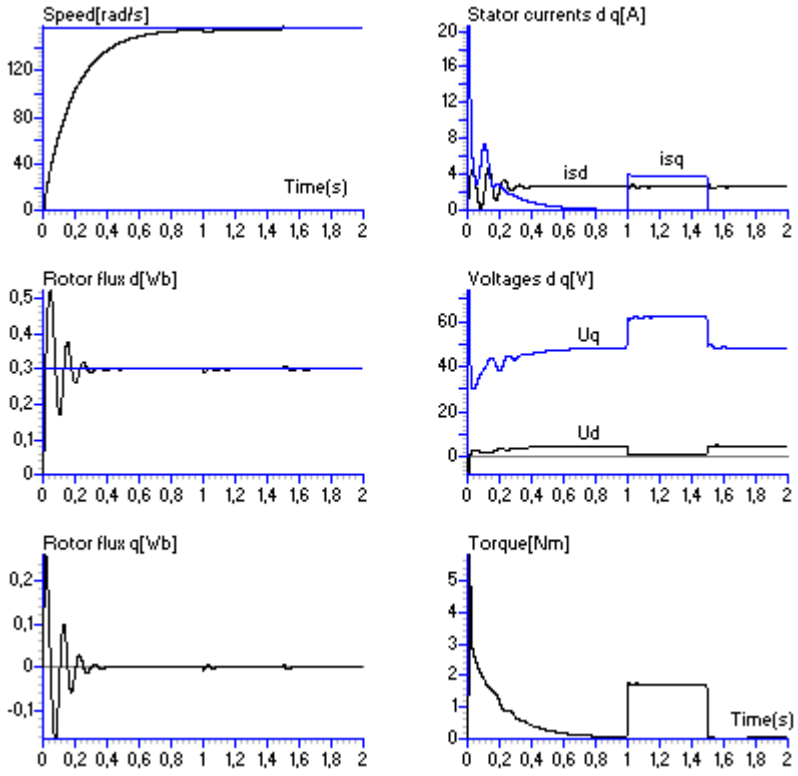

Figure 3. Simulation of the dynamic behavior of the system to a step in the speed reference and to a step in the load torque

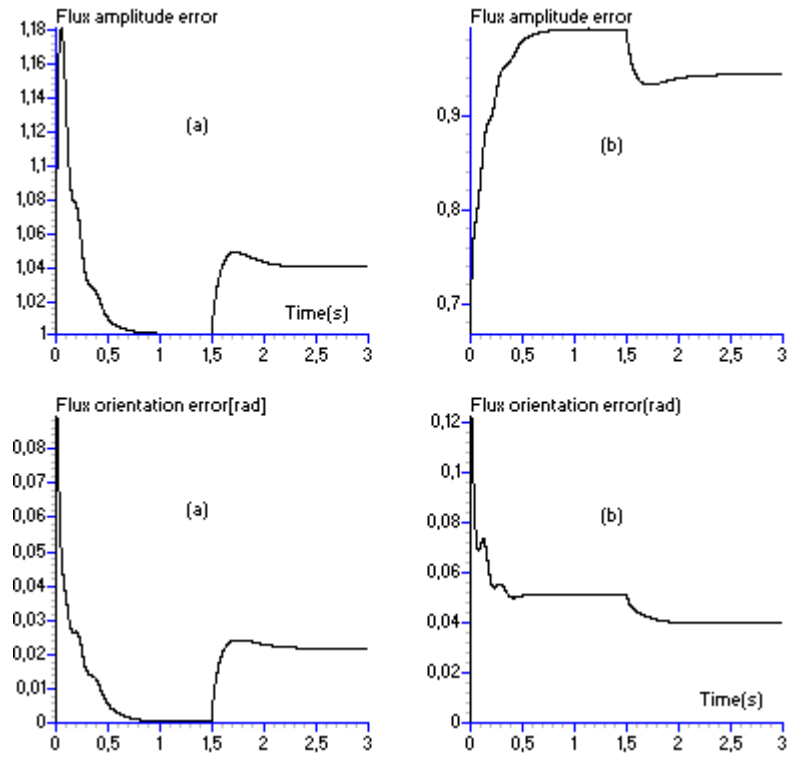

Figure 4. Flux error in steady state due to parameter uncertainties

a- Flux error when $R_r=1.5R_r^*$

b- Flux error when $R_s=1.5R_s^*$

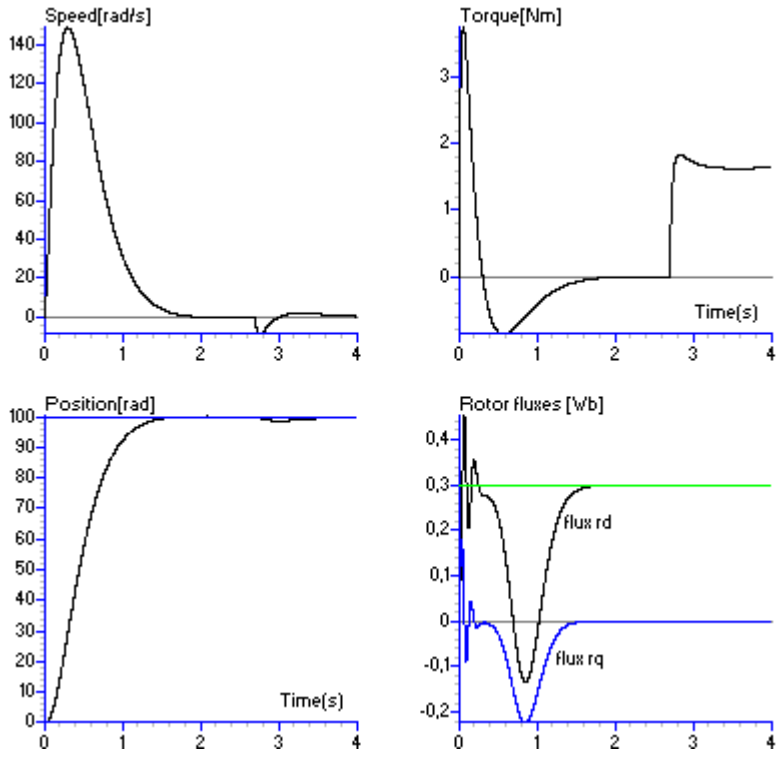

Figure 5. Simulation of the dynamic behavior of the system
to a step in the position reference

Modern Applied Science

www.ccsenet.org/journal.html

Vol. 3, No. 3

March 2009

Alkaline Extraction Method of Cottonseed Protein Isolate

Buning Zhang

School of Materials Science and Engineering

Northwestern Polytechnical University

127 Youyi Xilu, Xi'an 710072, China

E-mail:eins001@163.com

Yingde Cui (Corresponding Author)

Institute of Green Chemical Engineering

Zhongkai University of Agriculture and Engineering

24 Dongsha street, Haizhu District, Guangzhou 510225, China

E-mail: cuigdut@yahoo.com.cn

Guoqiang Yin, Xinming Li & Xiaoxia Zhou

Institute of Green Chemical Engineering

Zhongkai University of Agriculture and Engineering

24 Dongsha street, Haizhu District, Guangzhou 510225, China

This work was supported by the National Natural Science Fund of China (Grant No. 20776164).

Abstract

Cottonseed protein was extracted from defatted cottonseed flour with alkaline solvent and its precipitation property in different pH value was investigated. Orthogonal experiments design was introduced and factors influencing protein extraction were studied, namely, extraction solvent type, solvent-to-flour ratio, extraction pH value, extraction temperature and time. The optimum scheme of extraction was obtained: 0.1N KOH as extraction solvent, solvent-to-flour ratio=12,pH=12.5, temperature=60℃ and time=40min.Under this condition, the cotton protein extractability is above 70%and the protein extraction can be directly applied to further chemical modification.

Keywords: Cottonseed flour, Cottonseed protein, Extraction, Precipitation

1. Introduction

Recently, protein used as a non-petroleum, safe and biodegradable and renewable resource was focused by many researchers. Applications on modification of protein, especially in nonfood industry have been increased. Carboxyl, amido, amide, hydroxy, sulfhydryl groups exist in the main chain of protein molecule. Chemical modification such as grafting, copolymerization and crosslinking could result in the desirable materials of proteins. As a herbage, cotton cultivation is traditionally for the production of fibers. Nevertheless cottonseed is also an important source of oil and protein with the content of 38%-45% protein in defatted flour (Li, 2004, PP. 34-35). Cottonseed oil is used in cooking, salads, shortenings and the flour for livestock feed. In China about 8.0 million tons of cottonseed are produced annually, which ranked the first in the world and accounted for one third production of the world(Xue, 2007, PP. 55-58). Herein, annual defatted cottonseed flour would exceed 4.0 million tons after oil extraction, which contained nearly 1.6 million tons of protein (Dai, 2001, PP. 30-32, Yang, 2000, PP. 3-4). Cottonseed flour have reasonable amino acid components and nutrition value, however, the presence of toxic gossypol in the cottonseed flour is a limiting factor for human consumption and various methods have been proposed for reduction of free gossypol content. Due to the denaturation of proteins in the thermal processing of cottonseed oil extraction, and subsequently reduction of nutrition value, this source of protein has not been intensively and extensively applied (Li, 2005, PP. 22-23). Thus, 80% defatted cottonseed have to be used as fertilizer or substrates for edible mushroom, while only 5-10% are used as feed materials, which result in a great waste of protein (Lu, 2003, PP. 48-51). Therefore, the application of protein isolated from defatted cottonseed flour in non-feed or non-food industries would have great significance in economy and society.

Isolating proteins from cottonseed was usually performed by the method of "alkali extraction and acid precipitation", which utilized the difference of protein solubility in acids and alkali, dissolved the protein in alkali solutions in specific pH and then adjusted the solution pH with acids until the isoelectric point was attained and then separated out the protein isolates. The key point of this processing was to extract protein from the cottonseed flour as much as possible. In this paper, the effect of technical conditions were investigated, and the resulting protein extraction would be taken further investigation for modification, such as grafting copolymerization with other monomers, in order to prepare different functional cottonseed protein derivates or composite materials.

2. Materials and methods

2.1 Materials

Defatted cottonseed flour was provided by China cotton-unis bioscience Co., Ltd., used for the protein extractions after screened through 80 mesh(total protein content 49.17 % by Kjeldahl Method using the conversion factor of 6.25). All other reagents were of analytical grade and used without further purification.

2.2 Extraction of cottonseed protein

Cottonseed flour (constant weight) was extracted with the extracting solutions at a solvent-to-flour ratio of 10-15 (w/v) with constant stirring after the desirable temperature and pH value were adjusted. The pH value was kept constant by extracting solutions. After extraction, solutions were filtrated immediately. The protein content was calculated after nitrogen analysis by Kjeldahl Method and UV spectrophotometry method (Guo, 1996, PP. 61-64), using the conversion factor of 6.25.The protein extraction rate was calculated according to the following formulation:

Extraction rate%=Total protein after extraction/ Total original cottonseed protein×100%

2.3 Precipitation of cottonseed protein

The cottonseed flour was extracted with 0.1 N KOH at pH 10.5 and 40℃ for 40 minutes and the content of total protein was calculated after extraction. Then at the different pH values adjusted with 0.5 N HCl or 0.5 N NaOH, the extracting solution were stirred and then kept steady at 5℃ for 24hours until precipitation, respectively. The protein content and volume of the suspension was calculated. The precipitation rate was calculated according to the following formulation:

Precipitation rate %=(Total protein after extraction-Total protein of suspension) /Total protein after extraction×100%

3. Results and discussion

3.1 Effect of medium

Generally, mediums used for extracting cottonseed protein are ammonia(Zhao, 2002, PP. 25-26), NaOH(Cui, 2003, PP. 43-45), KOH(Zhao, 2007, PP. 49-50), $Na_2S_2O_3$ (Liadakis, 1993, PP. 918-922), NaCl(El Tinay, 1988, PP. 19-27), $CaCl_2$(El Tinay, 1988,PP.19-27, 57-63), sodium hexametaphosphate (Shemer, 1973, PP. 460-462) and so on. According to the previous researches, to obtain the optimized experimental parameters, a four-factor at three-level orthogonal array experimental design $L9(3)^4$ was adopted to extract protein from cottonseed flour at a solvent-to-flour ratio of 10 (w/v). The four factors were medium, temperature, pH value and time. Based on the experimental results of the previous orthogonal design, the optimal ranges for each factor and their extraction effect could be obtained, and the optimal conditions could be speculated. The factors studied and the assignments of the corresponding levels are listed in Table 1.

The analytical results of 9 tests are listed in Table 2. The values of $|k_{max}-k_{min}|$ in Table 2 indicated that the effect of medium, temperature, pH value and time. The efficiency of these four factors were classified in the order of medium>temperature>pH value>time. Thus, medium was the major factor affecting extraction rates and 0.1 NKOH was applied for further investigation.

3.2 Precipitation characteristics of cottonseed protein

Generally, isoelectric point (*pI*) of plant oil proteins range from pH 4 to 5. Among them, *pI* of protein from soybean, peanut and rapeseed is about 4.5 while from sunflower seed 4.0. As shown from Figure 1, the highest precipitation for cottonseed protein was observed between pH 4 to 5.5. Due to different techniques of oil extraction and de-gossypol process, highest precipitation for cottonseed protein from various source usually ranged from pH 3.5 to 5.5 (King, 1977, PP. 1211-1213). Liadakis (Liadakis ,1993, PP. 918-922) found that the solubility of cottonseed protein was least at pH4.37 while Beradi found that at pH 5.0. In the present paper, the precipitation rate was highest at pH5.0, which was comparable with previous literatures and could be used for further acidic precipitation process.

3.3 Effect of solvent-to-flour ratio

Cottonseed flour (constant weight) was extracted with 0.1N KOH solution at a different solvent-to-flour ratio with constant stirring at pH 12 and 60℃ for 40 minutes and the filtrated flour was extracted again with a solvent-to-flour ratio10 (w/v) in the same condition. The results are shown in Figure 2.

When solvent-to-flour ratio was too low, cottonseed flour swelled due to water adsorption, extracting solution concentration became dense, causing the viscosity of the solution increased which hampered molecular diffusion. The velocity of the extraction decreased accordingly. Although the extracting concentrate was dense, the obtained protein amount was low. When solvent-to-flour ratio was 6, extraction was the lowest. Extraction rate increased with the increasing of solvent-to-flour ratio. When the solvent-to-flour ratio ranged from 12 to 14, extraction rates made no significant difference, due to the adverse effect of high solvent-to-flour ratio which could cause low protein content of the extraction and interfered with further chemical modification. Considering the first extraction rate and the total extraction rate after two times operation, the solvent-to-flour ratio of 12 (w/v) was acceptable and desirable.

3.4 Effect of pH value

Cottonseed flour (constant weight) was extracted with 0.1N KOH solution at a constant solvent-to-flour ratio of 12 (w/v) with constant stirring at different pH and 60℃ for 30 minutes. The results are shown in Figure 3.

Obviously, in alkaline condition, extraction rate increased with the increasing of pH value. Separation and purification of proteins for foodstuffs were generally performed under pH 10(Di, 2006, PP. 439-441, Feng, 2004, PP. 29-30, Luan, 2000, PP. 58-60). Since the further step of modification was undertaken in alkaline condition and in order to attain more protein, the pH value applied could be increased properly. But cottonseed protein was prone to degradation and denaturation and difficult to be kept in strong alkaline condition, so pH value of 12.5 was selected for further investigation.

3.5 Effect of temperature

Cottonseed flour (constant weight) was extracted at same solvent-to-flour ratio of 12 (w/v) with stirring at pH 12.5 and different temperature for 30 minutes. The results are shown in Figure 4.

With the increasing of temperature, extraction rate of protein increased. Extraction rate varied almost linearly with temperature. When temperature increased, molecules moved fast, mass transfer rate of interface between solid and liquid developed. Therefore, increasing temperature could promote mass transfer and solubility, reduce viscosity of solution and thus increase extraction rate. However, high temperature could cause the reduction of protein activity and thermal denaturation of protein. Additionally, with the increasing of temperature, color of the protein extraction became dark, so temperature of 60℃ was selected for further investigation.

3.6 Effect of time

Cottonseed flour (constant weight) was extracted at same solvent-to-flour ratio of 12 (w/v) with constant stirring at pH 12.5, temperature 60℃ for different time. The results are shown in Figure 5.

As seen from Figure 5, with the increasing of time, extraction rate increased. After 20 minutes, extraction rate amounted to 50%. While after 40 minutes the extraction curve slope decreased obviously and extraction rate increased slowly. Until 80 minutes, extraction rate increased by only 4%, so time of 40 minutes for protein extraction was suitable.

4. Conclusions

At a solvent-to-flour ratio of 10 (w/v), the protein extraction efficiency of these four factors were classified in the order of medium>temperature>pH value>time. The optimized extracting parameters of medium, solvent-to-flour ratio, temperature, pH value and time were 0.1NKOH, 12, 60℃,12.5 and 40 minutes, respectively. Under this optimum condition, the protein extraction rate was above 70% and the obtained protein extraction could be used for chemical modification directly without further process.

References

Cui, Z.Q., Qian, Y.Y., & Shi, M.Y. (2003). Protein extraction from cottonseed meal produced by two-phase solvent extraction. *China oils and fats*, 28(11):43-45.

Dai, S.J., Zhao, G.R. (2001). Development and application of cottonseed protein isolates. *Shihezi science and technology*, (1):30-32.

Di, A.H., Ji, N., & Liu, H.Z. (2006). Study on the Extraction of Separate Protein of Oats. *Food science*, 27(12):439-441.

El Tinay, A.H., Nour, A.M., & Abdel-Karim, S.H., et al. (1988). Aqueous protein and gossypol extraction from glanded cottonseed flour: Factors affecting protein coagulation and gossypol content. *Food Chemistry,* 30(1):19-27.

El Tinay, A.H., Nour, A.M., & Abdel-Karim, S.H., et al. (1988). Aqueous protein and gossypol extraction from glanded cottonseed flour: Factors affecting protein extraction. *Food Chemistry,* 29(1):57-63.

Feng, Z.L., Yang, Z.J., & Yuan, B.L., et al. (2004). Study of extracting technology of isolating soybean protein. *China oils and fats*, 29(11):29-30.

Guo, Q.H., Li, S.L.(1996). Quick protein determination of cottonseed extracting solution by UV spectrophotometry method. *Journal of Tianjin university of light industry*, (1):61-64.

King, E.E., Lamkin, G.E. (1977). Isolation of proteins from glanded cottonseed. *Journal of Agricultural and Food Chemistry,* 25(5):1211-1213.

Li, Y.L., Li, S.B., & Wang, S.P. (2005). Development and utilization of cottonseed protein. *China cotton processing*, (3):22-23.

Li, Z.Q., Gu, D., & Dan, N. (2004). Nutrition characteritics and application of dephenolized cottonseed protein. *China diary*, (8):34-35.

Liadakis, G.N., Floridis, A., &Tzia, C., et al. (1993) Protein isolates with reduced gossypol content from screw-pressed cottonseed meal. *Journal of Agricultural and Food Chemistry,* 41(6):918-922.

Lu, H. (2003). Nutrition value and edible trends of cottonseed protein. *Modern business trade industry*, (11):48-51.

Luan, G.Z., Zhang, W. (2000). Preparation of a protein isolate (Wgpi) from wheat embryo. *Journal of qiqihar university(Natural science edition)*,16(2):58-60.

Shemer, M., Mizrahi, S., & Berk, Z., et al. (1973). Effect of processing conditions on isolation of cottonseed protein by sodium hexametaphosphate extraction method. *Journal of Agricultural and Food Chemistry,* 21(3):460-462.

Xue, M., Wu, X.F., & Guo, L.Y., et al. (2007). Application of dephenolized cottonseed protein in aquatic feed. *China journal of animal science*, 43(8):55-58.

Yang, W.H., Xiang, S.K. (2000). Retrospect and prospect of comprehensive utilization of cottonseed protein. *China cotton*, 27(3):3-4.

Zhao, L.C. (2007). Experimental study on processing technique of isolated cottonseed protein. *Cereals and oils processing*, (3):49-50.

Zhao, Y., Fan, Q.F. (2002). Study on the extraction of protein from cotton seed. *Science and technology of cereals,oils and foods*, 10(1):25-26.

Table 1. Assignments of the levels to factors in orthogonal design

Factors	Level 1	Level 2	Level 3
Medium	1%Ammonia	0.1NNaOH	0.1NKOH
pH	12	11.7	11.5
Temperature(℃)	20	40	60
Time(min)	20	40	60

Table 2. The matrix associated with the analytical results

Factors Number	pH	T/℃	t/min	Medium	Extraction rate(%)
1	12	20	20	Ammonia	14.33
2	12	40	40	NaOH	38.45
3	12	60	60	KOH	65.03
4	11.7	20	40	KOH	25.38
5	11.7	40	60	Ammonia	21.67
6	11.7	60	20	NaOH	51.36
7	11.5	20	60	NaOH	19.97
8	11.5	40	20	KOH	26.01
9	11.5	60	40	Ammonia	10.1
Average1	39.270	19.893	30.567	15.367	
Average2	32.803	28.710	24.643	36.593	
Average3	18.693	42.163	35.557	38.807	
$\lvert k_{max}-k_{min}\rvert$	20.577	22.270	10.914	23.440	

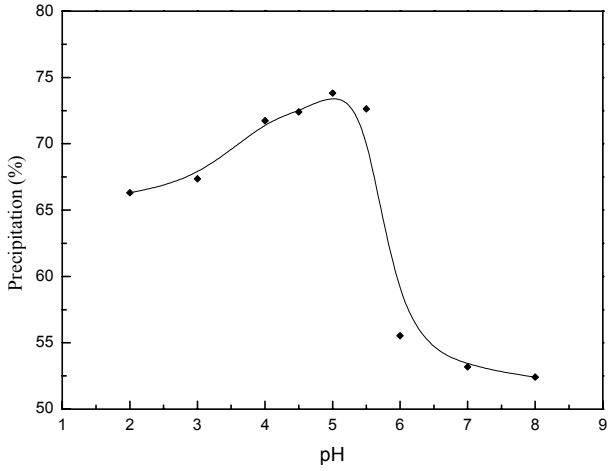

Figure 1. Effect of pH value on precipitation of cottonseed protein

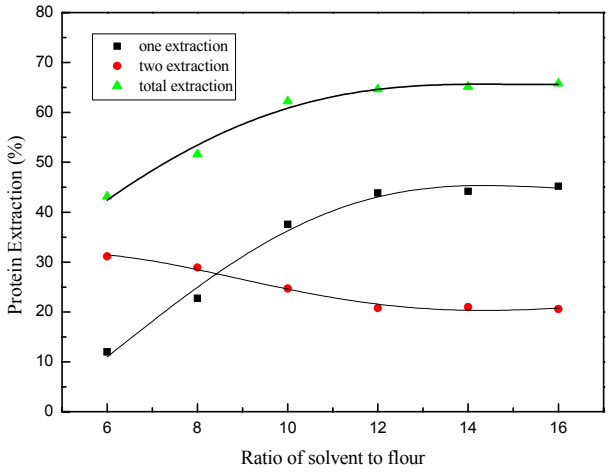

Figure 2. Effect of solvent-to-flour ratio on extraction of cottonseed protein

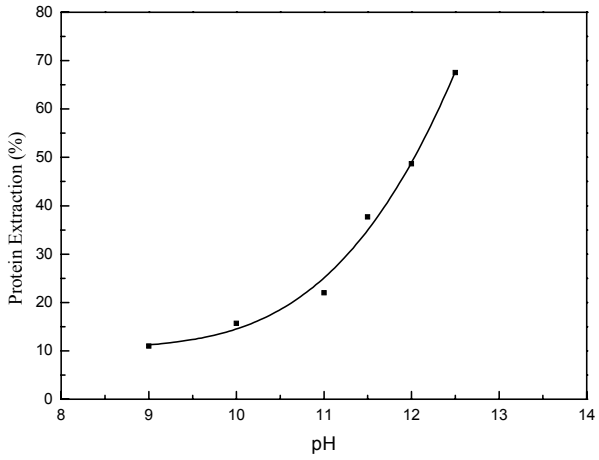

Figure 3. Effect of pH value on extraction of cottonseed protein

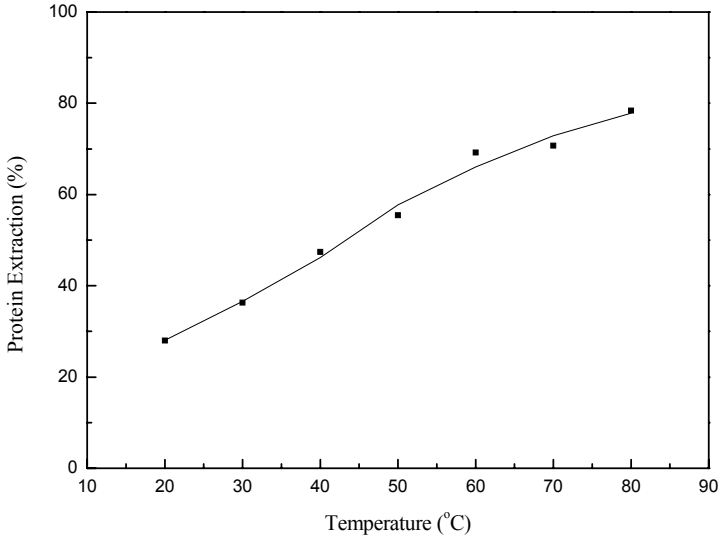

Figure 4. Effect of temperature on extraction of cottonseed protein

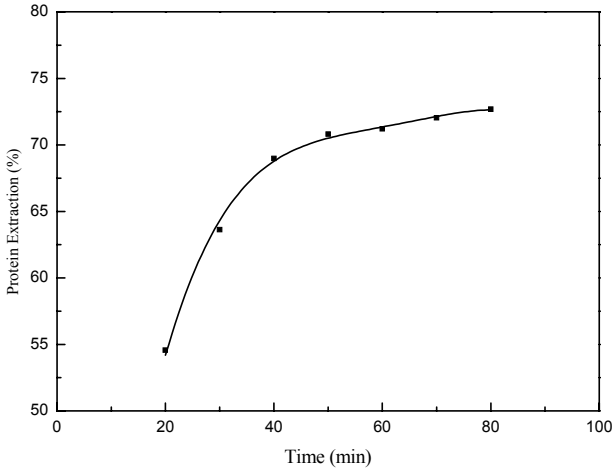

Figure 5. Effect of time on extraction of cottonseed protein